Modeling Rapidly Fading Supernovae as Nickel-Free Core-Collapse Explosions of Extended Helium Stars

Thesis by
Io Kleiser

In Partial Fulfillment of the Requirements for the
degree of
Doctor of Philosophy

CALIFORNIA INSTITUTE OF TECHNOLOGY
Pasadena, California

2019
Defended April 20, 2018

Io Kleiser
ORCID: 0000-0001-5332-1156

ACKNOWLEDGEMENTS

Most critical to the making of this thesis are my advisors and close collaborators. Many thanks go to my official advisor, Sterl Phinney, for keeping me on track throughout most of my graduate career. He has been an irreplaceable resource not just in terms of scientific knowledge but also personal guidance and emotional support. He has helped pull me out of many difficult episodes in graduate school with great understanding and his focus on cultivating my love of physics. None of the work in this thesis would be possible without my closest collaborator, Dan Kasen, who has worked with me, inspired me, and supported me since I was an undergraduate. I am incredibly lucky to have spent most of my career in astronomy collaborating with someone who has both seemingly unstoppable kindness and patience as well as an incredible knack for identifying impactful problems in astrophysics for his students. I could not have asked for a better team of advisors to guide me to this point. Thank you to the rest of my thesis committee: Shri Kulkarni, Evan Kirby, Phil Hopkins, and Chuck Steidel, who have also provided me with valuable guidance throughout my graduate career.

Additionally, I'd like to express great appreciation to Lars Bildsten, who set me back on track to my own thesis topic after trying times in early grad school. Lars was the first professor who sat down with me, took out a notepad, and asked what my interests were–then helped me develop a thesis plan based on the science I was passionate about. Thanks also to Matteo Cantiello for working with me in the early stages of this transition back into supernova research and to Jim Fuller for his help with my later work.

I would also like to acknowledge that I was granted incredible freedom in choosing my topics of research due to the DOE NNSA Stockpile Stewardship Graduate Fellowship Program, which has funded me through almost all of my graduate career. Thank you to Shelly Olsan for making sure I had the financial support I needed, and thanks also to Laura Berzak Hopkins for not only mentoring me scientifically during my summer at LLNL but also acting as a sounding board and grounding influence.

Perhaps one of the best things about being a graduate student in the Caltech Astronomy Department were the other students. I could not have asked for a kinder, more supportive group of people than my incoming class, without whom I might not have made it through my first year. Michael Eastwood, Becky Jensen-Clem,

Scott Barenfeld, Marta Bryan, and Marin Anderson: you are all so brilliant and accomplished, yet you managed to temper the anxiety of classes and quals with camaraderie and coloring books, and for that I cannot express enough gratitude.

I have also had incredible unwavering support from many of my other peers, and feel I have made a group of lifelong friends. Matt Gethers, Abhilash Mishra, Allison Strom, Mike Bottom, Heather Duckworth, Donal O'Sullivan, Nairn Baliber, Dave Yeaton-Massey, Gina Duggan, and Melodie Kao: because of you, I am a better, stronger person, and my friendships with you are some of the most valuable things I take with me out of this phase of my life. To my pre-grad school friends, Maria Dunlavey, Robin Lehleitner, Emily Baker-White, David Hanifi, and Sam Halverson: even over long distances, you have been there for me for years or even decades, and I can't imagine my life without you.

I also owe a deep gratitude to those who have defended and protected me and my fellow students. Samaya Nissanke, Chiara Mingarelli, Katey Alatalo, and countless other scientists in my field (and outside of it) who have stood up to sexual harassment and provided safe-havens for its victims, your bravery and self-sacrifice allowed another generation of women to push through and complete their doctorates. Thank you to Azeen Ghorayshi for her excellent reporting and exposition of sexual harassment in academia, and thanks to the countless people who sent words of encouragement when I needed them the most. Thank you to Jackie Villadsen, Alicia Lanz, and others who fought hard to protect me and my fellow students on campus. Thanks also to Felicia Hunt and Fiona Harrison, who worked tirelessly for so long for a better and safer Caltech campus.

Thank you to family for encouraging my love of science from a young age and seeing me all the way through college. Finally, I want to thank my aunt, Erika Walczak. Without you, I don't know what kind of person I would be. Thank you for your unrelenting kindness, understanding, willingness to listen, and dedication to keeping my head above water. Love you, Tia.

ABSTRACT

Supernovae are the engines of the universe, pulling material out of the furnaces of stars and spewing it out into their galaxies. As some of the most powerful explosions since the Big Bang, they influence not only the chemical but also mechanical evolution of the galaxies they inhabit. They induce star formation and produce the building blocks of planets, organisms, and ultimately, civilizations. Understanding the connections between the supernovae we observe and the stars that would have produced them is a critical piece of understanding this process.

Unfortunately, we rarely have the ability to observe the progenitor stars of supernovae directly; it is usually difficult to predict when a given star will explode, and most are in galaxies too distant to allow observation of individual stars. Instead, we typically must leverage our understanding of the explosions themselves to reveal the nature of the stars that produced them. Using analytical and numerical calculations, it is possible to predict the supernovae from certain types of stars and work backwards.

In this thesis, we present a new model for previously elusive rapidly fading supernovae, which we believe are due to the core-collapse explosions of massive stars inside extended hydrogen-free envelopes or previously ejected mass shells. This model requires not only pre-explosion stellar radii of unprecedented size for hydrogen-free stars but also a lack of radioactive nickel, which is usually present in supernovae. We show our process from simple toy models to self-consistent explosions of stellar models and compare our results to existing rapidly fading supernovae. Understanding these unusual transients will shed light on the many possible ways stars behave shortly before death and also may be critical for understanding the population of core-collapse supernovae as a whole.

PUBLISHED CONTENT AND CONTRIBUTIONS

Kleiser, I. K. W., Kasen, D., & Duffell, P. C., 2018a, Monthly Notices of the Royal Astronomical Society, 475, 3152, DOI: 10.1093/mnras/stx3321, arXiv: 1801.01943 [astro-ph.HE],
I.K. participated in the conception of the project, designed models, developed and ran simulation code, participated in analysis, and led authorship of the paper.

Kleiser, I., Fuller, J., & Kasen, D., 2018b, ArXiv e-prints, arXiv: 1809.09103 [astro-ph.HE],
I.K. participated in the conception of the project, ran simulations, and led authorship of the paper.

Kleiser, I. K. W., & Kasen, D., 2014, Monthly Notices of the Royal Astronomical Society, 438, 318, DOI: 10.1093/mnras/stt2191, arXiv: 1309.4088 [astro-ph.HE],
I.K. participated in the conception of the project, ran simulations and compared the results to data, participated in analysis, and led authorship of the paper.

CONTENTS

LIST OF FIGURES

LIST OF TABLES

Chapter 1

INTRODUCTION

Over the last century since the discovery of supernovae (SNe), the explosive deaths of stars (Baade & Zwicky 1934), the field has evolved from a study of single objects to a study of populations. Where once these transients were a rare find, because of new transient surveys (Filippenko et al. 2001; Kaiser et al. 2002; Law et al. 2009) we now have swiftly growing archives of recorded SNe with a zoo of different species, including many events that defy classification and evade our understanding of their origins. This thesis focuses on the nature of massive stars that have undergone significant mass stripping throughout their lives and on the core-collapse supernovae they then produce. We further turn our attention specifically to rapidly fading supernovae (RFSNe), which constitute a small but growing class of explosions (Poznanski et al. 2010; Kasliwal et al. 2010; Drout et al. 2014; Shivvers et al. 2016) that we believe to be the core-collapse explosions of massive stars under unusual conditions, although others have proposed very different scenarios for their origins. Developing a good grasp of this topic requires an understanding of the following: 1) progenitor star structures and how they affect the available power sources of SNe; 2) the effects of mass loss on the star structure; and 3) the influence these factors have on the observational appearance and type of SN that results from a given progenitor star.

The task of connecting SNe to their progenitor stars is one of the primary themes of supernova (SN) research. Generally, a SN discovery will not be accompanied by a direct detection of its progenitor star (see e.g. Smartt 2009; Van Dyk et al. 2014, for exceptions), which would require obtaining images of the star prior to its explosion. Because SNe are rare (roughly one per 50-100 years per star-forming galaxy (Tammann et al. 1994; Cappellaro et al. 1999; Mannucci et al. 2005)), the vast majority are only detected in fairly distant galaxies, and resolving individual stars in these galaxies often either is not possible or would require the most powerful telescopes we have. Furthermore, it is usually extremely difficult to predict when a SN will occur, so high-resolution images of most host galaxies do not exist because it is not known ahead of time which ones will produce SNe in our lifetime. Understanding which progenitors give rise to which SNe then falls largely to analytical and numerical analyses of the SN observables themselves. This

endeavor is not only interesting in its own right, but it also has direct implications for many other areas of astrophysics, including galactic evolution (see §7.3) and the mass distributions of compact objects such as black holes and neutron stars (§7.2).

1.1 Core-Collapse Progenitor Star Structures and Power Sources

Not only are SNe themselves are useful probes for the properties of their progenitor stars, they are usually the only way of gaining any knowledge about the stars that produced them. In this work, we are not concerned with actual explosion mechanisms or dynamics, but rather what is ultimately observed given a certain progenitor system, explosion energy, and amount and distribution of radioactive nickel. We also focus on core-collapse SNe (CCSNe) from massive stars and not thermonuclear disruptions of white dwarfs.

The final structure of the progenitor star is critical for determining the shape of the SN light curve. The primary effects on this structure are the mass loss history (or mass gain) throughout the star's life and any activity during late burning phases that could increase the radial extent of the stellar envelope or even dynamically eject some material that could interact with the ejecta from the final explosion. Mass loss will typically involve the loss of part or all of the outer hydrogen-rich envelope, which of course affects the spectroscopic variability among core-collapse SNe with the presence or absence of hydrogen lines and their relative strength over the lifetime of the SN. There is some debate over whether additional mass loss digging into the helium layer can account for the presence or absence of helium lines found in H-poor SNe as well (Filippenko 1997; Piro & Morozova 2014).

The existence and extent of the hydrogen layer also dramatically affects the light curve because it can be very spatially extended. The greater the extent of the stellar envelope, the more thermal energy will be available from radiative cooling after the shock has run through the extended material (Popov 1993; Kasen & Woosley 2009). For this reason, H-rich stars, which have large radii because of this fluffy hydrogen layer, have a strong shock cooling component. However, the shock cooling component can be enhanced for both H-rich and H-poor stars if some of the stellar material is simply brought out to a larger radius. In some cases, the material may be unbound and considered circumstellar material (CSM) at the time of the explosion. These cases are generally thought of as interaction-powered SNe resulting from the collision of the ejecta with a shell or wind that is distinct from the star itself (see e.g. Smith et al. 2014). In other cases, there may be a bound envelope that has attained

large radii hydrostatically.

The other typical contribution to the light curve is radioactive ^{56}Ni, which is synthesized in the explosion and decays to ^{56}Co, which in turn decays to ^{56}Fe and emits gamma-rays. These gamma-rays then encounter the ejected material and thermalize, and they are reprocessed into optical and other wavelengths. Most SNe are powered primarily by either shock cooling or nickel decay or a combination of the two. There are other, more exotic SN power sources (see §7.4), but these two most common types are the only ones we consider in detail in this thesis.

1.2 The Importance of Binarity

When discussing the mass loss histories of massive stars, it is unwise to omit the possibility of binary. For the first few decades of systematic SN research, it was typically assumed that the progenitors evolved and died as single stars. In this case, the primary mass loss mechanism for massive stars would be the radiation-driven wind, in which radiation from the star itself imparts the material in its outermost layers with momentum and casts it off. The strength of this wind increases with opacity (which is composition- and wavelength-dependent) and of course with the luminosity of the star. Because the luminosity of the star increases with mass (roughly $L \propto M^3$ on the Main Sequence; the actual power varies in different regions of the Main Sequence but L always increases strongly with M), the inference would be that only the most massive stars will ultimately lose enough material to be fully H-stripped at the time of explosion.

Unfortunately, the observed fraction of stars at the high end of the initial mass function (IMF) does not seem sufficient to explain the quantity of H-free SNe that have been discovered (Smith et al. 2011). Additionally, it appears that wind mass loss rates should be lower than previously expected, making it even more difficult from wind-driven mass loss in single stars to account for the number of SNe from highly mass-stripped stars. It is necessary therefore to consider that many, if not most, H-stripped SNe originate from binary systems, in which the progenitor star could lose large amounts of mass to a companion through Roche Lobe overflow regardless of its original mass. This conclusion is further supported by recent observations of nearby massive star clusters, in which $\sim 2/3$ of massive stars live with binary companions close enough that the stars will exchange mass at some point (Sana et al. 2012). There are several channels through which massive stars may become H-free, but binarity should be prevalent among them (see §7.1 for

further discussion). Therefore we use the fact that binary interaction could remove arbitrary amounts of mass from a progenitor star in order to explore the effects of variable mass loss on our SN calculations.

1.3 Common Observational Types of CCSNe

In order to tie different progenitor scenarios to the SNe they produce, it is important to understand the various observational classifications of these explosions and how those relate to the physical structure and composition of the progenitor star. The observational types of SNe are primarily based on the presence or absence of certain spectroscopic features as well as the shapes of their light curves. As we have discussed previously, these classifications will be affected by both the mass loss history and the final structure of the progenitor. We review the common types of core-collapse SNe here and discuss how these types are related to the lives of their stars, but Filippenko (1997) presents a useful review of SN types in greater detail.

The first branch of distinction is between SNe that are spectroscopically rich or poor in hydrogen, with Type I being hydrogen-free and Type II hydrogen rich. This is usually determined by the presence or absence of the Hα feature at 6563 angstroms, though Hβ is often visible as well. Core-collapse SNe of Type I are further subdivided into SNe Ib and SNe Ic based on whether features of helium are visible. The general assumption is that the sequence of Types II, Ib, and Ic represents a sequence of increasing mass loss prior to explosion, so the H shell is removed between Types II and Ib, and the He shell is removed between Types Ib and Ic. There is often some difficulty in distinguishing SNe Ib and Ic, however, so they are often grouped in a "Ibc" category. In fact, it may not be differences in mass loss but the presence or absence of nickel mixed into the ejecta that determines whether He lines are excited and therefore whether the SN is classified as Ib or Ic (Piro & Morozova 2014).

SNe II are also subdivided based on light curve shape. Many H-rich SNe exhibit an initial period of relatively constant luminosity for $\sim$ 100 days before dropping off, for which they are named Type II-plateau SNe or "SNe IIP". Some decline more linearly (in magnitude space) and are called SNe IIL. There are also now many instances of "SNe IIb", so named because they show hydrogen features at early times, but these later disappear and the SN resembles those of the Ib variety. SNe IIb may represent an intermediate case between SNe IIP and Ib in which a very small amount of hydrogen remains at the time of the SN and is quickly overtaken by the

explosion. It is thus far unclear whether these are three distinct categories (Arcavi et al. 2012) or whether there is some continuum between them. However, it is well established that the plateau seen in SNe IIP is due to the near-constant radius of the photosphere, dictated by the recombination of the exploded H envelope as it cools and expands outward (Popov 1993), so the variety in light curve shapes among SNe II could be largely due to variability in prior mass loss.

Light curves of SNe II tend to be dominated by shock cooling energy, which is released gradually based on the recombination temperature of hydrogen, $\sim 10^3$ K. There is typically also some contribution of radioactive nickel, which is dominant at later times once the hydrogen envelope becomes transparent. Most SNe Ibc, however, do not show any obvious shock cooling component, and they are usually dominated by nickel power.

Many variations on these common types of SNe have appeared in recent decades. One example relevant to understanding the focus of this work is the Type IIn SN, so named because it shows "narrow" features of hydrogen rather than the broad features typically seen in fast-moving ejecta of typical SNe II. The commonly accepted explanation for these features is that the ejecta from the explosion are running into and interacting with slow-moving CSM that is H-rich, exciting these narrow features. In line with this explanation is the fact that some of these SNe IIn are very bright compared with more normal CCSNe, since the interaction with the CSM provides an additional power source on top of the nickel power and whatever shock energy is available in the ejecta itself.

In a sense, the power from SNe IIn or interacting SNe is analogous to that of the shock cooling power seen in SNe IIP, but the progenitor "envelope" is so extended that the shock can still be seen running through it as the SN is observed. This analogy will be an important theme in understanding the nature of the RFSNe that are the focus of this work.

1.4 Rapidly Fading Supernovae and SNe Ibn

The bulk of the work in this thesis centers around the relatively new class of rapidly fading supernovae (RFSNe), whose peak luminosities are variable and whose decline times are very rapid, in the range of roughly 10 days. Most are spectroscopically similar to SNe Ibc, but they do not exhibit the radioactive decay tails of typical H-stripped CCSNe. There is some controversy over the nature of their progenitor stars; originally it was assumed that these events did not originate from massive

stars at all but might be thermonuclear disruptions on the surfaces of white dwarfs (Kasliwal et al. 2010). In more recent years, several lines of evidence suggest that they may in fact originate from massive stars, as discussed in Drout et al. (2014) and Tauris et al. (2015) as well as the papers incorporated into this thesis.

Here we explore the possibility that these objects are primarily shock-cooling light curves from massive stars with extended H-free envelopes and with little or no contribution from radioactive nickel. The power source would be analogous to that of SNe IIP or IIn, i.e. dominated by the thermal energy left by the shock after it runs through the stellar envelope and/or CSM. Either their H-stripped progenitor stars would have to become extended enough to provide significant shock cooling energy, or some pre-SN activity may be necessary to take material out to large distances to produce bright shock-cooling light curves.

In fact, a new observational class of SNe "Ibn", which show helium narrow lines, includes at least one of these RFSNe (Shivvers et al. 2016), as well as some that are longer-lived and have more typical Ibc light curves or double-peaked light curves (see e.g. Pastorello et al. 2016, and references therein). This suggests that RFSNe may be examples of "interaction" of the ejecta with extended He-dominated material, supporting the central proposition of this thesis. Further observational testing of this model (see §7.5) and more detailed simulations will be required to definitively pin down whether it adequately explains the growing population of RFSNe, but we present here an argument in favor of the concept that CCSNe from extended H-stripped stars are viable candidate progenitors for these unusual explosions.

1.5 Overview

Chapter 2 contains an overview of the main simulation codes used in this thesis, and we describe in detail the hydrodynamics code built for this work. In Chapter 3, we show exploratory efforts conducted using all three simulation codes in stellar evolution, explosion hydrodynamics, and radiative transfer. Chapter 4 is a study of RFSNe using only radiative transfer calculations with parameterized ejecta structure, and this chapter represents the initial motivation or modeling RFSNe as CCSNe. We expand upon this work in Chapter 5 by obtaining ejecta structures from exploded stellar models, although we add toy circumstellar shells to the stellar models prior to explosion. In Chapter 6, we show that extended envelopes can be obtained for certain H-stripped stars naturally, without adding a circumstellar shell, and that these stars can be exploded to reproduce the bulk properties of RFSNe. Chapter 7

contains a review of connections to and implications for other areas of astrophysics. Finally, we provide conclusions and discussion of future directions for this work in Chapter 8.

Chapters 4-6 were originally written as three papers, two of which are published in MNRAS and one of which is in preparation for submission.

References

Arcavi, I., Gal-Yam, A., Cenko, S. B., et al., 2012, ApJL, 756, L30, L30

Baade, W., & Zwicky, F., 1934, Proceedings of the National Academy of Science, 20, 254

Cappellaro, E., Evans, R., & Turatto, M., 1999, A&A, 351, 459

Drout, M. R., Chornock, R., Soderberg, A. M., et al., 2014, ApJ, 794, 23, 23

Filippenko, A. V., 1997, ARA&A, 35, 309

Filippenko, A. V., Li, W. D., Treffers, R. R., & Modjaz, M., 2001, in Astronomical Society of the Pacific Conference Series, IAU Colloq. 183: Small Telescope Astronomy on Global Scales, ed. B. Paczynski, W.-P. Chen, & C. Lemme, Vol. 246, 121

Kaiser, N., Aussel, H., Burke, B. E., et al., 2002, in Proc. SPIE, Survey and Other Telescope Technologies and Discoveries, ed. J. A. Tyson, & S. Wolff, Vol. 4836, 154

Kasen, D., & Woosley, S. E., 2009, ApJ, 703, 2205

Kasliwal, M. M., Kulkarni, S. R., Gal-Yam, A., et al., 2010, ApJL, 723, L98

Law, N. M., Kulkarni, S. R., Dekany, R. G., et al., 2009, PASP, 121, 1395

Mannucci, F., Della Valle, M., Panagia, N., et al., 2005, A&A, 433, 807

Pastorello, A., Wang, X.-F., Ciabattari, F., et al., 2016, MNRAS, 456, 853

Piro, A. L., & Morozova, V. S., 2014, ApJL, 792, L11, L11

Popov, D. V., 1993, ApJ, 414, 712

Poznanski, D., Chornock, R., Nugent, P. E., et al., 2010, Science, 327, 58

Sana, H., de Mink, S. E., de Koter, A., et al., 2012, Science, 337, 444

Shivvers, I., Zheng, W. K., Mauerhan, J., et al., 2016, MNRAS, 461, 3057

Smartt, S. J., 2009, ARA&A, 47, 63

Smith, N., Li, W., Filippenko, A. V., & Chornock, R., 2011, MNRAS, 412, 1522

Smith, N., Mauerhan, J. C., & Prieto, J. L., 2014, MNRAS, 438, 1191

Tammann, G. A., Loeffler, W., & Schroeder, A., 1994, ApJS, 92, 487

Tauris, T. M., Langer, N., & Podsiadlowski, P., 2015, MNRAS, 451, 2123

Van Dyk, S. D., Zheng, W., Fox, O. D., et al., 2014, AJ, 147, 37, 37

Chapter 2

NUMERICAL CODES

In this thesis, we use several simulation codes to reproduce the properties of SNe at each stage from the birth of the star to the optical signature released by its explosion. We use these codes either independently or in series to answer questions about CCSNe—with particular focus on explosions of hydrogen-stripped massive stars in binaries and RFSNe—throughout this work. Stellar models are created in MESA, which we can then explode with our own in-house hydrodynamics code; finally, the ejecta structure is fed into SEDONA for the radiation transport calculation. However, there are some cases in which a simplified ejecta structure is used instead of an exploded star, such as in Chapter 4. There is also exploratory work in Chapter 3 that delves more into MESA stellar evolution itself and examination of the explosions from those stellar models.

2.1 Stellar Evolution with MESA

To obtain models of stars at the end of their lives, we use Modules for Experiments in Stellar Astrophysics (MESA), an open-source 1D stellar evolution code (Paxton et al. 2011). MESA is designed to simultaneously solve structure and composition equations and has available a suite of modules for the equation of state, opacities, nuclear reaction networks, and other physics important to the evolution of a wide range of stellar, compact object, and planetary models. It uses sophisticated adaptive mesh refinement and time step adjustment. MESA also allows mass loss through various wind models or prescribed mass loss rates; and it can allow for mass accretion. More recently, binary evolution has been implemented in MESA, and this is an active area of development (Paxton et al. 2015). New hydrodynamics capabilities have also been introduced to explode massive stars at core-collapse, although we do not use that functionality in this work, instead using our own hydrodynamics code.

2.2 Explosion Hydrodynamics

Setup and Algorithm

The explosions are simulated in a 1D staggered moving-mesh hydrodynamical code. The utility of using a Lagrangian code is that it accommodates many scales, and the

ejecta can be expanded out to the homologous expansion phase without re-gridding. We adapt the 1D Lagrangian setup from Castor (2004). Quantities defined at the zone boundaries (e.g. radii and velocities) are denoted by the subscripts I, and the properties of the zones, defined at the zone centers (e.g. densities, internal energies, and pressures) are denoted by subscripts $I - 1/2$.

The initial properties of the simulation are read from an input file, which contains information for N zones, the inner radius $r_{\rm inner}$, initial time $t_{\rm init}$, number of ions $n_{\rm ions}$, A_i for each ion, and Z_i for each ion. Each zone I of the N zones is read into a structure of zones and has outer radius r_I, outer boundary velocity v_I, cell density $\rho_{I-1/2}$, cell pressure $p_{I-1/2}$, and cell mass $m_{I-1/2}$. The sound speed $c_{s,I-1/2}$ in each zone is then calculated from $\sqrt{\gamma \frac{p_{I-1/2}}{\rho_{I-1/2}}}$, and the energy is approximated as $e_{I-1/2} = \frac{1}{\gamma-1}\frac{p_{I-1/2}}{\rho_{I-1/2}}$.

The grid includes one inner and one outer ghost zone. At each time step, these are used to apply boundary conditions—first, the outer radius of the inner ghost zone $r_0 = r_{\rm inner}$ and is either set to a constant radius (e.g. in the thermal bomb case) or is moved as a function of time, i.e. to implement a piston. The outer ghost zone is used to determine the acceleration of the outer zone's radius r_N. The important quantity here is the pressure, which is extrapolated linearly from previous zones as

$$p_{N+1} = p_N + \frac{p_N - p_{N-1}}{r_N - r_{N-1}}(r_{N+1} - r_N) \ .$$

If there is a piston in the simulation, its evolution is determined by the piston velocity $v_{\rm pist}$ and explosion energy $E_{\rm exp}$ input by the user. The code calculates the maximum radius to which the piston should travel in order to impart the inner zones with roughly $E_{\rm exp} = \frac{1}{2}M_{\rm kin}v_{\rm pist}^2$, where $M_{\rm kin}$ is the sum of the masses of the inner few zones imparted with this kinetic energy. That is, the code sequentially adds the mass of the innermost zone, the second zone, and so forth until the total $\frac{1}{2}Mv_{\rm pist}^2$ exceeds the specified kinetic energy. This is only a rough estimate, however, and $E_{\rm exp}$ as an input may need to be adjusted in order to inject the desired amount of energy.

In thermal bomb mode, $v_{\rm inner}$ is set to zero, so $r_{\rm inner}$ does not move. Instead, the explosion energy $E_{\rm exp}$ is inserted in the form of thermal energy in the innermost layers. How many of these zones are impulsively imparted with this energy is determined by a thermal mass $M_{\rm therm}$ adjusted as a parameter. The code calculates approximately how many of the inner zones need to participate in order to spead the energy over $M_{\rm therm}$, and these zones receive internal energy $e_{I-1/2} = E_{\rm exp}/M_{\rm therm}$.

Again, this is approximate and may need to be adjusted in order to put the required energy in.

In the time loop, the first step is to calculate the new time step using the Courant-Friedrichs-Lewy (CFL) condition. There are several relevant timescales to consider. One is the maximum time step $dt_{\rm max}$ supplied by the user. The second is the sound-crossing time $dt_{cs} = \frac{dr}{c_s}$, where dr is the width of the zone. The third is the time for a zone to grow or shrink by its own size through the motion of its boundaries, $dt_v = \frac{dr}{v_{I-1} - v_I}$. The new time step is found by finding $\min(dt_{cs}, dt_v)$ and multiplying by some CFL constant, usually around 0.25 or 0.5. The minimum value for this product $dt_{\rm new}$ across all zones is found, and if it is less than $dt_{\rm max}$, then this is the new time step.

One caveat is that the time step is calculated before the velocities are updated, so the zone boundaries may pass through one another, which is unphysical, and create zones of negative volume. To prevent this problem, the time step calculation runs a check for negative volumes and reduces the time step until this does not occur.

The next step is to update the zone boundary velocities:

$$u_I^{n+1/2} = u_I^{n-1/2} + (t_{n+1} - t_{n-1}) \frac{p_{I-1/2}^n + q_{I-1/2}^n - p_{I+1/2}^n - q_{I+1/2}^n}{m_{I-1/2} + m_{I+1/2}} 4\pi (r_I^n)^2 - (t_{n+1} - t_{n-1}) \frac{GM_I}{2(r_I^n)^2} \, ,$$

where $M_I = \sum_{j=1}^{I-1} m_{j+1/2} + M_{\rm remnant}$ is the mass interior to the zone, including the mass of the remnant. The gravitational term is only added if gravity is turned on. Next the zone positions can be moved as

$$r_I^{n+1} = r_I^n + (t_{n+1} - t_n) u_I^{n+1/2} \, ,$$

and new densities are found for each zone using the (constant) zone masses and new radii:

$$\rho_{I-1/2}^{n+1} = \frac{m_{I-1/2}}{\frac{4\pi}{3}[(r_I^{n+1})^3 - (r_{I-1}^{n+1})^3]} \, .$$

Pseudo-viscosity is implemented as

$$q_{I-1/2}^{n+1} = C_Q \rho_{I+1/2}^{n+1} \max(u_{I-1}^{n+1/2} - u_I^{n+1/2}, 0)^2 \, ,$$

where C_Q is an adjustable constant that is usually $\sim 1 - 4$. This essentially removes kinetic energy by reducing the velocities of the zones and converts it to internal

energy on the grid. The pseudo-viscosity is set to zero in any zone that is expanding (so free expansion is not affected) but comes into play in any zone that is under compression. This is used to reduce artificial oscillation in the simulation, but too much viscosity can smooth out shocks unrealistically.

The internal energy is calculated with a γ-law equation of state, assuming $\gamma = 4/3$ for radiation-dominated ejecta. The energy calculation is implicit and has the form

$$e^{n+1}_{I-1/2} = e^{n}_{I-1/2} - \frac{1}{2}(p^{n}_{I-1/2} + p^{n+1}_{I-1/2} + q^{n}_{I-1/2} + q^{n+1}_{I-1/2})\left(\frac{1}{\rho^{n+1}_{I-1/2}} - \frac{1}{\rho^{n}_{I-1/2}}\right) .$$

This can be converted to an explicit form by using the γ-law equation of state, which is used to solve for the pressure at the new time step:

$$p^{n+1}_{I-1/2} = (\gamma - 1)\rho^{n+1}_{I-1/2} e^{n+1}_{I-1/2} .$$

Plugging this expression into the equation for internal energy allows us to rearrange and solve explicitly for $e^{n+1}_{I-1/2}$, giving

$$e^{n+1}_{I-1/2} = \frac{e^{n}_{I-1/2} - \frac{1}{2}(p^{n}_{I-1/2} + q^{n}_{I-1/2} + q^{n+1}_{I-1/2})\left(\frac{1}{\rho^{n+1}_{I-1/2}} - \frac{1}{\rho^{n}_{I-1/2}}\right)}{1 + \frac{1}{2}(\gamma - 1)\rho^{n+1}_{I-1/2}\left(\frac{1}{\rho^{n+1}_{I-1/2}} - \frac{1}{\rho^{n}_{I-1/2}}\right)} .$$

Once the internal energies and pressures for each zone are calculated, the sound speeds are updated to

$$c^{n+1}_{s,I-1/2} = \sqrt{\gamma \frac{p^{n+1}_{I-1/2}}{\rho^{n+1}_{I-1/2}}}$$

for the next time step calculation.

Basic Hydrodynamics Tests

Sod Shock Tube Test

Figure 2.1 shows a comparison of the numerical solution for the shock tube test with the semianalytical solution from Timmes (2018). The density ρ is shown as a function of distance x at $t = 0.4$ s. The original quantities are $\rho_0 = 10$ g cm^{-3} and $P_0 = 100$ dyn cm^{-2} for $x < 2$ cm and$\rho_0 = 1$ g cm^{-3}, $P_0 = 10$ dyn cm^{-2} for $x > 2$ cm, and $\gamma = 1.4$.

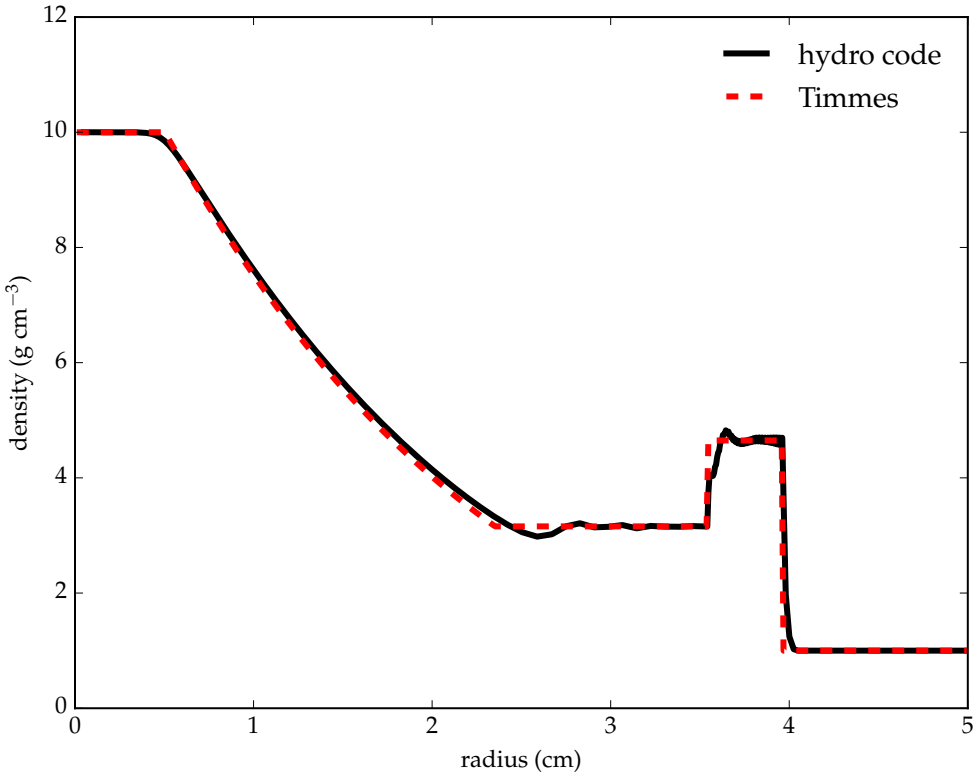

Figure 2.1: Density as a function of radius for the Sod Shock tube test. Our results are compared with the semianalytical solution from Timmes (2018).

Sedov Blast Wave Test

Using dimensional analysis, we can estimate the radius of the blast wave as a function of time,

$$r = \xi_0 (E_0/\rho_0)^{1/5} t^{2/5} \ , \tag{2.1}$$

where ξ_0 is a constant factor of order 1. The velocity of the shock is then

$$v_{\rm blast} = \frac{2}{5} \xi_0 (E_0/\rho_0)^{1/5} t^{-3/5} \ .$$

We can plug in for t to get

$$v_{\rm blast} = \frac{2}{5} \xi_0^{5/2} \left(E_0/\rho_0 \right)^{1/2} r^{-3/2} \ .$$

The pressure in the shocked region goes as

$$P \sim \rho v_{\rm blast}^2 = \frac{4}{9} \xi_0^5 E_0 r^{-3} \ .$$

Since the post-shock fluid is radiation-dominated, $P = \frac{1}{3}aT^4$. This allows us to solve for the temperature behind the shock,

$$T \sim \left(\frac{E_0}{ar^3}\right)^{1/4},$$

similar to the relationship found in Woosley et al. (1995). This expression can be used to approximate the post-shock temperature at the time of shock breakout for a supernova:

$$T_{\rm sb} \sim 1.4 \times 10^8 \text{ K} \left(\frac{E_0}{10^{51} \text{ erg}}\right)^{1/4} \left(\frac{R_*}{R_\odot}\right)^{-3/4}. \tag{2.2}$$

For a given explosion energy of, say 10^{51} erg, the shock breakout temperature will be determined by the pre-supernova radius of the progenitor. For a compact star of a few solar radii, the temperature should be roughly 10^8 K, whereas the explosion of a red supergiant with $R_* \sim 300$ $R_\odot$ would have a breakout temperature closer to 2×10^6 K.

In Figure 2.2 is a comparison between the hydrodynamical solution at $t = 0.4$ s and the semianalytical solution from Timmes (2018). The original density is a constant $\rho_0 = 1$ g cm^{-3}, and the energy deposited in the first zone is 0.851072 erg. $\gamma = 1.4$ for this calculation, and the density is shown as a function of radius at a time $t = 1$ s.

2.3 Radiation Transport with SEDONA

In this work, we extensively use SEDONA (Kasen et al. 2006) to calculate artificial light curves and spectra for the supernova profiles obtained with our hydrodynamics code. SEDONA is a time-dependent Monte Carlo radiation transport code that generates and propagates photon packets through an expanding ejecta. While this code has 3D, polarization, and some radiation-hydrodynamics capabilities, in this thesis we use it only in the context of 1D (spherically symmetrical) homologously expanding ejecta. In this case, the ejecta are freely $r_{\rm out} = v_{\rm out} t_{\rm exp}$, where $r_{\rm out}$ is the outer radius of the zone, $v_{\rm out}$ is the velocity of this outer edge, and $t_{\rm exp}$ is the time since explosion. Since the velocity of each zone is constant with time, the grid uses velocity as the spatial coordinate.

Density, composition, and temperature are all used to determine the opacity and emissivity in each wavelength bin for each spatial zone. Opacities and emissivities are saved in tables prior to the calculation in order to increase computational speed. At each time step, photon packets are emitted or absorbed with a certain probability at each wavelength in each zone. The calculation is simplified with the use of the

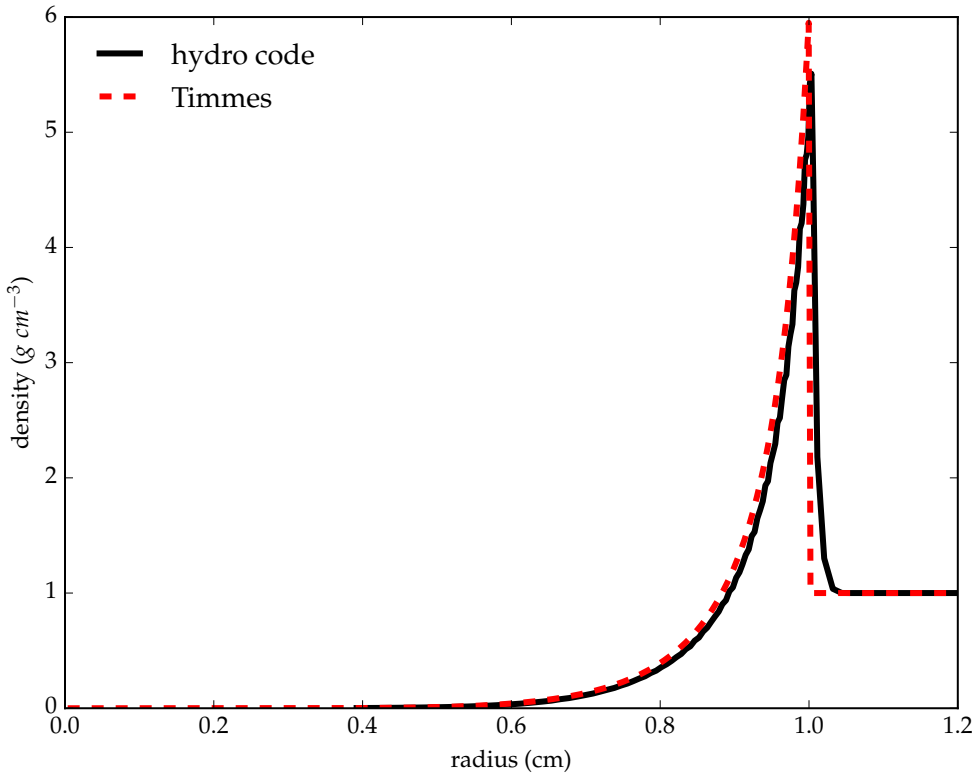

Figure 2.2: Density as a function of radius for the Sedov blast wave. The numerical solution is compared with the semianalytical solution from Timmes (2018).

Sobolev approximation, which relies on the assumption that the Doppler velocity width of the bound-bound emission and absorption lines is small compared to the velocity scale of significant changes in the ejecta. This is typically valid for SN explosions and other rapid mass outflows. In addition, we assume that the ejecta are in local thermodynamic equilibrium (LTE), so the ionization and excitation states of the material are determined exclusively by the Saha and Boltzmann equations, and there are no additional sources of ionization or excitation of electrons. Notably, some helium features common in SNe require excitation by fast electrons knocked off by gamma-rays in radioactive nickel decay, so there are important limitations introduced by the LTE assumption. However, these limitations should not significantly influence the bulk properties of most light curves and should only affect some spectroscopic features, particularly in the first weeks to months after explosion while the ejecta are still in the photospheric (as opposed to nebular) phase.

The power of SEDONA as opposed to most other radiation transport codes available is in the detailed calculation of wavelength-dependent opacities based on ejecta properties and on the Monte Carlo emission, propagation, and absorption of photon packets, which emulates the physical process of photon behavior in the ejecta. There is statistical noise associated with using discrete photon packets, and this noise is decreased if larger numbers of packets are used (each containing proportionally less radiation energy). This makes the calculation more computationally intensive, so calculations that yield detailed spectroscopic information are more expensive.

References

Castor, J. I. 2004, Radiation Hydrodynamics, 368

Kasen, D., Thomas, R. C., & Nugent, P., 2006, ApJ, 651, 366

Paxton, B., Bildsten, L., Dotter, A., et al., 2011, ApJS, 192, 3, 3

Paxton, B., Marchant, P., Schwab, J., et al., 2015, ApJS, 220, 15, 15

Timmes, F. X. 2018, http://cococubed.asu.edu/code_pages/ppm_1d.shtml

Woosley, S. E., Langer, N., & Weaver, T. A., 1995, ApJ, 448, 315

Chapter 3

END-TO-END MODELS OF SUPERNOVAE

In this chapter, we show exploratory efforts and tests in each stage of our simulation pipeline, from stellar evolution to hydrodynamical explosion to radiation transfer. In our stellar evolution runs, we explore the effect of different amounts and rates of mass loss on massive stars. For our hydrodynamics section, we show our results from adding a thermal bomb to one of these stellar models and check that they are consistent with analytic solutions. Finally, we show the light curves calculated for exploded models of several of these stars.

3.1 Stellar Evolution and Mass Loss

We use MESA to evolve stars with varying amounts of mass loss. We have chosen three initial masses $M_{\rm i}$ =15, 20, and 40 $M_\odot$, and for each we have selected several final masses. Each star is evolved through the Main Sequence and allowed to expand at the end of core hydrogen burning until the surface reaches an effective temperature $T_{\rm eff}$ = 5000 K. At this point, we implement a constant mass loss prescription of $\dot{M} = 10^{-3}$ $M_\odot$ yr^{-1}. After the desired final mass is reached, this mass loss is shut off; the star is prevented from undergoing any additional mass loss and is allowed to evolve to iron core collapse.

There are other, perhaps more natural-seeming criteria for beginning and halting mass loss, e.g. defining a Roche lobe radius and removing mass when the star's radius exceeds this; however, in an actual binary system of massive stars, angular momentum transport is complicated and may cause changes in the rotation rate of stars as well as orbital radii, influencing the shape of the Roche lobe. This is an active area of research, including with the MESA code itself (e.g. Paxton et al. 2015).

We use our simpler (and not necessarily less physical) prescription to remove mass until some specified final mass in order to probe a chosen parameter space. As long as the star is allowed to come into equilibrium after the mass loss has finished, the final structure of the star is expected to be unaffected by the mass loss history (provided it is Case B mass loss). We show below that the actual mass loss history should not important to the final structure of the star prior to explosion.

Results for 20 Solar-Mass Stars

For our $M_{\rm i} = 20\ {\rm M}_\odot$ models, the final structure of the star is determined by either how much of the hydrogen envelope remains at the end of mass loss, if any, and how much of the helium core is removed if mass loss proceeds beyond stripping the entire hydrogen envelope. If mass loss does not remove anything beyond the hydrogen envelope, the core structure between models with different final masses will be similar. Figure 3.1 shows Kippenhan diagrams for $M_{\rm i} = 20\ {\rm M}_\odot$ models, including a model with standard single-star mass loss. With no additional mass loss, the helium core increases to about 6 solar masses. Significant stripping occurs in our other $M_{\rm i} = 20\,{\rm M}_\odot$ models, but it is not until final masses as low as ~5 solar masses or less that the core structure is actually affected, as shown in Figure 3.2. The varying hydrogen envelope masses, however, will dramatically affect the light curves of the resulting supernovae. Note that with a mass loss rate of $\dot{M} = 10^{-3}\ {\rm M}_\odot/{\rm yr}$, the final mass of the star is reached well before the formation of the carbon core. If the mass loss rate is more gradual and continues into later stages of burning, it may affect the subsequent growth of cores at various stages. Based on Yoon et al. (2010), we take it to be a reasonable assumption that most or all of the mass is lost to the companion well before late stages of burning.

The Hertzsprung-Russell (HR) diagram in Figure 3.3 shows the evolution of these models in luminosity-temperature space. The runs with little or no mass loss remain roughly at the same position at low temperatures and the right-hand side of the plot. Moderate mass loss causes the surface temperature to rise, although the luminosity is roughly constant. This is because only the hydrogen envelope mass is changing, and the core structure remains the same, so the luminosity is the same but the radius is shrinking. In the case of $M_{\rm f} = 8\ {\rm M}_\odot$, the radius expands and cools again in later stages because some hydrogen is retained. Meanwhile, stars which are stripped below the threshold of their helium cores dip dramatically in both luminosity and temperature after their move blueward. Once mass loss shuts off, they are able to return close to their original luminosities but remain hot blue cores. The $M_{\rm f} = 4\ {\rm M}_\odot$ case has a slightly lower luminosity and temperature than the $M_{\rm f} = 5\ {\rm M}_\odot$ case due to the change in He core mass.

Results for 40 Solar-Mass Stars

If the stripping does remove part of the He core, other core masses (C, O, Si, Fe) will be affected, and the compactness of the star will change as well as the composition. Figure 3.4 shows the evolution of $M_{\rm i} = 40\ {\rm M}_\odot$ stars, which at the onset of mass

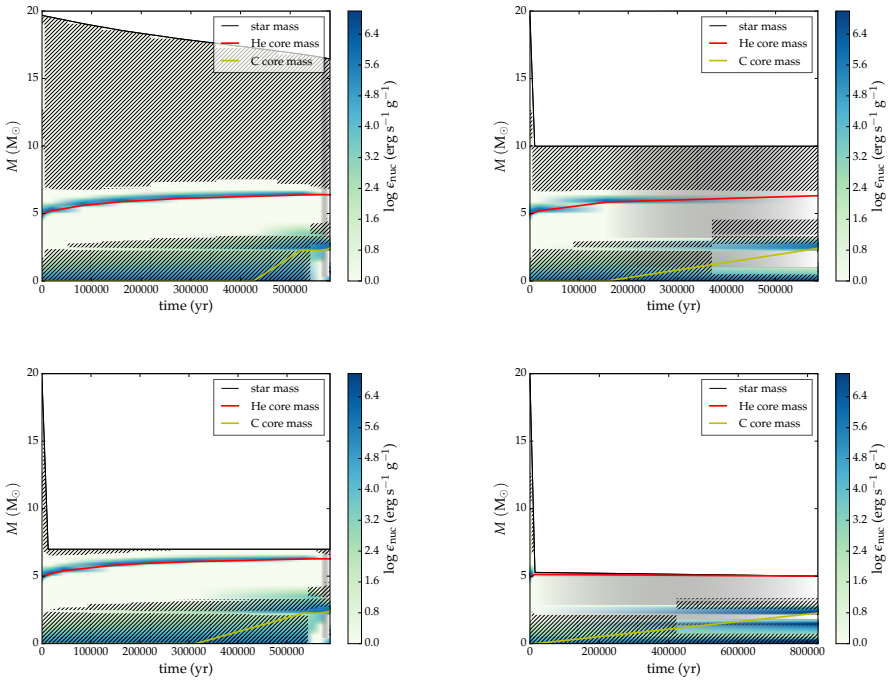

Figure 3.1: Kippenhan diagrams showing the mass loss and burning of various $M_{\rm i} = 20$ M$_\odot$ models. Convective regions are shown with hatches. For simulations with artificial stripping, the mass loss is quite fast compared to the lifetime of the star. Note that in the $M_{\rm f} = 5$ M$_\odot$ case, the stripping cuts into the helium core, while in other cases it does not.

loss have much larger He cores. The single-star model produces a helium core of just over 15 solar masses, so even stripping down to 10 M$_\odot$ cuts well into it. As can be seen in Figures 3.4 and 3.5, all models we stripped have entirely lost their hydrogen envelopes and are bare helium cores; in fact, mass loss has removed part of the helium core in different amounts, which changes the abundances of heavier elements produced.

The HR diagram evolution for $M_{\rm i} = 40$ M$_\odot$ models is shown in Figure 3.6. In every case with mass loss, the star evolves blueward then dips in both temperature and luminosity until mass loss is shut off, then the star re-expands as shown in the high mass loss runs from $M_{\rm i} = 20$ M$_\odot$ stars. The larger amount of mass loss, the more dramatically the star dims, and the more its final state is shifted to lower luminosity and temperature at core collapse.

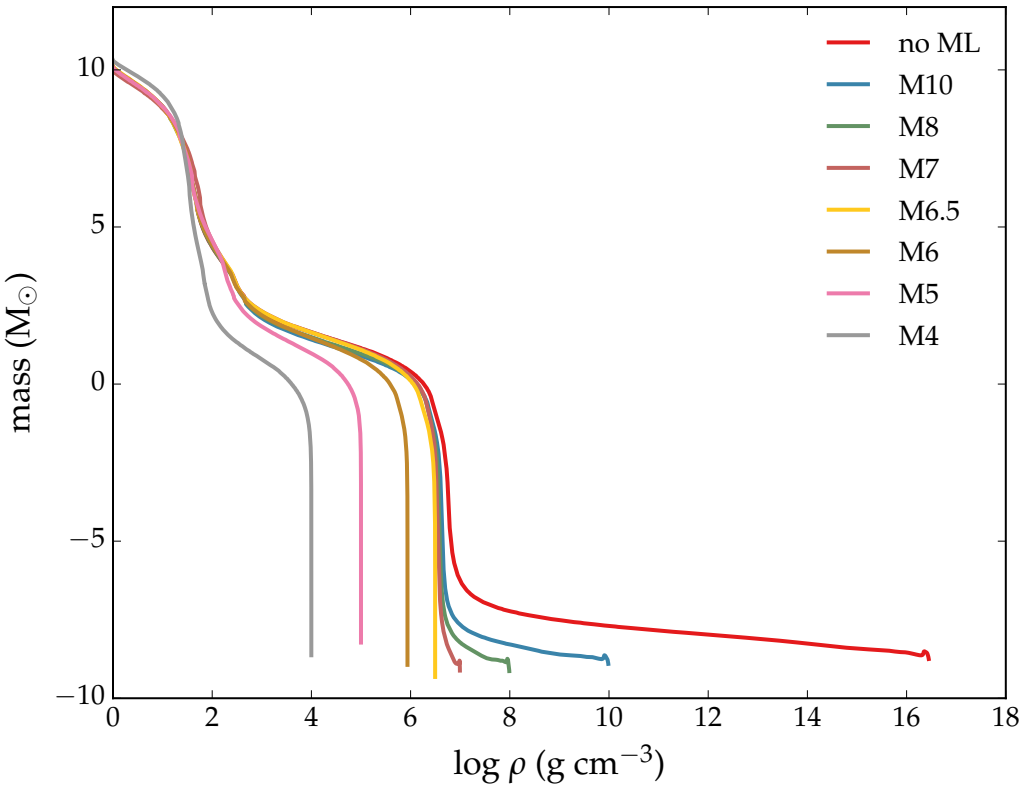

Figure 3.2: Density profiles for M_i = 20 M$_\odot$ models. The structures of these stars are very different depending on whether there is a hydrogen envelope left (and how massive it is) and also how massive the helium core is. "no ML" indicates the run without mass loss, and other legend labels indicate the final mass of the star once mass loss is shut off.

Varying Mass Loss Rates

We run several simulations from M_i = 20 M$_\odot$ to M_f = 6 M$_\odot$ with the same mass loss prescription but with different mass loss rates. As can be seen in Figure 3.7, the HR diagram evolutionary track can be quite different if different mass loss rates are assumed, particularly in the case of $\dot{M} = 10^{-2}$ M$_\odot$ yr^{-1}. The stars all end up in roughly the same region of the HR diagram, although with slightly different temperatures. This may be partly because their final masses are slightly different; as can be seen in Figure 3.8. The density profiles of these stars are quite similar, with only small structural differences. We therefore conclude that the mass loss history, as long as it occurs after the Main Sequence but before late-stage burning beyond He core burning, should not greatly affect the structure of the star.

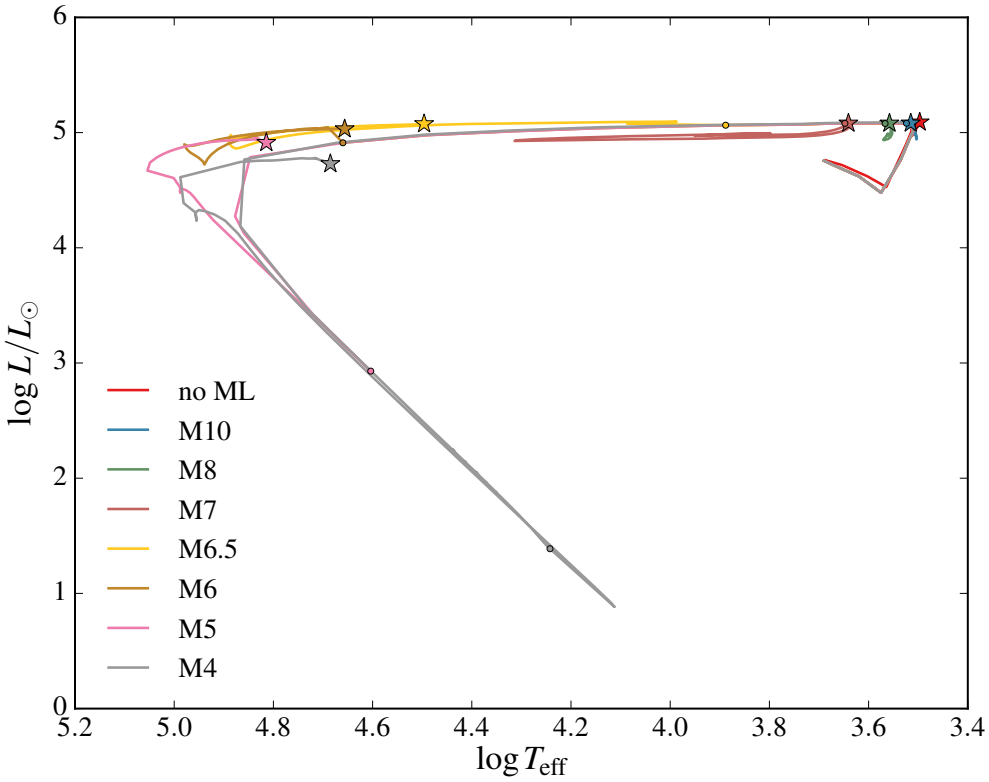

Figure 3.3: Hertzsprung-Rusell diagram showing tracks for the stellar models with $M_{\rm i} = 20$ M$_\odot$. Dots with colors corresponding to each track show the points where mass loss was shut off, and star symbols indicate the position of each star at core collapse. As mass loss occurs, stars evolve blueward. Once mass loss has removed the entire hydrogen envelope and starts removing part of the helium core, stars become dimmer and redder. When mass loss shuts off, they evolve back up in luminosity and temperature. As in Figure 3.2, legend labels indicate the final mass or no mass loss.

Compactness

While the ability of a given star to explode may be chaotic and difficult to determine by examining its pre-explosion structure, the structure is bound to at least affect the likelihood of explosion (Clausen et al. 2015). The compactness of a star has been shown to affect its ability to explode in 1D simulations (O'Connor & Ott 2011; Sukhbold et al. 2017). The compactness can be expressed as a parameter given by

$$\xi_M = \frac{M/\mathrm{M}_\odot}{R/(1000\ \mathrm{km})}\ , \tag{3.1}$$

where M is typically taken to be 2.5 M$_\odot$. This is because the mass coordinate 2.5 M$_\odot$ should be close to the mass boundary between black hole and neutron star

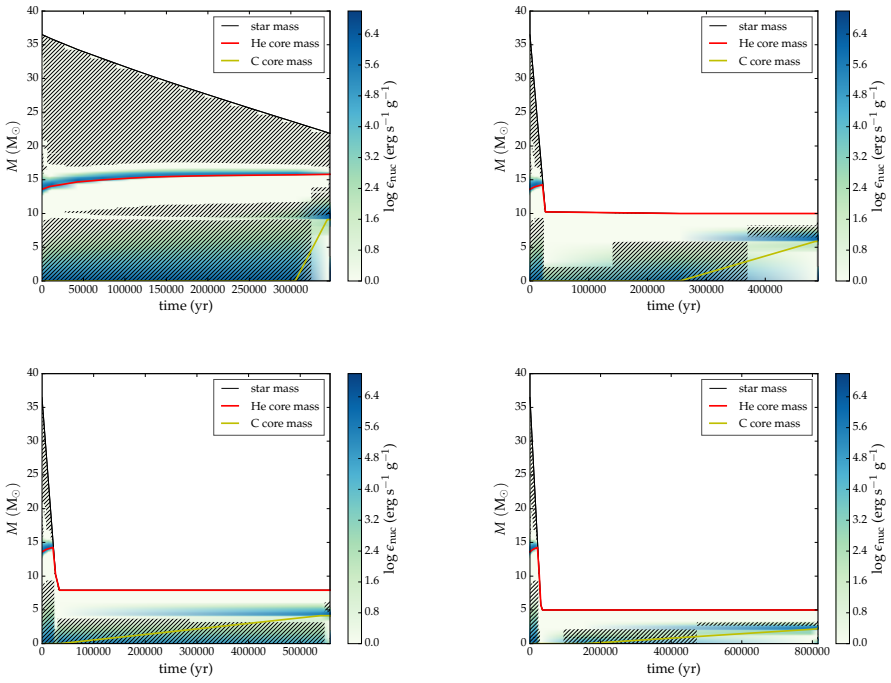

Figure 3.4: Same as Figure 3.1 but for $M_{\rm i} = 40$ M$_\odot$. In this case, all levels of mass loss shown here cut into the helium core and will change the evolution and final structure of the star.

formation. Figure 3.9 shows the compactnesses of various final models in our suite. Above $M_{\rm f} = 6$ M$_\odot$, models with $M_{\rm i} = 20$ M$_\odot$ have very similar compactness values due to the fact the the He cores remain intact. On the other hand, $M_{\rm i} = 40$ M$_\odot$ models vary dramatically, with compactness rising significantly as the He core mass increases, except for the case without artificial mass loss.

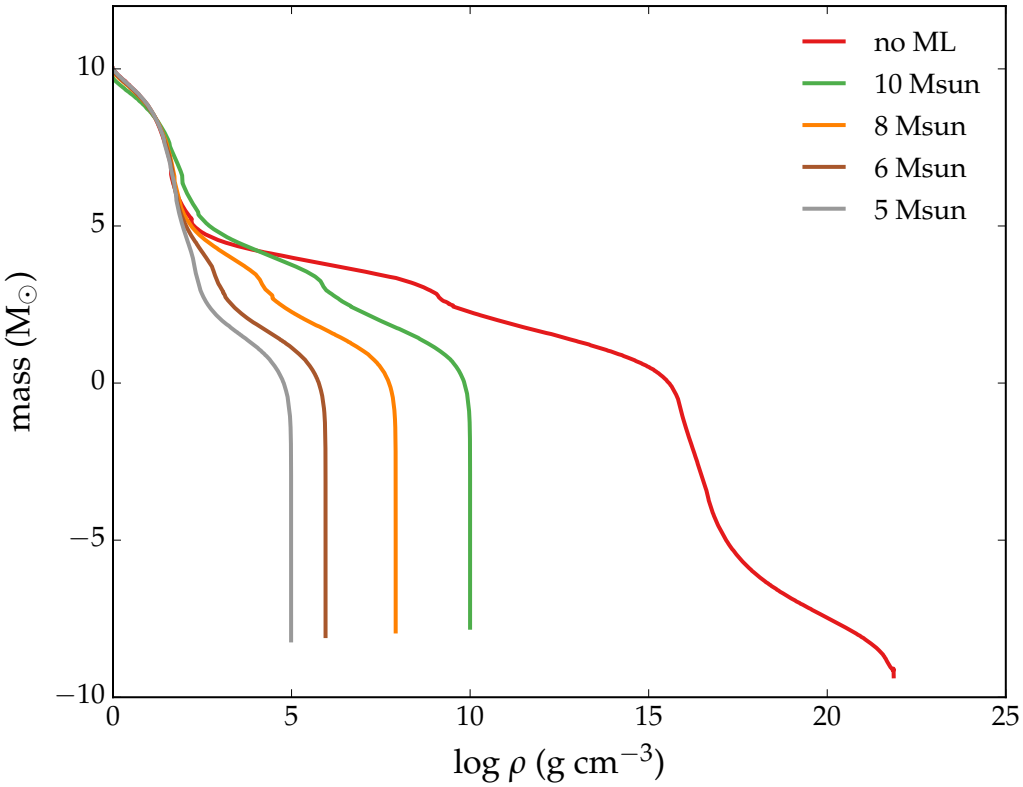

Figure 3.5: Density profiles for $M_{\rm i}$ = 40 $M_\odot$ models. Here, unlike in Figure 3.2, helium core structures are all different due to the different amounts of mass loss.

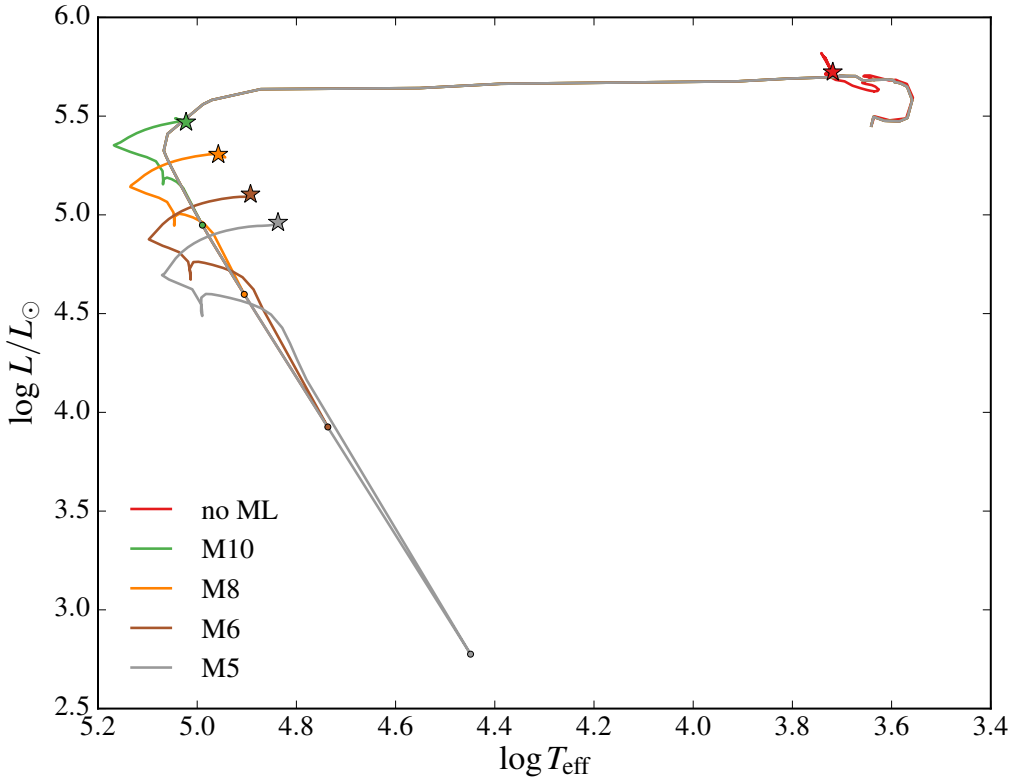

Figure 3.6: Same as Figure 3.3 but for $M_{\rm i}$ = 40 $M_\odot$. The hydrogen envelopes of all stripped stars are fully removed, and varying amounts of their helium cores are as well. Stars which experience more loss of their He cores dip farther down in luminosity and temperature before rising again after mass loss ends. All stripped models end up very blue upon explosion.

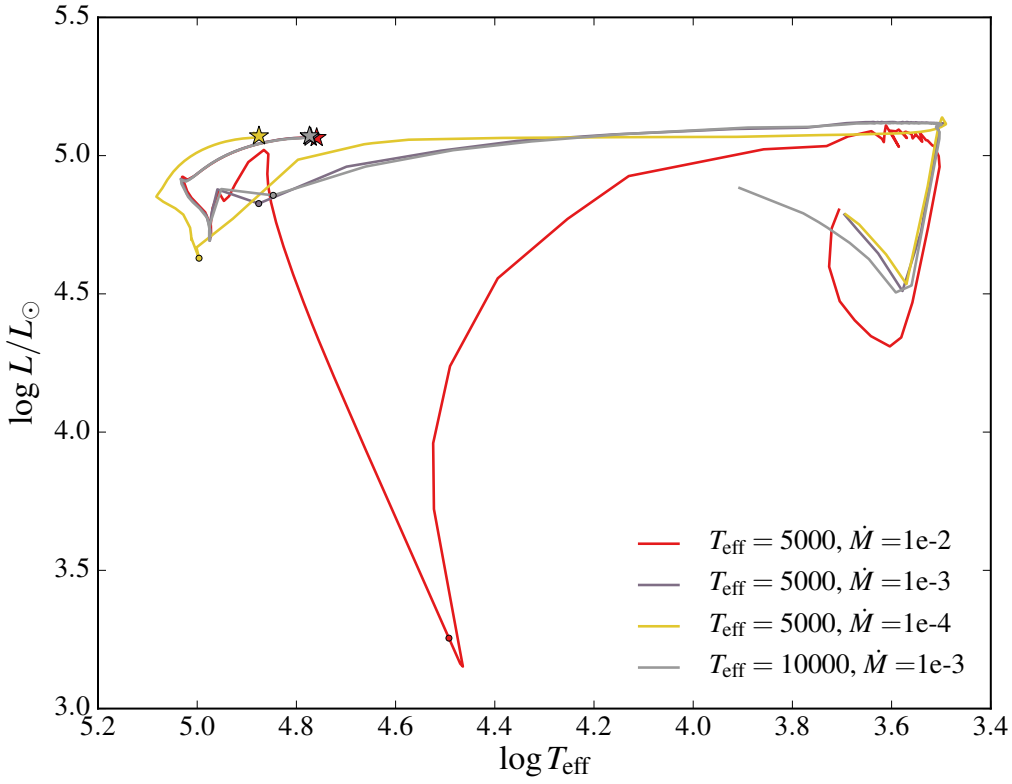

Figure 3.7: HR diagram showing the evolution of stars going from $M_{\rm i}$ = 20 $M_\odot$ to $M_{\rm f}$ = 6 $M_\odot$ but with different mass loss rates. Dots of corresponding color show where mass loss was shut off, and stars indicate the end point of the star's evolution. In one of these runs, we initiate mass loss slightly earlier, when $T_{\rm eff}$ drops to 10^4 rather than 5000 K, and the results are quite similar to the 5000 K case.

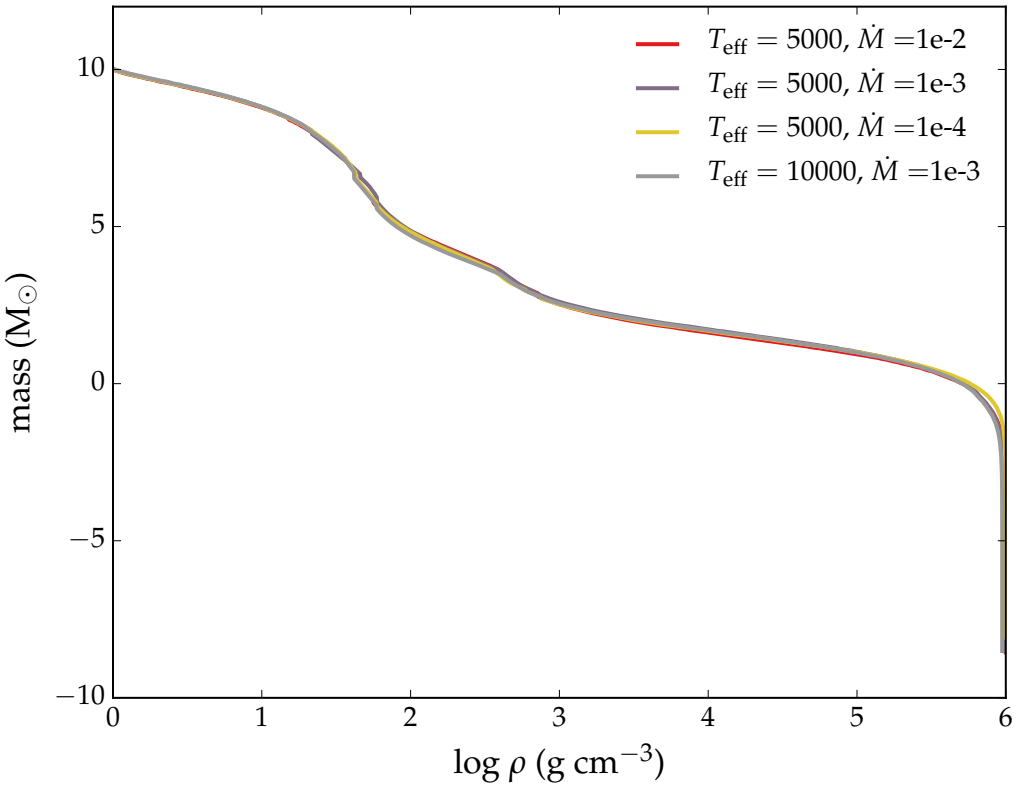

Figure 3.8: Final density profiles for the stellar models shown in Figure 3.7. Clearly the different mass loss rates do not greatly affect the final structure of the star, as long as they occur after the star leaves the Main Sequence and finish before late-stage burning phases begin.

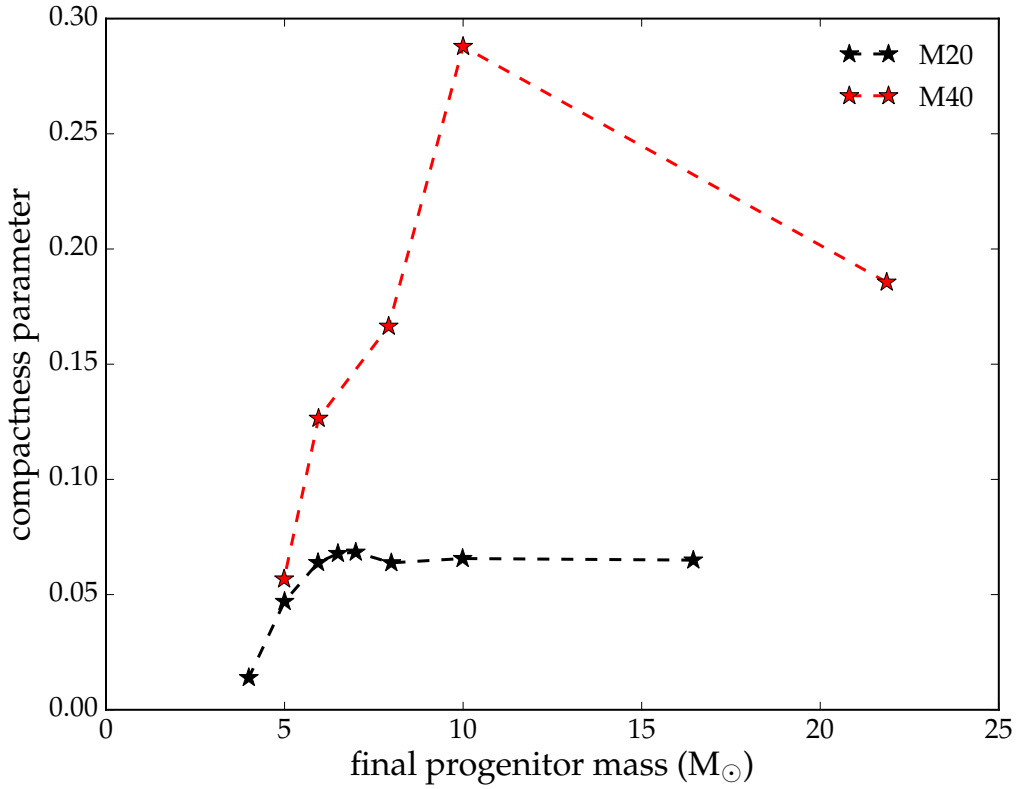

Figure 3.9: Compactness values for final stellar models. The values for $M_{\rm i} = 20\ {\rm M}_\odot$ are similar above $M_{\rm f} = 6\ {\rm M}_\odot$, likely due to the fact that their He cores are roughly the same mass. In the case of $M_{\rm i} = 40\ {\rm M}_\odot$, all stripped stars experienced mass loss down past the edge of the He core, resulting in different core masses and therefore different core structures. Stripped stars with larger He cores have final star structures with larger compactnesses. However, the $M_{\rm i} = 40\ {\rm M}_\odot$ model with normal (single star) mass loss has a lower compactness. In single-star studies, compactness does not always increase monotonically with mass, so this behavior is not surprising.

M_i ($\mathrm{M}_\odot$)	M_f ($\mathrm{M}_\odot$)	L (10^4 $\mathrm{L}_\odot$)	T_eff (K)	R ($\mathrm{R}_\odot$)	$\xi_{2.5}$	M_H	M_He	Mc_He	Mc_C	Mc_O	Mc_Si	Mc_Fe
20	3	0.77	6300	73	–	2.89×10^{-43}	1.56	3.00	1.38	1.35	0.00	0.00
20	4	5.4	4.8×10^4	3.3	1.4×10^{-2}	9.3×10^{-4}	2.06	4.00	1.84	1.61	0.00	1.45
20	5	8.2	6.5×10^4	2.2	$3.1 - 4.7 \times 10^{-2}$	6.66×10^{-7}	2.50	5.00	2.28	1.83	1.56	1.46
20	6	11	4.5×10^4	5.3	6.4×10^{-2}	3.84×10^{-2}	3.17	5.69	2.44	1.69	1.57	1.45
20	6.5	12	3.1×10^4	12	6.8×10^{-2}	8.19×10^{-2}	3.57	6.15	2.46	1.69	1.55	1.43
20	7	12	4400	600	6.9×10^{-2}	0.341	3.80	6.28	2.47	1.77	1.62	1.49
20	8	12	3600	890	6.4×10^{-2}	0.987	4.14	6.29	2.47	1.69	1.53	1.45
20	10	12	3300	1100	6.6×10^{-2}	2.31	4.76	6.32	2.47	1.79	1.56	1.44
20	16.45	12	3100	1200	6.5×10^{-2}	6.67	6.75	6.40	2.48	1.69	1.56	1.45
40	5	9.2	6.9×10^4	2.1	5.7×10^{-2}	1.92×10^{-20}	2.37	4.99	2.30	1.81	1.63	1.49
40	6	13	7.8×10^4	2.0	0.13	1.28×10^{-19}	2.64	5.95	2.88	2.34	1.63	1.50
40	8	20	9.1×10^4	1.8	0.17	6.42×10^{-20}	3.13	7.92	4.15	1.92	1.69	1.52
40	10	29	10^5	1.6	0.29	2.69×10^{-21}	3.47	10.00	5.86	2.39	1.94	1.66
40	21.86	53	5200	8.9	0.19	3.32	8.45	15.8	9.10	2.20	1.65	1.50

Table 3.1: Properties of final MESA models. Note that one run ($M_\mathrm{i} = 20\ \mathrm{M}_\odot$, $M_\mathrm{f} = 3\ \mathrm{M}_\odot$) was not run to completion, probably because late-stage shell burning for low-mass helium cores can be very computationally expensive and time-consuming.

Stellar Explosions

Analytics: Shock Jump Conditions

We can deposit energy inside a constant-density 'star' to test whether the code satisfies the Rankine-Hugoniot strong shock jump conditions. The Rankine-Hugoniot jump conditions are relationships that relate upstream (in the shock frame) quantities ρ_1, u_1, T_1 to downstream, post-shock quantities ρ_2, u_2, T_2. Assume 1D plane-parallel (which should be valid for most regions of our spherically symmetric solutions, where $dr \ll r$), steady state, and no gravity. We can also ignore viscosity for quantities outside the shock. We can start with the continuity equation, the momentum conservation equation, and the energy equation:

$$\frac{\partial \rho}{\partial t} + \vec{\nabla} \cdot (\rho \vec{u}) = 0 \longrightarrow \frac{d}{dx}(\rho u) = 0 \,, \tag{3.2}$$

$$\rho \frac{\partial \vec{u}}{\partial t} + \rho(\vec{u} \cdot \vec{\nabla})\vec{u} + \vec{\nabla} P = 0 \longrightarrow \rho u \frac{du}{dx} + \frac{dP}{dx} = 0 \,, \tag{3.3}$$

$$\frac{\partial}{\partial t}\left(\rho\epsilon + \frac{1}{2}\rho u^2\right) + \vec{\nabla} \cdot \vec{u}\left(\rho\epsilon + \frac{1}{2}\rho u^2 + P\right) = 0 \longrightarrow \frac{d}{dx}\left[\rho u\left(\epsilon + \frac{1}{2}u^2 + \frac{P}{\rho}\right)\right] = 0 \,. \tag{3.4}$$

First, from the continuity equation,

$$\rho_1 u_1 = \rho_2 u_2 \tag{3.5}$$

in steady state. We also can use

$$\rho u \frac{du}{dx} = \frac{d}{dx}(\rho u^2) - u \frac{d}{dx}(\rho u) = \frac{d}{dx}(\rho u^2) \,,$$

so

$$\frac{d}{dx}(\rho u^2) + \frac{dP}{dx} = 0 \,,$$

giving

$$\rho_1 u_1^2 + P_1 = \rho_2 u_2^2 + P_2 \,.$$

From the energy equation, we have

$$\rho u \frac{d}{dx}\left(\epsilon + \frac{1}{2}u^2 + \frac{P}{\rho}\right) + \left(\epsilon + \frac{1}{2}u^2 + \frac{P}{\rho}\right)\frac{d}{dx}(\rho u) = \rho u \frac{d}{dx}\left(\epsilon + \frac{1}{2}u^2 + \frac{P}{\rho}\right) \,,$$

which gives

$$\epsilon_1 + \frac{1}{2}u_1^2 + \frac{P_1}{\rho_1} = \epsilon_2 + \frac{1}{2}u_2^2 + \frac{P_2}{\rho_2} \,.$$

We are also using a γ-law equation of state, so $\epsilon = \frac{1}{\gamma-1}\frac{P}{\rho}$, so

$$\frac{1}{2}u_1^2 + \frac{\gamma}{\gamma-1}\frac{P_1}{\rho_1} = \frac{1}{2}u_2^2 + \frac{\gamma}{\gamma-1}\frac{P_2}{\rho_2}$$

if γ is the same on both sides of the shock. These equations can be rewritten in terms of the upstream Mach number $M_1 = \frac{u_1}{c_{s,1}}$,

$$\frac{\rho_2}{\rho_1} = \frac{(\gamma+1)M_1^2}{(\gamma-1)M_1^2+2} ,$$

$$\frac{P_2}{P_1} = \frac{2\gamma M_1^2 - (\gamma-1)}{\gamma+1} .$$

For radiation-dominated shocks, $P = (\gamma-1)aT^4$, where a is the radiation constant, so

$$\frac{T_2}{T_1} = \left[\frac{2\gamma M_1^2 - (\gamma-1)}{\gamma+1}\right]^{1/4} .$$

In the case of strong shocks, $M_1 \gg 1$, so the jump conditions can be approximated by

$$\rho_2 \approx \frac{\gamma+1}{\gamma-1}\rho_1 ,$$

$$P_2 \approx \frac{2\gamma}{\gamma+1}M_1^2 P_1 = \frac{2}{\gamma+1}\rho_1 u_1^2 ,$$

$$T_2 \approx T_1\left(\frac{2}{\gamma+1}\frac{\rho_1 u_1^2}{P_1}\right)^{1/4} .$$

The velocity u_1 is the shock velocity in the lab frame, so $u_1^2 \approx 2E_0/M_{\rm enc}$, where $M_{\rm enc}$ is the mass coordinate of the original star through which the shock has passed. $T_1/P_1^{1/4} = (3/a)^{1/4}$, so

$$T_2 \approx \left(\frac{2}{\gamma+1}\frac{3(M_{\rm enc}/r^3)2(E_0/M_{\rm enc})}{a}\right)^{1/4} \approx 2.1\times10^8\ {\rm K}\left(\frac{E_0}{10^{51}\ {\rm erg}}\right)^{1/4}\left(\frac{R_*}{R_\odot}\right)^{-3/4} ,$$

which is similar to the expression found in Equation 2.2.

Tests With Stellar Models

The mapping from the MESA model output onto the grid for the explosion simulation is done assuming a logarithmic grid in radius such that $dr = \alpha r$, where α is some small number such as 0.05. Then pressure, density, and mass fractions of various isotopes are interpolated linearly based on this new grid, and the mass contained

in each zone is calculated from the density and volume. For these illustrative tests, we have used a stellar model from MESA with a ZAMS mass $M_{\rm ZAMS} = 20\ {\rm M}_\odot$, and we have removed mass almost down to the edge of the helium core such that the hydrogen envelope mass is $M_{\rm env} = 0.05\ {\rm M}_\odot$, resulting in a final stellar mass of about $M_{\rm f} \approx 5.7{\rm M}_\odot$. We then exploded this model with 1.7 B of thermal energy.

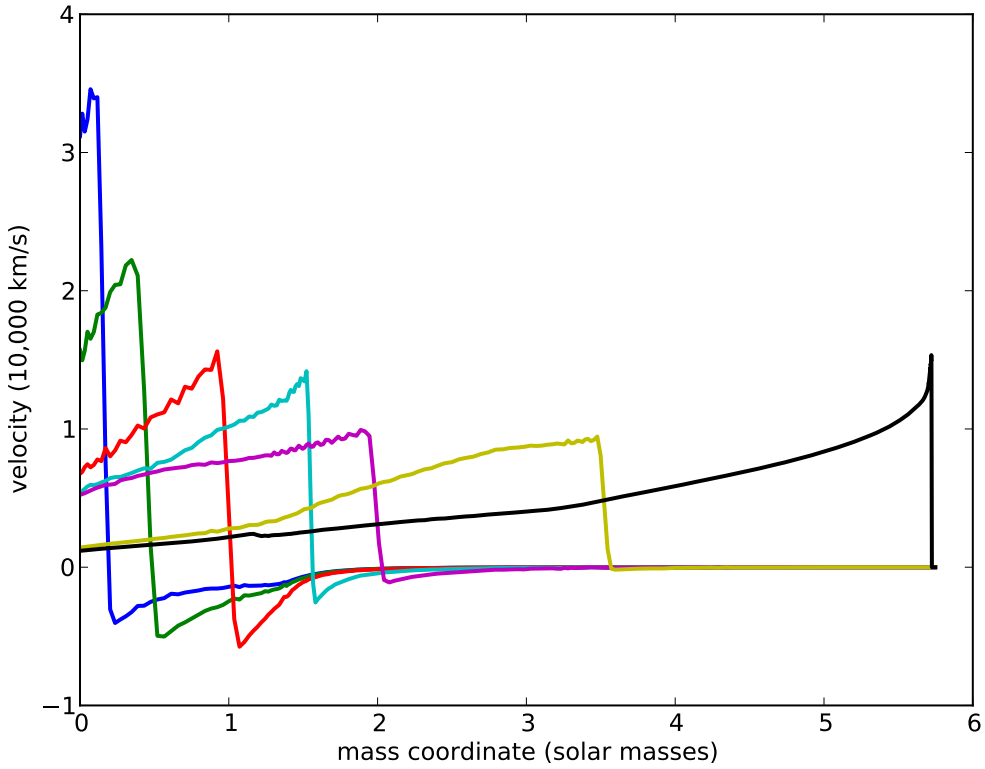

Figure 3.10: Illustrative plot showing velocity as a function of mass coordinate at various times for the star with $M_{\rm ZAMS} = 20\ {\rm M}_\odot$ and almost all of the hydrogen envelope removed ($M_{\rm env} = 0.05\ {\rm M}_\odot$), which we exploded with an energy of 1.7 B.

Figure 3.10 shows the velocity of the material as a function of mass coordinate at various times until shock breakout. The shock moves from the left-hand side of the plot outward; meanwhile, some of the material just outside the shock has an increasingly negative velocity due to gravity. If we track specific zones, we can show each being accelerated by the shock at different times, as shown in 3.11.

Figure 3.12 shows the temperature as a function of mass coordinates for select times. The post-shock material is at roughly constant temperature throughout. We

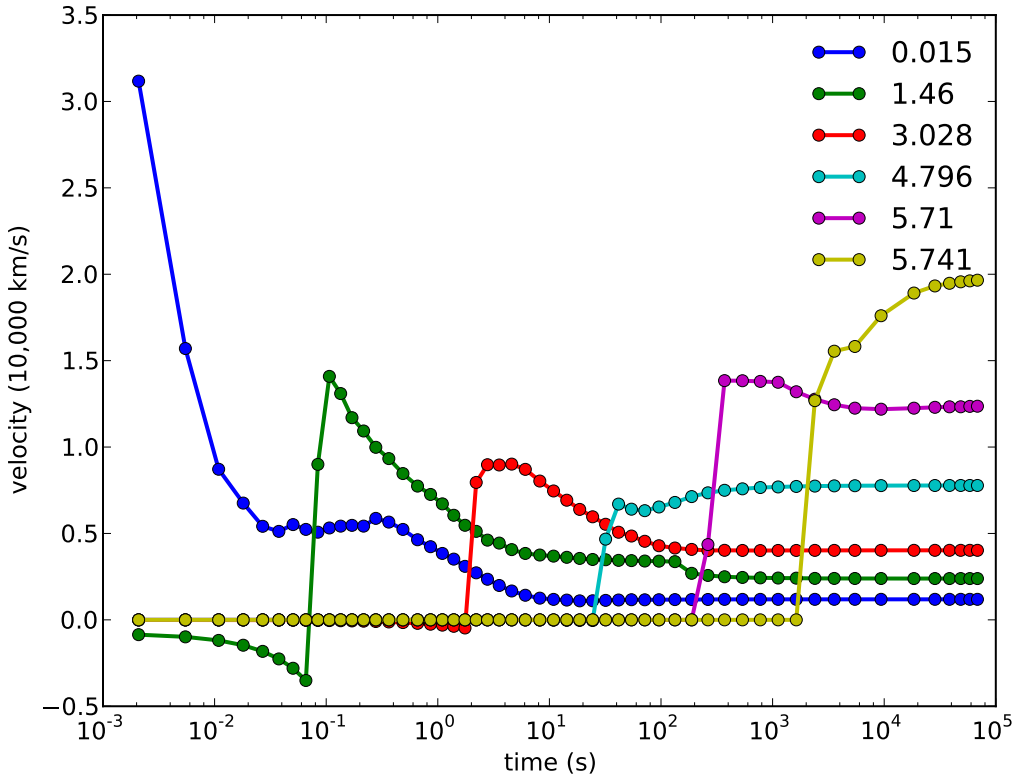

Figure 3.11: Velocity as a function of time for zones at various mass coordinates, indicated by legend labels in solar-mass units.

can track the temperature just behind the shock as it moves out, and this quantity is shown in Figure 3.13. Included in this figure is is the analytic solution given by Equation2.2, which matches closely except in the innermost regions, where our numerical solution has a higher temperature.

Radiation Transport

We model the spectra and light curves by mapping the homologously expanding ejecta into SEDONA. We run 1D calculations in local thermodynamic equilibrium and with power contributions from both radioactive ^{56}Ni and thermal energy deposited into the ejecta by the shock. During the hydrodynamics phase, we do not track nuclear reactions. Since our work focuses on CCSNe and not thermonuclear explosions, there should not be extensive nuclear processing of the ejecta; however, in some cases, some of the ejecta may be under the conditions to produce ^{56}Ni.

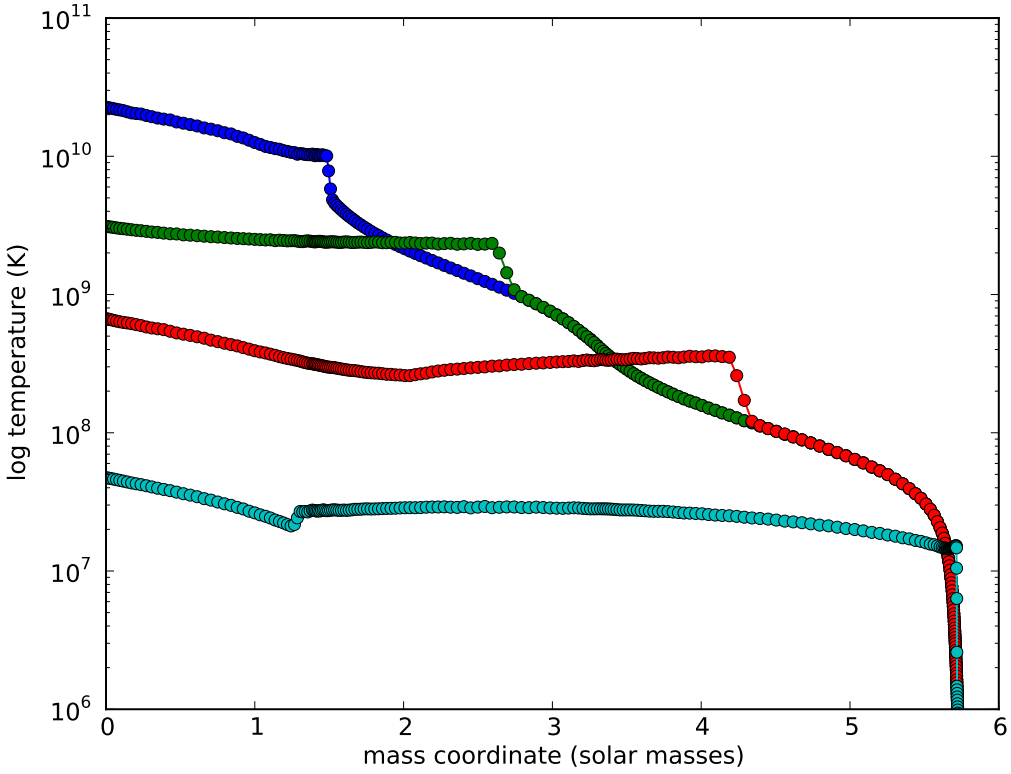

Figure 3.12: Illustrative plot showing temperature as a function of mass coordinate at various times for the same star with $M_{\rm ZAMS} = 20$ M$_\odot$ and $M_{\rm env} = 0.05$ M$_\odot$ exploded with an energy of 1.7 B. Note that the shocked material has roughly constant temperature throughout at each time step.

We choose to keep the amount and distribution of radioactive nickel as free parameters. An estimate of the (maximum) ^{56}Ni mass can be obtained by assuming that any zone that attains a temperature of $\sim 5 \times 10^9$ K will burn fully to nickel. However, it is still valuable to vary this parameter as there are likely uncertainties involved, including fallback of some of the nickel onto the remnant. We have also implemented a simple way of approximating a smeared nickel distribution due to mixing. The ^{56}Ni fraction profile is a function of the form

$$\frac{1}{2}\left(\frac{\tanh[-(r - r_{\rm sh})]}{sdr} + 1\right), \tag{3.6}$$

where dr is the width of each zone as mapped into SEDONA. This is effectively a smoothed step function such as the one shown in Figure 3.14. Here $r_{\rm sh}$ represents the

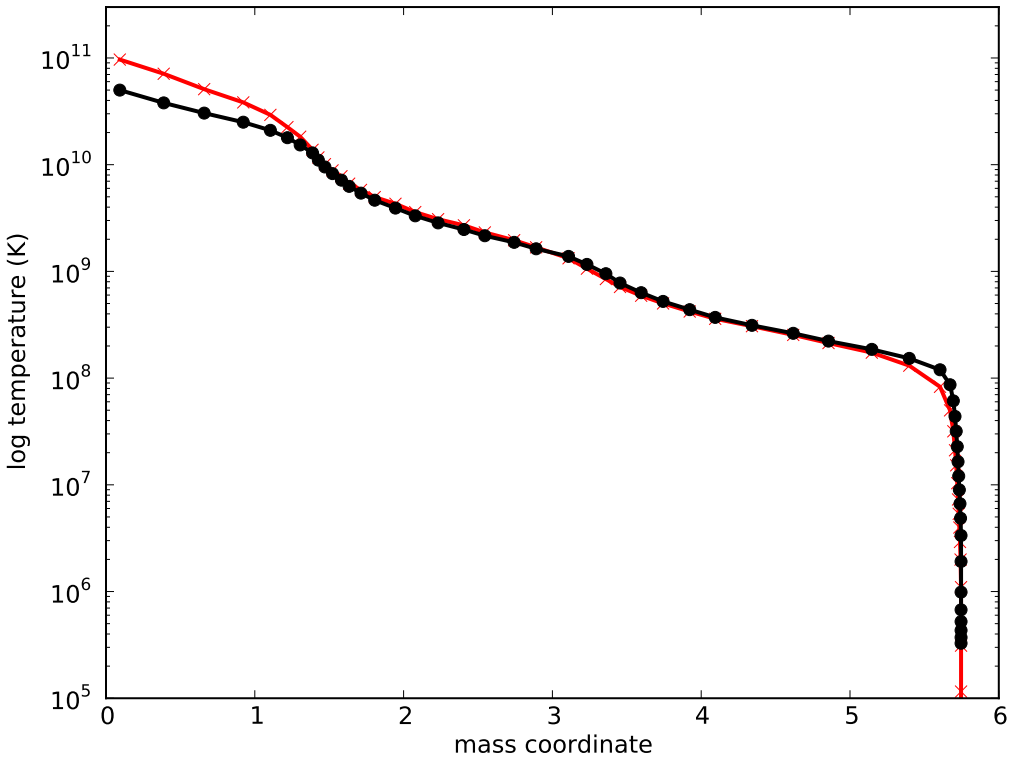

Figure 3.13: Shock temperature as a function of mass coordinate (red) compared to the temperature given by Equation 2.2 (black).

shift of the transition between nickel-rich and nickel-poor ejecta, while s controls the amount of smoothing (small s will concentrate all of the nickel in the innermost layers). The parameters for determining the nickel distribution are nickel mass and the degree of smoothing s, so the location of the transition parameterized by $r_{\rm sh}$ is solved for iteratively based on these two parameters.

Pipeline Demonstrations

For our exploratory pipeline tests, we have evolved two sets of models, starting with initial masses 20 $M_\odot$ and 40 $M_\odot$. We removed mass with constant mass loss rates of $\dot{M} = 10^{-3}$ $M_\odot$ yr^{-1} down to final masses of $M_f = 3$ $M_\odot$, 4 $M_\odot$, 5 $M_\odot$, 6 $M_\odot$, 8 $M_\odot$, and 10 $M_\odot$. For $M_i = 20$ $M_\odot$ models, we additionally ran down to $M_f = 6.5$ $M_\odot$ and 7 $M_\odot$ because this was the region in parameter space between progenitors with significant hydrogen envelopes and with no hydrogen envelopes at all. Runs are tabulated with observational properties at collapse in Table 3.1. Some stars with

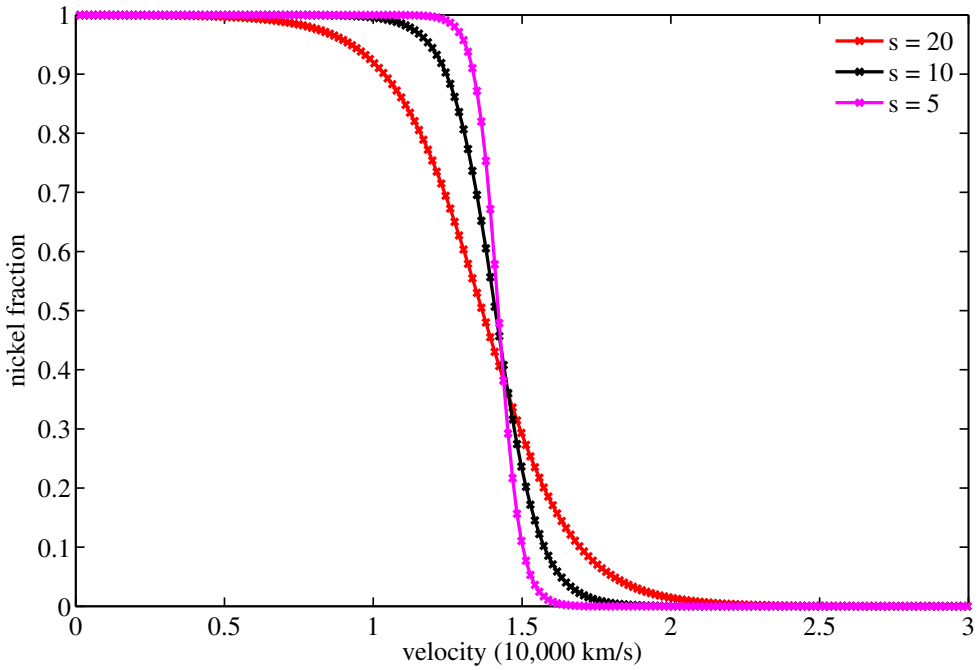

Figure 3.14: Nickel distribution for the same nickel mass but different amounts of smoothing, parameterized by the quantity s, which is related to the number of zones over which the distribution is smoothed.

lower final masses could not run to iron core collapse within a reasonable amount of time, which is typical for bare helium cores in this mass range. These types of stars will be explored more in Chapter 6.

Figures 3.15, 3.16, and 3.17 show MESA profiles and SEDONA outputs for some of our models. Fully stripped models have timescales that are long compared to typical SNe Ibc, indicating that realistic models will have to be pushed down to lower values of M_f. The light curves of $M_i = 20$ M$_\odot$ models begin to resemble SNe II at larger M_f (i.e. their hydrogen envelopes are still intact). Note also that the $M_i = 40$ M$_\odot$, $M_f = 10$ M$_\odot$ model has grown a very large oxygen core and has a very long-timescale light curve, which is not commonly observed. We also show example spectra in Figure 3.18, one a typical Type Ibc spectrum and one a typical Type II spectrum.

3.2 Discussion of Pipeline Results

In this chapter, we have shown the first uses of our pipeline for end-to-end SN simulations. First, we have stripped stars from two initial masses down to different

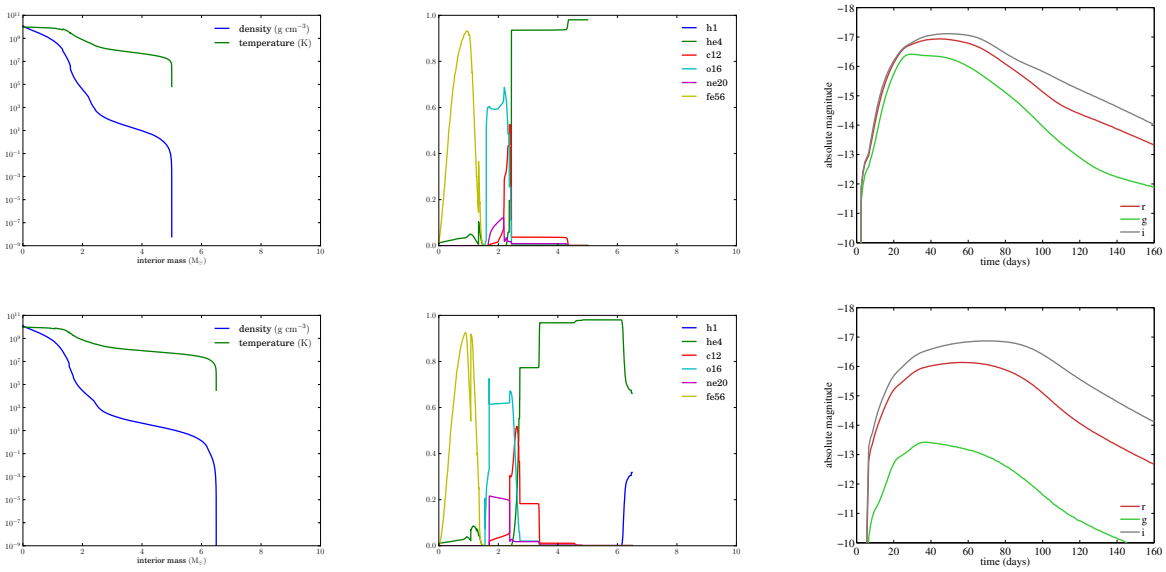

Figure 3.15: Model results for $M_i = 20$ M$_\odot$. From left to right are density and temperature structures; mass fractions of various isotopes; and SDSS light curves from explosions with 10^{51} erg, $M_{\rm Ni} = 0.1$ M$_\odot$, and the nickel distribution is centralized ($S = 10$). From top to bottom are $M_f = 5$, 6.5 M$_\odot$. These light curves are reminiscent of SNe Ibc but with longer timescales than are typical, indicating that they may have more ejecta mass than the usual hydrogen-free core-collapse supernova.

final masses and then allowed them to evolve to core collapse in most cases. All of these mass loss episodes are examples of case B mass transfer, such that the helium core has already been formed on the Main Sequence (see e.g. Yoon et al. 2010).

We have chosen to strip off an arbitrary amount of mass after expansion to the red supergiant phase, without reference constraints of more physical mechanisms. Because binary interaction is difficult to calculate and can have many parameters involved, this is an appropriate way to explore the possible space of mass stripping before moving on to more physically realistic calculations. It allows us to study how the mass stripping changes the stellar structure, and therefore supernovae, in several ways.

Most of the models we have evolved from $M_{\rm i} = 20$ M$_\odot$ have roughly the same core structure because the stripping does not cut into the helium core formed on the main sequence, which is $5 - 6$ M$_\odot$ (the model we have stripped down to $M_{\rm f} = 4$ M$_\odot$ has a different structure, which will be important for Chapter 6). In these models, the interior structure is the same, so the core size and abundances are all similar, but the

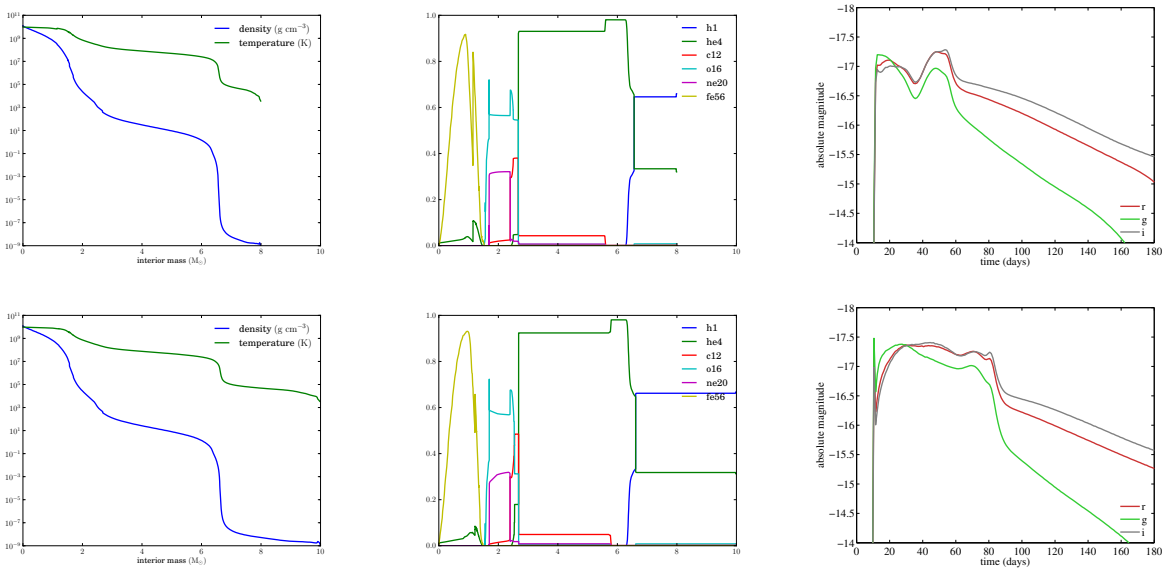

Figure 3.16: Same as Figure 3.15 but for $M_f = 8,\ 10\ \mathrm{M}_\odot$. In these runs, there is substantial hydrogen present, which significantly affects the shape of the light curves and produces IIb- and IIP-like SNe.

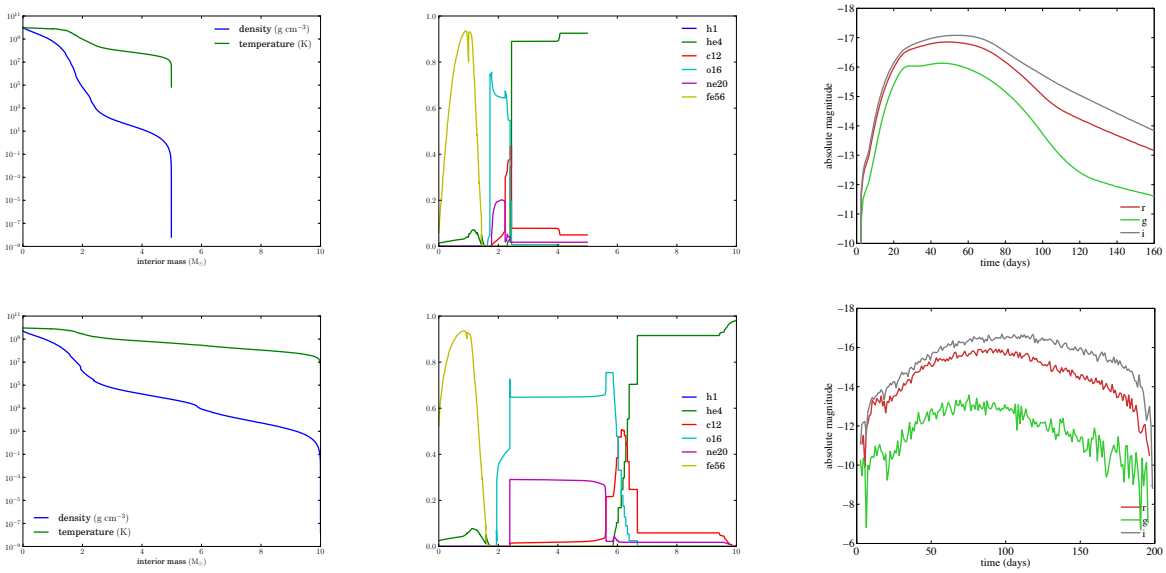

Figure 3.17: Same as Figures 3.15 and 3.16 but for $M_i = 40\,\mathrm{M}_\odot$ and $M_f = 5,\ 10\,\mathrm{M}_\odot$. These light curves are also SN Ibc-like but they timescales are very long. If SNe Ibc with these ejecta masses exist, they are very rare.

mass and radial extent of the hydrogen envelope varies, and this can dramatically change the light curve, as we have shown.

In the case of $M_\mathrm{i} = 40\,\mathrm{M}_\odot$ models, all of the hydrogen has been stripped off, and the

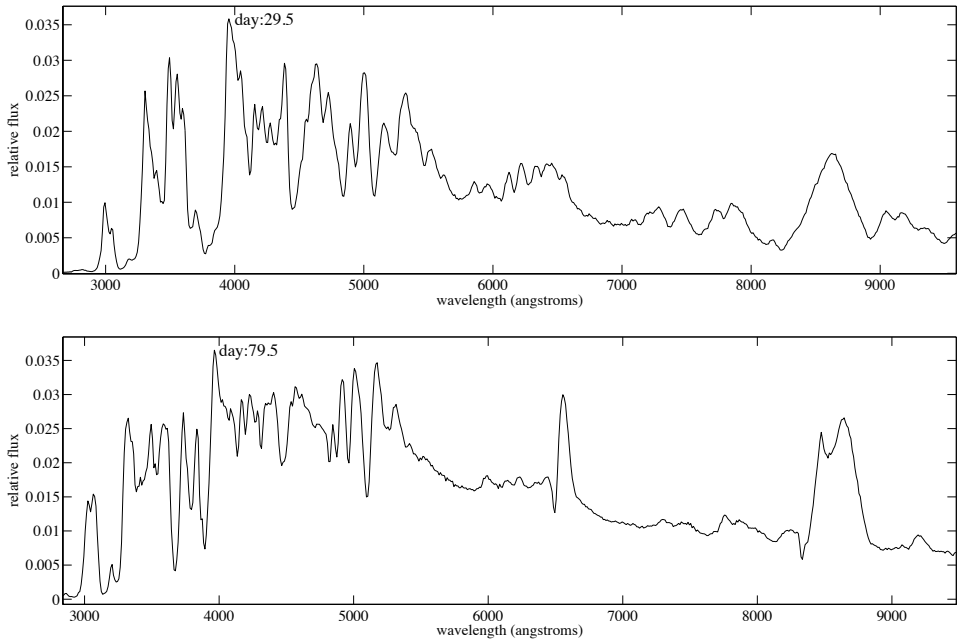

Figure 3.18: Spectra for runs with $M_{\rm i}$ = 20 $M_\odot$. The top panel shows a spectrum from the run with $M_{\rm f}$ = 5 $M_\odot$, in which the entire hydrogen envelope has been removed. This spectrum resembles that of a typical SN Ibc. In the bottom panel is the spectrum for $M_{\rm f}$ = 10 $M_\odot$, which still has a substantial hydrogen envelope at explosion and resembles a typical SN II upon exploding.

mass loss even removes part of the helium core. Clearly the core size and structure are affected significantly, as are the abundances of heavier elements. With more realistic treatment of binary evolution, this may or may not be possible, and losing part of the helium core at this stage of evolution could involve a common-envelope phase, which would be much more complicated. However, we show the results of this stripping with the acknowledgement that more detailed study will be needed to assess the feasibility of each model.

As mass loss occurs stars, stars tend to first move blueward. They become hotter but maintain a constant luminosity, since the stripping does not greatly affect the luminosity from burning, but meanwhile the radius drops. If the mass loss is severe enough, it can cut into hydrogen shell burning, which is why the more stripped models dip to lower luminosity and temperature, then climb back up to higher luminosities when later phases of core burning start. In general, stripped stars end up bluer and slightly more dim, depending on the amount of stripping. This is especially true of out $M_{\rm i}$ = 40 $M_\odot$ models, which are all bare helium cores,

so the stripping has influenced the core size and therefore the energy output from core burning. However, this evolution may or may not be realistic for a true star, depending on the parameters of the binary system that causes the mass loss.

Although the mechanism and rate of mass loss will be important for determining the star's HR track, we predict that it will not greatly affect the final stellar model, provided that it is Case B mass transfer. We have experimented with different mass loss rates, and it does not appear that there is a significant change in stellar structure among them. This suggests that, after the star leaves the Main Sequence, the specific mass loss history is not very important to determining the stellar structure; only the amount of mass removed matters. This allows us a certain amount of freedom in using our simplified mass loss prescription rather than more complex binary evolution simulations, which have more parameters and some uncertain physics.

We have shown hydrodynamics tests with one stellar model, and they behave qualitatively as expected and also are consistent with analytic calculations from Rankine-Hugoniot shock jump conditions. Upon exploding our series of stellar models with varying mass loss, we have calculated light curves and spectra for those exploded with 1 B, a typical observed SN energy. The hydrogen-rich stellar models we have exploded closely resemble SNe IIP and IIb, indicating that these different types may indeed be simply due to different amounts of loss of the H envelope. Our hydrogen-poor models look qualitatively like SNe Ibc and have Ibc-like spectra, but their timescales are quite long. This suggests that observed SNe Ibc usually have smaller ejecta masses, as expected from analytical estimates.

The question then is why SNe like these are not observed, or at least are not common. Is it rare to produce such massive hydrogen-stripped stars in the first place, or do these stars typically form black holes rather than exploding? A detailed comparison of stripped stars and their compactnesses is necessary to help resolve this issue. While we have briefly discussed the compactness of our stellar models, it would in informative to conduct a broader study of compactness of stars from binary systems, whereas most previous studies have focused only on single stars. It is possible that the compactness will be primarily influenced by the mass of the helium core; indeed, we observe the largest changes in compactness with the $M_{\rm i} = 40$ $M_\odot$ stars since all of their helium core masses are quite different. Further study could help determine whether our long-timescale SNe Ibc are unrealistic simply because such stars would not explode.

References

Clausen, D., Piro, A. L., & Ott, C. D., 2015, ApJ, 799, 190, 190

O'Connor, E., & Ott, C. D., 2011, ApJ, 730, 70, 70

Paxton, B., Marchant, P., Schwab, J., et al., 2015, ApJS, 220, 15, 15

Sukhbold, T., Woosley, S., & Heger, A., 2017, ArXiv e-prints

Yoon, S.-C., Woosley, S. E., & Langer, N., 2010, ApJ, 725, 940

Chapter 4

RAPIDLY FADING SUPERNOVAE FROM MASSIVE STAR EXPLOSIONS

ABSTRACT

Transient surveys have recently discovered a class of supernovae (SNe) with extremely rapidly declining light curves. These events are also often relatively faint, especially compared to Type Ia SNe. The common explanation for these events involves a weak explosion, producing a radioactive outflow with small ejected mass and kinetic energy ($M \sim 0.1$ M$_\odot$ and $E \sim 0.1$ B, respectively), perhaps from the detonation of a helium shell on a white dwarf. We argue, in contrast, that these events may be Type Ib/c SNe with typical masses and energies ($M \sim 3$ M$_\odot$, $E \sim 1$ B), but which ejected very little radioactive material. In our picture, the light curve is powered by the diffusion of thermal energy deposited by the explosion shock wave, and the rapid evolution is due to recombination, which reduces the opacity and results in an “oxygen-plateau" light curve. Using a radiative transfer code and simple 1D ejecta profiles, we generate synthetic spectra and light curves and demonstrate that this model can reasonably fit the observations of one event, SN 2010X . Similar models may explain the features of other rapidly evolving SNe such as SN 2002bj and SN 2005ek. SNe such as these may require stripped-envelope progenitors with rather large radii ($R \sim 20\ R_\odot$), which may originate from a mass loss episode occurring just prior to explosion.

4.1 Introduction

As more powerful wide-field optical surveys come online, not only have the rates of supernova (SN) discoveries increased, but so has our ability to detect rarer events at greater distances and with lower luminosities. Of particular interest is a small but growing collection of unusual supernovae whose light curves are relatively dim and of short duration. These rapidly fading supernovae (RFSNe) not only have peculiar light curves, but their spectra are also often distinctive, in some cases containing line features that have not yet been securely identified. Presumably these transients have something interesting to tell us about the life and death of stars, but we still do not have a complete understanding of their physical properties or origins.

The class of RFSNe is diverse and may be broken up into several subclasses. In this chapter, we focus on SN 2010X (Kasliwal et al. 2010) and similar events, which have been found in spiral galaxies and so could potentially be related to massive star death. The peak absolute magnitude of SN 2010X was -17 (corresponding to a luminosity of $\sim 10^{42}$ erg s^{-1}) and the light curve declined very rapidly after peak (by 0.23 ± 0.01 mag day^{-1}). The spectra showed line features of oxygen, calcium, and iron, with some uncertain features attributed to perhaps aluminum or helium. The light curve of a seemingly related event, SN 2002bj (Poznanski et al. 2010), was about two magnitudes brighter than SN 2010X but declined at a nearly equal rate. The spectra of SN 2002bj contained features of silicon, sulfur, and what was tentatively identified as vanadium. In both cases, the typical ejecta velocities, measured from the blueshift of the absorption lines, were around $5,000 - 10,000$ km s^{-1}. Recently Drout et al. (2013) presented detailed observations of SN 2005ek, which strongly resembles SN 2010X in many ways.

Other RFSNe likely belong to distinct sub-classes. Events like SN 2005E have been labeled "calclium-rich transients" (Perets et al. 2010; Kawabata et al. 2010; Kasliwal et al. 2012), as their late time spectra are dominated by calcium emission. These SNe have been found in the outskirts of elliptical galaxies with no signs of star formation and therefore likely originate from old stellar populations. Another class of RFSNe, the "SN 2002cx-like", or "Iax" events, show some spectroscopically similarities to SNe Ia, but are distinguished by low peak magnitudes (between about -14 and -19 in V-band) and low ejecta velocities (Foley et al. 2013).

Several physical models have been proposed to explain the RFSNe. In almost all cases, the rapid evolution of the light curves is explained as a consequence of a low ejected mass (~ 0.1 M$_\odot$), resulting in a short photon diffusion time through

the ejecta. The ".Ia" model, for example, considers the detonation of a thin shell of helium that has accreted onto the surface of a carbon/oxygen (C/O) white dwarf (Bildsten et al. 2007; Shen et al. 2010). The model is so named because the kinetic energy (~ 0.1 B, where 1 B = 10^{51} erg) as well as the ejected mass and luminosity are each about a tenth of those of a typical Type Ia supernova (SN Ia). This model can reproduce some basic properties of the SN 2010X light curves (Kasliwal et al. 2010). However, as we discuss later, the model has difficulty reproducing important features of the observed spectra and the shape of the light curve. In addition, current ".Ia" models do not reach the higher luminosities seen in events like SN 2002bj.

Partial explosions of C/O white dwarfs near the Chandrasekhar mass have also been suggested as an origin of RFSNe. Kromer et al. (2013) simulate a centrally ignited deflagration that burns a portion of the star but does not release enough nuclear energy to completely unbind it. Instead, a fraction of the mass (~ 0.4 $M_\odot$) is ejected with low kinetic energy and a ^{56}Ni content of ~ 0.1 $M_\odot$. The resulting transients are dim but have fairly long diffusion times due to the relatively high amount of ejected matter and low energy. The light curves therefore do not decline rapidly enough to match the SN 2010X-like events, although this model may explain the SN 2002cx-like transients.

Another potentially relevant model is the accretion-induced collapse (AIC) of a white dwarf to a neutron star. In the AIC simulations of Dessart et al. (2006), only a very small amount of radioactive material ($\sim 10^{-4} - 10^{-3}$ $M_\odot$) is ejected. The resulting transient should therefore be very dim. The simulations of Fryer et al. (2009), however, find larger radioactive masses (~ 0.05 $M_\odot$) and predict brighter SNe. For rapidly differentially rotating white dwarfs, a centrifugally supported disk may form during collapse and subsequently be blown apart, perhaps synthesizing even more ^{56}Ni (Metzger et al. 2009; Darbha et al. 2010; Abdikamalov et al. 2010). In these models, the ejecta velocities are fairly large, near the escape velocity of the neutron star ($\sim 0.1 - 0.3c$). If the WD is surrounded by a relatively dense circumstellar medium, the ejecta may be slowed down and the light curves powered in part by shock heating (Fryer et al. 2009; Metzger et al. 2009).

While the above white dwarf models may explain a subset of the observational class of RFSNe, we argue that they cannot explain all such events. We consider in particular the SN 2010X -like transients and highlight two observables that may point to a different origin. The first is the precipitous decline in the post-maximum light curve with no sign, at least within the limits of the observations, of a radioactively

powered light curve tail at late times. This suggests that the amount of radioisotopes ejected is quite small. The second is the presence of certain strong spectral features, in particular OI. In this chapter, we show that the OI lines in SN 2010X may require a relatively large mass of ejected oxygen, which is difficult to accommodate along with the rapid decline in brightness in a ".Ia" or similar model. A similar estimate of the oxygen mass is discussed by Drout et al. (2013) in an analysis of SN 2005ek.

Some previous studies have considered a core collapse explanation for RFSNe. Moriya et al. (2010) simulate low-energy explosions in massive stars and show that, with proper tuning, only a small amount of mass may be ejected (~ 0.1 M$_\odot$) with most of the star falling back onto a compact remnant (a black hole). The 1D models of Moriya et al. (2010) assume an artificial complete mixing, although the authors speculate that a jet-powered explosion may be able to carry ^{56}Ni to the surface layers. Drout et al. (2013) also discuss the possibility of a low-energy ($0.25 - 0.52$ B) core collapse explanation for SN 2005ek with an inferred ejecta mass of $0.3 - 0.7$ M$_\odot$, a ^{56}Ni mass of 0.03M$_\odot$, citing fallback among a few explanations for such a low-mass ejection. One question this raises is how the radioactive ^{56}Ni, which is usually produced in the dense innermost regions of the star, avoids falling back and instead is ejected with the outer layers of the star.

The common feature of all of the above models has been an unusually low ejected mass and energy. Here, in contrast, we show that the mass and energy of SN 2010X - like events may be typical of Type Ib/c SNe ($M \sim 1-5$ M$_\odot$, $E \sim 1$ B). We attribute the luminosity not to radioactivity but to the thermal energy deposited by the explosion itself. The rapid light curve decline, despite the relatively high ejected mass, can be explained by recombination, which dramatically reduces the effective opacity.

The possibility that some SNe may fail to eject radioactive isotopes has been considered before. Fryer et al. (2009) discuss models of very massive stars ($\gtrsim 20$ M$_\odot$) in which the amount of material that falls back onto the remnant may be quite substantial, i.e. several solar masses. Essentially all of the ^{56}Ni is formed in the innermost layers of the ejecta and falls back, robbing the light curves of energy from radioactive decay and producing very dim events (V and B magnitudes of -13 to -15). Ugliano et al. (2012) indicate that such a large amount of fallback material is unlikely, probably not more than ~ 0.2 M$_\odot$, but this may still be enough to accrete most if not all of the radioactive material produced. Dessart et al. (2011) have considered Type Ib models that lack ^{56}Ni and show that they produce relatively short duration, thermally powered light curves with peak luminosities ($\sim 10^{40} - 10^{41}$ ergs s^{-1}).

In this chapter, we explore such models of massive star explosions as an explanation for SN 2010X-like events. We first argue that SN 2010X ejected a substantial amount of oxygen, suggestive of the explosion of a stripped-envelope, massive star (§4.2). We then demonstrate that massive SNe can produce brief, rapidly declining light curves once recombination is taken into account (§4.3). We then use the radiative transfer code SEDONA (Kasen et al. 2006) to produce synthetic light curves and spectra of simple, 1-D ejecta models, and show that these models can reproduce the SN 2010X light curve, provided that the progenitor star had a large enough radius (§4.4). In §4.5, we discuss various progenitor scenarios that may be responsible for this class of SNe.

4.2 Estimates of the Ejecta Mass

Analytical scaling relations are commonly used to estimate the ejecta mass and kinetic energy of observed SNe. For ejecta of mass $M_{\rm ej}$ and velocity v, and assuming a constant opacity κ, the duration of the light curve $t_{\rm sn}$ is set by the effective diffusion time through the expanding ejecta (Arnett 1979):

$$t_{\rm sn} \approx 34 \left(\frac{M_{\rm ej}}{\rm M_\odot} \right)^{1/2} \kappa_{0.1}^{1/2} v_4^{-1/2} \text{ days}, \tag{4.1}$$

where $v_4 = v/10^4$ km s^{-1} and $\kappa_{0.1} = \kappa/0.1$ cm^2 g^{-1}. We have calibrated the numerical constant based on Type Ia SNe, which have $v_4 \approx 1$, $M_{\rm ej} \approx 1.4$ M$_\odot$ and a bolometric light curve width (i.e., rise plus fall) of roughly 40 days (Contardo et al. 2000). The value $\kappa = 0.1$ cm^2 g^{-1} is appropriate for electron scattering in singly ionized helium. It is also similar to the mean opacity due to Doppler broadened lines of iron-group elements, which is the dominant form of opacity in SNe Ia (Pinto & Eastman 2000).

Inverting Equation 4.1 for the ejecta mass gives

$$M_{\rm ej} \approx 0.0875 \left(\frac{t_{\rm sn}}{10 \text{ days}} \right)^2 v_4 \kappa_{0.1}^{-1} \text{ M}_\odot, \tag{4.2}$$

which has fostered the belief that RFSNe like SN 2010X represent relatively low mass ejections. Such an argument, however, presumes a constant opacity of $\kappa \sim 0.1$ cm^2 g^{-1}. In fact, the opacity of SN ejecta is highly dependent on the physical state and, as we discuss in the next section, may vary by an order of magnitude depending on the temperature and composition of the ejecta.

It is possible to derive an independent constraint on the ejecta mass using absorption features observed in the spectrum. In particular, SN 2010X showed a strong, broad,

and persistent OI triplet feature ($\lambda\lambda\lambda$7772,7774,7775), which would seem to suggest a significant mass of oxygen. In homologously expanding atmospheres, the degree of absorption is quantified by the Sobolev optical depth,

$$\tau_{\rm sob} = \left(\frac{\pi e^2}{m_e c^2}\right) t_{\rm exp} \lambda_0 n_l, \tag{4.3}$$

where λ_0 is the rest wavelength of the line, $t_{\rm exp}$ the time since explosion, and n_l the number density in the lower level of the atomic transition.

In Figure 4.1 we plot contours of $\tau_{\rm sob}$ for the OI triplet line as a function of density and temperature for ejecta composed of pure oxygen at $t_{\rm exp} = 30$ days, a time when the oxygen absorption feature is quite prominent in SN 2010X. To estimate n_l we have assumed that the ionization/excitation states were approximately given by local thermodynamic equilibrium (LTE). Figure 4.1 shows that a density of at least $\rho_{\rm c} \approx 10^{-14}$ g cm^{-3} is required to achieve strong ($\tau_{\rm sob} \gtrsim 1$) absorption in the OI line. This critical density corresponds to the most favorable temperature, $T \approx 5500$ K, at which the level density n_l is highest. For hotter temperatures, oxygen becomes more highly ionized, while for cooler temperatures it is difficult to thermally populate the excited lower level of the OI transition. In these cases, an even higher density is required to make the line optically thick.

We can use this critical OI density to obtain an approximate lower limit on the total ejecta mass of SN 2010X. The February 23 spectrum (close to $t_{\rm exp} \approx 20$ days) showed apparent OI absorption at velocities $\approx 10,000$ km s^{-1}. Assuming that the ejecta density profile is described by a broken power-law (see §4.4) and that the energy release per unit mass is typical of SNe, $E/M \sim 10^{51}$ ergs/M$_\odot$, the condition $\rho \gtrsim \rho_c$ at $v \approx 10,000$ km s^{-1} implies a total ejecta mass $M_{\rm ej} \gtrsim 0.35$ M$_\odot$. This is likely a significant underestimate, as we have assumed the oxygen layer was composed of 100% oxygen at the ideal temperature of $T \approx 5500$ K. The March 7 spectrum of SN 2010X (near $t_{\rm exp} \approx 30$ days) also shows strong absorption at the same location, which implies $M_{\rm ej} \gtrsim 1.2$ M$_\odot$.

These spectroscopic mass estimates are subject to two important caveats. First, the absorption near 7500 Å may be due in part to MgII (and perhaps FeII) rather than OI lines. Second, the line optical depths may be influenced by non-LTE effects. The lower level of the OI feature is a metastable state (albeit with a high excitation energy, $\Delta E = 9.14$ eV) such that an LTE description may not be a bad approximation. Nonetheless, it is quite possible that the level population is enhanced by non-thermal excitation by radioactive decay products (Lucy 1991; Dessart et al.

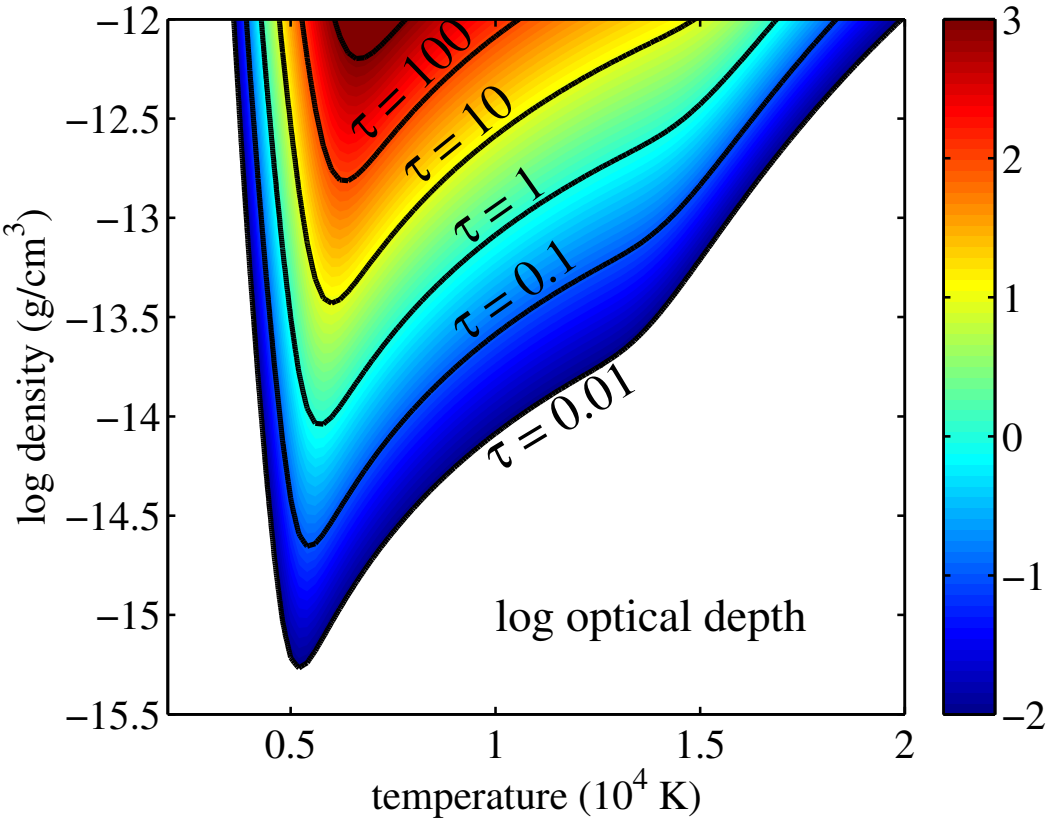

Figure 4.1: Logarithmic Sobolev optical depth of the combined OI $\lambda\lambda\lambda$7772,7774,7775 triplet line as a function of density and temperature for a 100% oxygen composition at $t_{\rm exp}$= 30 days. Black lines indicate curves of constant optical depth. The lowest point in the $\tau = 1$ curve occurs at $\rho_c \approx 10^{-14}$ g/cm^3, which is taken to give the lowest possible density needed to see the OI absorption.

2012), or by time-dependent effects (Dessart & Hillier 2008). As an empirical check of the method, one can examine the constraints for normal SNe Ia. For SN 1994D, for example, the OI feature remained mildly optically thick ($\tau_{\rm sob} \sim 1$) until about 12 days past maximum light ($t_{\rm exp} \approx 30$ days). From this, one calculates a total ejecta mass of $\sim 1-2$ M$_\odot$, which is consistent with the values expected for SNe Ia. The OI feature of SN 2010X at a comparable epoch ($t_{\rm exp} \approx 30$ days) is significantly broader and deeper than that of SN 1994D. We therefore consider it likely that the ejected mass of SN 2010X was comparable to or larger than that of a typical SNe Ia, hence $M_{\rm ej} \gtrsim 1$ M$_\odot$.

The association of SN 2010X with a massive progenitor is strengthened by comparison with core-collapse SNe. Figure 4.2 shows the SN 2010X spectra with those of

SN 1994I, which is considered a fairly typical, if somewhat fast-evolving, Type Ic SN. The agreement is striking and strongly points to a similar physical origin for the two. Drout et al. (2013) have also noted the spectroscopic resemblance of SN 2005ek to other normal SNe Ic as well as SN 2010X . The light curve of SN 1994I showed a clear radioactive tail, indicating that it ejected ~ 0.07 $M_\odot$ of ^{56}Ni (Young et al. 1995; Iwamoto et al. 1994). We will suggest that SN 2010X was a compositionally similar Type Ib/c SN but did not eject as much ^{56}Ni.

4.3 Oxygen Plateau Supernovae

The mass estimates discussed in the last section present a paradox—the narrow light curve of SN 2010X suggests a low $M_{\rm ej}$, while the spectroscopic constraints indicate that $M_{\rm ej}$ may be many times larger. Here we show that the conflicting estimates can be reconciled in a core-collapse model in which the ejecta mass is large ($M \gtrsim 1$ $M_\odot$) but where the effective diffusion time is significantly reduced due to recombination.

The opacity of SN ejecta is highly dependent on the ionization state and so may vary significantly with temperature. In Figure 4.3, we plot the Rosseland mean opacity (calculated assuming LTE) of SN ejecta of different compositions. We consider in particular an oxygen-neon-magnesium composition (see Table 4.1) which may be characteristic of the massive, stripped envelope stars believed to be the progenitors of Type Ic SNe. For higher temperatures ($T \gtrsim 6000$ K), the O-Ne-Mg opacity has a characteristic value $\kappa \approx 0.04$ cm^2 g^{-1} When the temperature drops below 6000 K, however, oxygen recombines to neutral, and the opacity drops sharply by more than an order of magnitude. This is because, in the absence of scattering off of free-electrons, photons can escape through the "windows" in wavelength space that occur between the lines, reducing the Rosseland mean opacity. However, the opacity does not drop to zero at $T \lesssim 6000$ K because other elements (such as Mg and Si) with lower ionization potentials remain ionized. For a helium-rich composition, recombination occurs at a higher temperature ($\sim 10,000$ K) due to the higher ionization potential of helium. In contrast, the opacity of ^{56}Ni and its daughter nuclei (^{56}Co and ^{56}Fe), due to the lower ionization potential of the iron group species, maintains a large value as long as $T \gtrsim 3000$ K.

The recombination physics will strongly influence the light curves of SNe composed largely of oxygen. The radiative transfer parallels the well understood effects in Type II plateau SNe (e.g., Grassberg et al. 1971; Dessart & Hillier 2008). Initially, the ejecta are heated and ionized by the passage of the explosion shockwave.

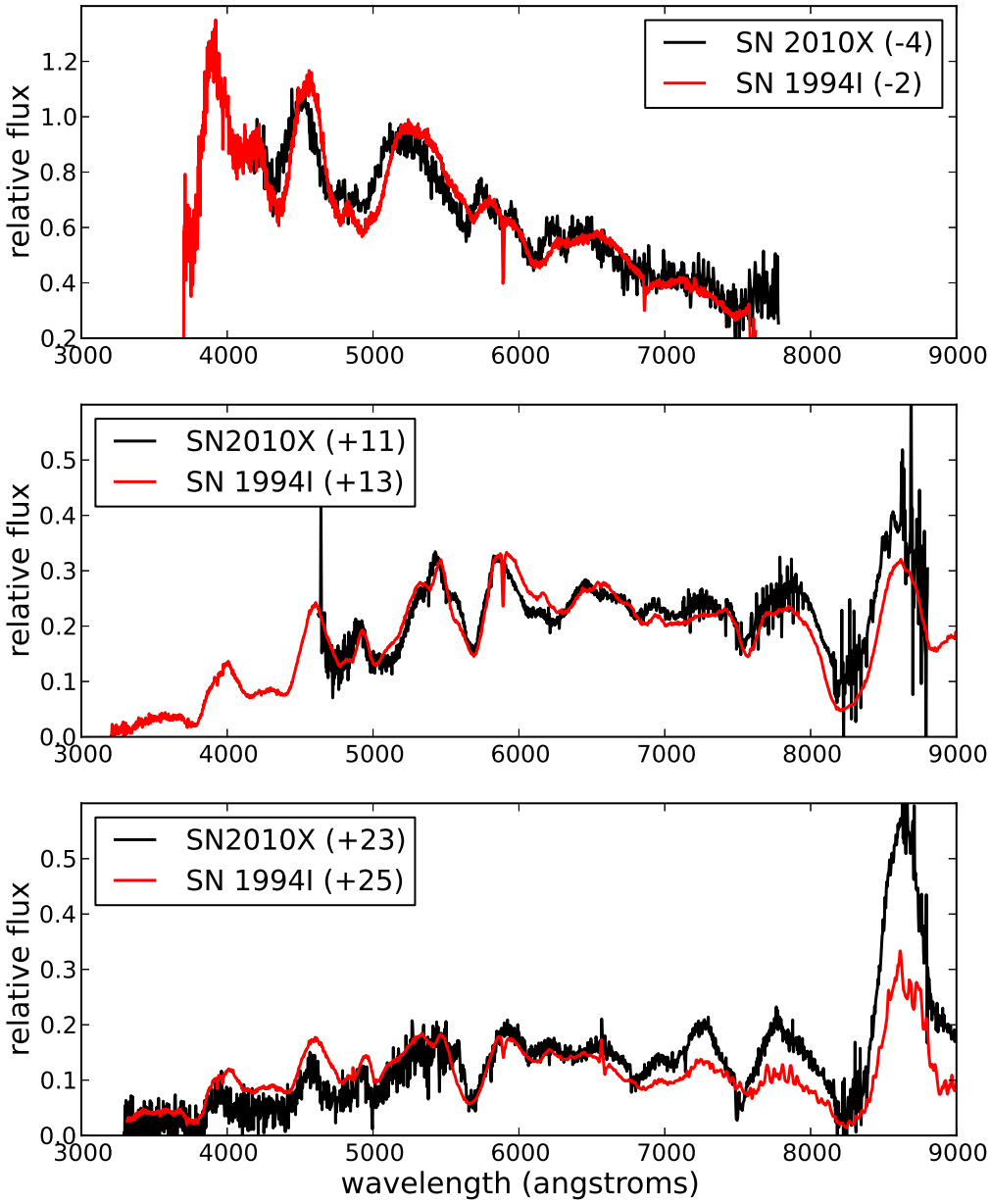

Figure 4.2: Comparison of the multi-epoch spectra of the Type Ic SN 1994I to those of SN 2010X. Times since B-band maximum are listed. The strong spectral similarity may indicate a similar physical origin.

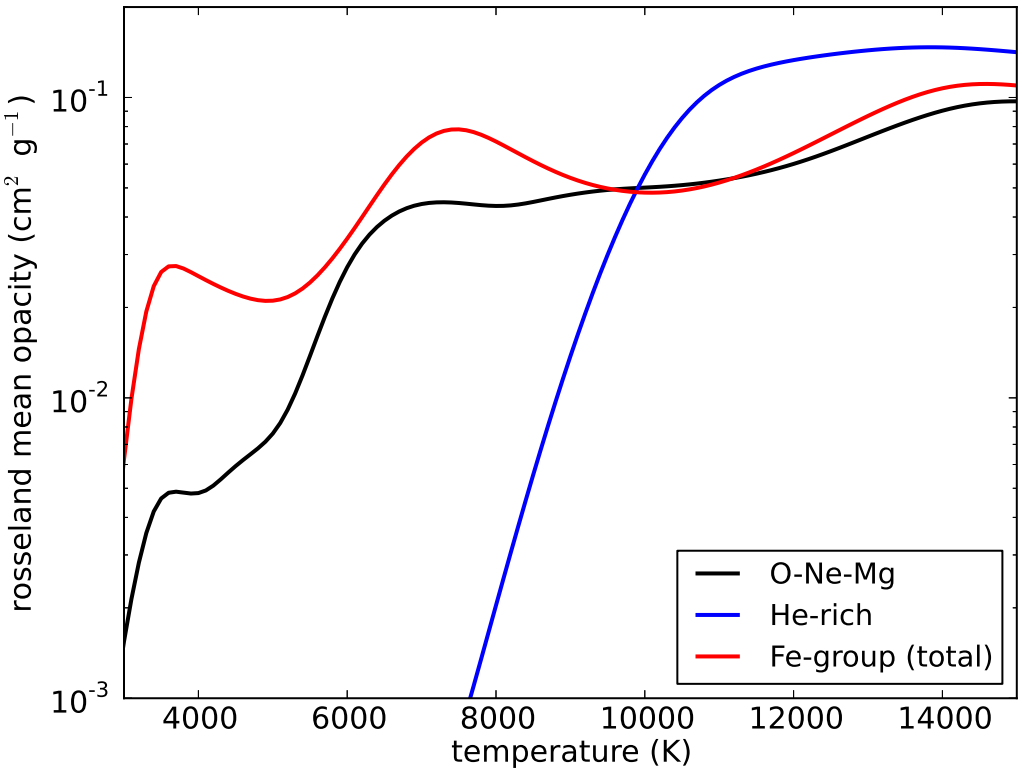

Figure 4.3: Calculated Rosseland mean opacity (for SN ejecta of different compositions) as a function of temperature for supernova ejecta at a density $\rho = 10^{-13}$ g cm^{-3} and $t_{\rm exp} = 10$ days. The main opacities included are electron scattering and line expansion opacity.

.

As the ejecta expand and cool, however, the material eventually drops below the recombination temperature $T_{\rm i}$ and becomes largely transparent. Because the outer layers of ejecta are the coolest, they recombine first, and a sharp ionization front develops in the ejecta. As time goes on, the ionization front recedes inward in mass coordinates, releasing the stored thermal energy. When this recombination wave reaches the center of the ejecta, the stored energy is exhausted and the light curve should drop off very rapidly, marking the end of the “oxygen-plateau" phase. The analogous case of a helium plateau in Type Ib SN has been discussed by Ensman & Woosley (1988) and Dessart et al. (2011).

Relationships for the timescale and peak luminosity of Type II plateau supernovae, including the effects of recombination, have been determined by Popov (1993) and

verified numerically by Kasen & Woosley (2009), who find

$$t_{\rm sn} \approx 120 E_{51}^{-1/6} M_{10}^{1/2} R_{500}^{1/6} \kappa_{0.4}^{1/6} T_{6000}^{-2/3} \text{ days} , \tag{4.4}$$

$$L_{\rm sn} \approx 1.2 \times 10^{42} E_{51}^{5/6} M_{10}^{-1/2} R_{500}^{2/3} \kappa_{0.4}^{-1/3} T_{6000}^{4/3} \text{ ergs/s} , \tag{4.5}$$

where $E_{51} = E/10^{51}$ ergs is the explosion energy, $M_{10} = M/(10\text{M}_\odot)$ is the ejected mass, $R_{500} = R/(500\ R_\odot)$ is the presupernova radius, $\kappa_{0.4} = \kappa/(0.4\ \text{cm}^2\text{g}^{-1})$ is the opacity of the ejecta, and $T_{6000} = T/(6000\ \text{K})$ is the ejecta temperature. The numerical calculations of Kasen & Woosley (2009) actually found a scaling closer to $t_{\rm sn} \propto E^{-1/4}$ rather than $E^{-1/6}$, but otherwise the relations are the same. We can use similar arguments for hydrogen-less supernovae, assuming the luminosity is determined by the recombination temperature of whatever species dominates the ejecta.

Inverting Equations 4.4 and 4.5 allows us to solve for the ejecta mass and presupernova radius in terms of observed quantities,

$$M_{\rm ej} \approx 2.9\ L_{42}^{-1} t_{20}^4 v_4^3 \kappa_{0.04}^{-1} T_{6000}^4\ \text{M}_\odot , \tag{4.6}$$

$$R_0 \approx 12.4\ L_{42}^2 t_{20}^{-2} v_4^{-4} \kappa_{0.04} T_{6000}^{-4}\ \text{R}_\odot . \tag{4.7}$$

These are very rough estimates, but they demonstrate that, when recombination is accounted for, the light curves of SN 2010X and other RFSNe are consistent with massive ($M_{\rm ej} \gtrsim 1\ \text{M}_\odot$) ejections which powered by shock energy, not radioactivity, provided that the radius of the progenitor star is sufficiently large.

4.4 Radiative Transfer Models

To model the light curves and spectra of RFSNe in more detail, we use the time-dependent Monte Carlo code radiative transfer code SEDONA (Kasen et al. 2006). We base our calculations on simple parameterized ejecta models rather than on detailed hydrodynamical simulations, as this allows us to easily control the ejecta mass, kinetic energy, and progenitor star radius. We vary these parameters, in an empirical spirit, in an effort to fit the observations of SN 2010X and constrain its physical properties.

Ejecta Models

For simplicity, we consider ejecta models that are spherically symmetric and in the homologous expansion phase. Simulations of core-collapse explosions suggest that

the ejecta density structure can roughly be described by broken power-law profile (Chevalier 1992),

$$\begin{aligned} \rho_{\rm in}(r,t) &= \zeta_\rho \frac{M}{v_{\rm t}^3 t^3} \frac{r}{v_{\rm t} t}^{-\delta} \text{ for } v < v_t \ , \\ \rho_{\rm out}(r,t) &= \zeta_\rho \frac{M}{v_{\rm t}^3 t^3} \frac{r}{v_{\rm t} t}^{-n} \text{ for } v \geq v_t \ , \end{aligned} \tag{4.8}$$

where $v_{\rm t}$ is the velocity at the transition between the two regions,

$$v_{\rm t} = 4.5 \times 10^8 \zeta_v (E_{51}/{\rm M}_\odot)^{1/2} {\rm cm\ s}^{-1} \ . \tag{4.9}$$

The coefficients ζ_ρ and ζ_v are constants which can be determined by requiring Equation 4.8 integrate to the specified mass and energy. In our model for SN 2010X , we use $\delta = 1$ and $n = 8$ as they are typical values for core collapse SN and produced reasonable fits to the light curves and spectra. These are parameters that, along with $M_{\rm ej}$, E_{51}, and R_0, are used to adjust the output light curves and spectra.

Immediately following the passage of a core-collapse SN shockwave, the explosion energy is roughly equally split between the kinetic energy and thermal energy of the stellar material. The latter is strongly radiation-dominated. Simulations suggest that, before radiative diffusion sets in, the ratio of the radiation energy density to the mass density is nearly constant throughout most of the envelope (Woosley 1988). We therefore take the energy density profile at t_0, the start time of our calculation, to be

$$\epsilon(v, t_0) = \frac{E_0}{2} \frac{\rho(v)}{M} \left(\frac{R_0}{R_{\rm ej}} \right) , \tag{4.10}$$

where $R_{\rm ej} = v_t t_0$ is the size of the remnant at the start of our transport calculation. This expression assures that the total thermal energy equals $E_0/2$ when $R_{\rm ej} = R_0$; the term in parentheses accounts for losses due to adiabatic expansion prior to the start of our transport calculation. In this model, the initial energy density profile is a broken power law with the same exponents as the mass density. This is reasonably consistent with analytical results that find that the energy density power law in the outer layers is very similar to, though slightly steeper than, the mass density profile (Chevalier 1992).

We assume that the composition of the ejecta is homogenous in two layers. Detailed abundances are given in Table 4.1. Abundances for the inner layers ($v \leq$ 10000 km s^{-1}) are typical of an O-Ne-Mg layers of a massive star and taken from the stellar evolution models of Woosley et al. (2002) for a 25 M$_\odot$ pre-supernova star

at a mass coordinate of 3.9 $M_\odot$. For the outer layers ($v > 10000$ km s^{-1}) we assume He-rich material with a solar abundances of metals. The inclusion of helium in the outer layers in fact does not significantly affect the light curves and spectra, as the photosphere at the epochs of interest turns out to be in the O-Ne-Mg layers. For the models in this chapter, we assume that no radioactive isotopes were ejected, so the light curves are solely powered by the energy deposited in the explosion shock wave.

Synthetic Light Curves and Spectra

We performed radiative transfer calculations for a series of models, in which we vary the three key ejecta parameters: the explosion E, the ejected mass $M_{\rm ej}$, and the presupernova radius R_0. Figure 4.5 shows how the SDSS r-band light curve changes as we vary each parameter while holding the others fixed. We show the r-band curves for easy comparison to SN 2010X, as this is the band in which we have the most data. The general trends are qualitatively consistent with the scaling relations (Equations 4.4 and 4.5). Increasing the explosion energy shortens the light curve duration while increasing the peak luminosity. Raising the mass increases the light curve duration but does not strongly affect its peak luminosity. Finally, a larger presupernova radius increases both the luminosity and duration of the light curve. The light curves resemble those presented in Dessart et al. (2011) for models of Type Ib/c SNe assumed to eject no ^{56}Ni (particularly models Bmi25mf6p49z1 and Bmi25mf7p3z0p2).

In Figure 4.4 we show a fit to the light curve of SN 2010X, using a model with $M_{\rm ej} = 3.5\ M_\odot, E = 1$ B, and $R_0 = 2 \times 10^{12}$ cm. The model demonstrates that the basic properties of this RFSNe can be explained by the explosion of an ordinary-mass star in which the emission is powered solely by the energy deposited in the explosion shockwave, without any radioactive ^{56}Ni. The assumed radius of the progenitor, however, is significantly larger than that of typical Wolf-Rayet stars, an issue we return to in §4.5. The short duration of the model light curve reflects the rapid release of radiation energy by the receding recombination wave. The luminosity for the first 25 days (the “oxygen-plateau") is fairly constant, but then drops dramatically as the recombination wave nears the center of the ejecta and the stored radiation energy is exhausted. After day 25, the r-band magnitude drops by more than 3 magnitudes in only 5 days, marking the end of the plateau phase. As no radioisotopes were included, the light curve shows no radioactive tail at late times, and the luminosity continues to drop rapidly.

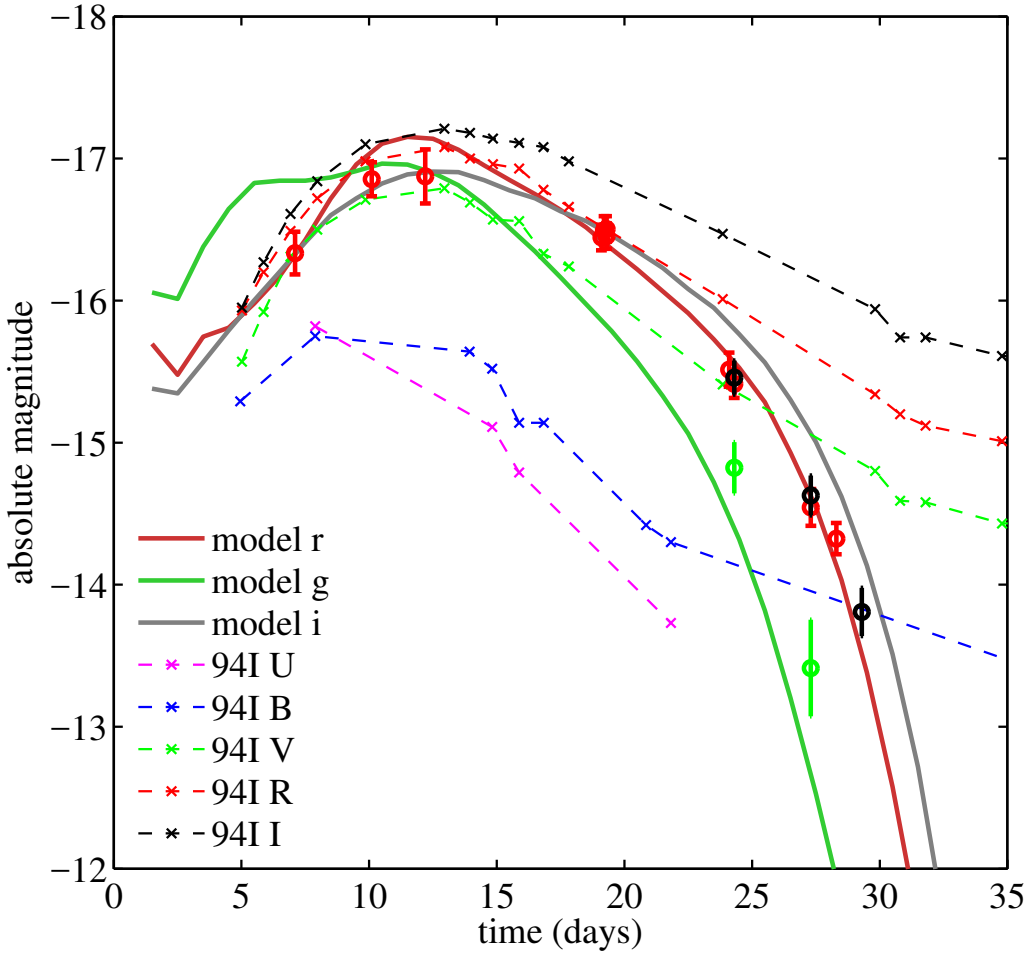

Figure 4.4: Light curves in g, r, and i calculated for a pure explosion model of SN 2010X , plotted against the data. This model was obtained with $M_{\rm ej} = 3.5$ M$_\odot$, $E_{51} = 1$ B, and $R_0 = 2 \times 10^{12}$ cm. Dashed lines show light curves in $UBVRI$ for SN 1994I, a typical SN Ic, for comparison.

The light curve fit does not uniquely constrain all three model parameters (M, E, and R_0) as there are essentially only two photometric observables (light curve brightness and duration). We have chosen to show here a model in which the mass and energy are typical of ordinary Type Ic SNe, but other combinations can provide fits of similar quality (see Figure 4.5). The degeneracy can perhaps be broken by using the observed velocity to constrain the mass energy ratio; however, the photospheric velocity in plateau SNe is set by the location of the recombination front and hence is not necessarily indicative of $v \approx (2E/M)^{1/2}$.

Figure 4.6 compares the synthetic spectrum (at $t_{\rm exp}$ = 24 days) of the same model to the February 23 spectrum of SN 2010X. On the whole, the model does a good job reproducing the major spectral features and in particular predicts significant absorption near the OI triplet. This supports the idea that the composition of the SN 2010X ejecta is consistent with that of a O-Ne-Mg core of a massive star. In detail, however, one notices discrepancies in the position and depth of several features. For instance, the model absorption near 5600 Å, due to the sodium NaID line, is much too weak and has too low a velocity. A similar problem with the NaID line has often been noted in models of Type IIP SNe, and has been explained as resulting from the neglect of time-dependent non-LTE effects (Dessart & Hillier 2008). Thus, while fine-tuning of our ejecta parameters could likely improve the spectral fit, the overall agreement is presumably limited by the simplified nature of the calculations, including the one-dimensional broken power law density structure, the two-zone uniform composition, and the neglect of non-LTE effects.

The identification of the absorption features at 6800 Å and 7000 Å was the subject of some discussion in Kasliwal et al. (2010), who suggest that these features may be due either to lines of AlII or HeI. Our model does not include aluminum, and the helium lines are optically thin, given the lack of non-thermal excitation from radioactivity. Analysis of the Sobolev optical depths suggest that lines of FeII and neutral species (SiI λ7035 and CaI) contribute to the spectral features in this wavelength region. Drout et al. (2013) similarly show that the spectra of SN 2010X-like events can be reasonably fit without invoking aluminum or helium absorption lines.

In Figure 4.7, we show the spectral time series of SN 2010X alongside select spectra from our model. The general trends are reasonable, but the color evolution is faster in the model. For example, the day 10 model spectrum is bluer than the day 9 observed spectrum, while the day 31 model spectrum is redder than the observed day 36 spectrum. Our radiative transport becomes suspect at later times ($\gtrsim$ 30 days)

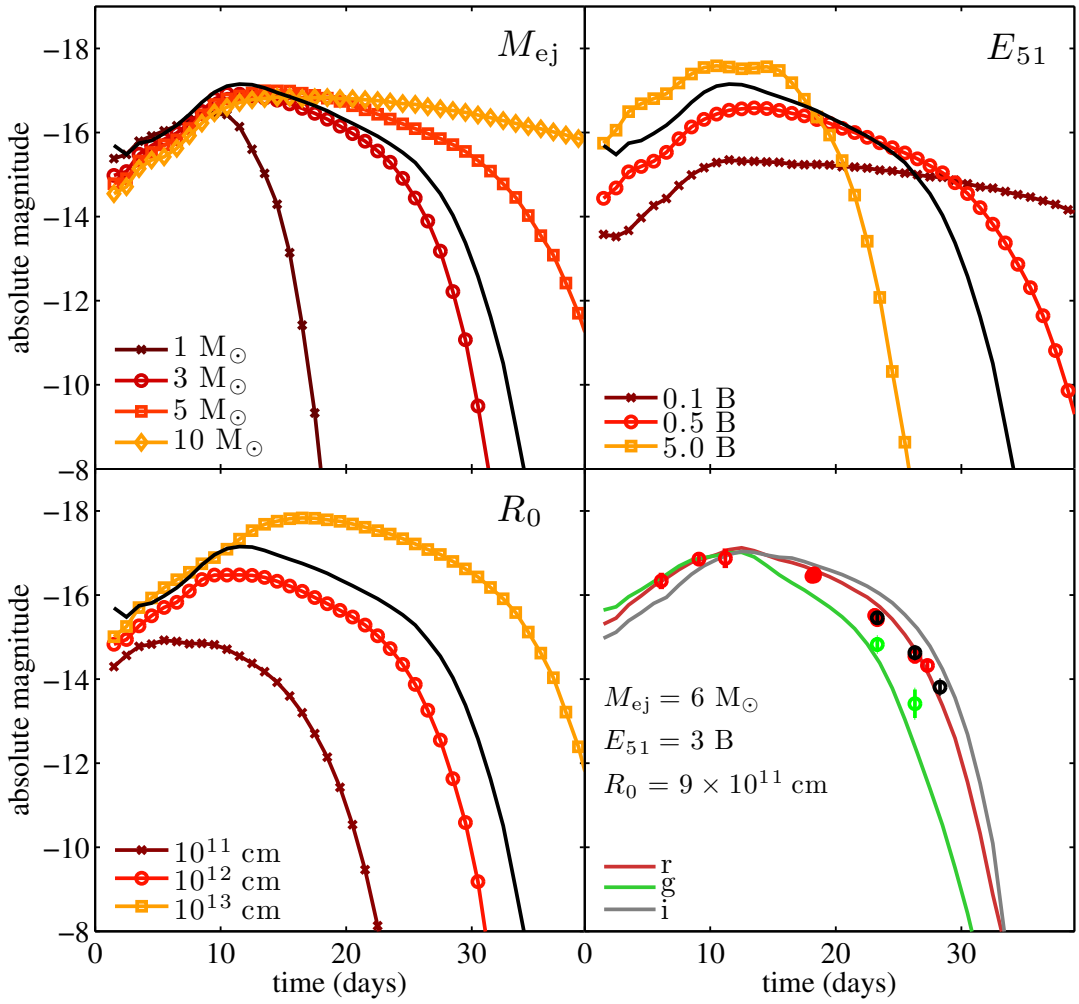

Figure 4.5: Calculated light curves using parameter variations around our fiducial ejecta model for SN 2010X, which has parameters $M_{\rm ej} = 3.5$ M$_\odot$, $E_{51} = 1$ B, and $R_0 = 2 \times 10^{12}$ cm. Top left: light curve calculations holding all parameters constant except ejecta mass. Top right: same as the top left panel but with varying explosion energy. Bottom left: same as top right and top left panels but with varying presupernova radius. Bottom right: an alternative model that fits the data fairly well with parameters $M_{\rm ej} = 6$ M$_\odot$, $E_{51} = 3$ B, and $R_0 = 9 \times 10^{11}$ cm. This demonstrates the degeneracy in our approach and that the light curves could be fit with a range of parameters.

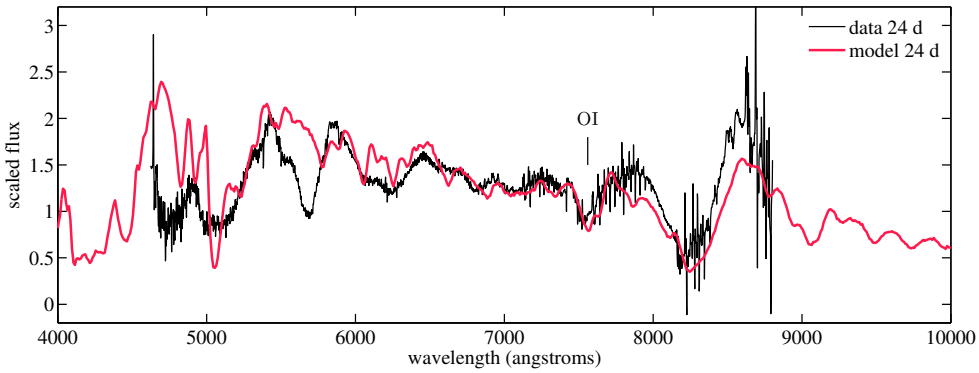

Figure 4.6: Selected spectrum calculated from our fiducial ejecta model of Figure 4.4 shown against observed data. The overall shape is similar, and most of the important spectral features are reproduced. Discrepancies may arise from our assumption of LTE, simplified power-law density structure, or the untuned abundances assumed.

as the ejecta are becoming optically thin and non-LTE effects should become more significant. While the model spectral series does not reproduce every observed spectral feature, we emphasize that we have chosen to limit any fine-tuning of the abundances and explosion parameters in order to fit the data. Further adjustment of the oxygen-rich composition would presumably lead to an improved fit, as has been shown in the modeling of the spectroscopically similar SN 1994I (Sauer et al. 2006).

4.5 Discussion and Conclusions

We have argued that some RFSNe, in particular the SN 2010X-like events, are the result of core-collapse explosion of massive stripped-envelope stars. This contradicts previous suggestions that these events represent low mass, low-energy outbursts from, for example, “.Ia" explosions on white dwarfs. In our picture, the supernova ejected very little radioactive material and the light curve was instead powered by the diffusion of thermal energy deposited by the explosion shock wave. The short duration of the light curve, despite the relatively high ejected mass ($M \sim 3-4\ \mathrm{M}_{\odot}$), is due to recombination, which dramatically reduces the effective opacity. The evolution is similar to Type IIP supernovae, and the sharp decline of the light curve can be understood as reflecting the end of an “oxygen plateau". Our 1D radiation transport models demonstrate that the observations of SN 2010X are consistent with this scenario. Empirically, the spectral similarity of SN 2010X with the Type Ic SN 1994I strongly suggests that these events have oxygen-dominated ejecta as would

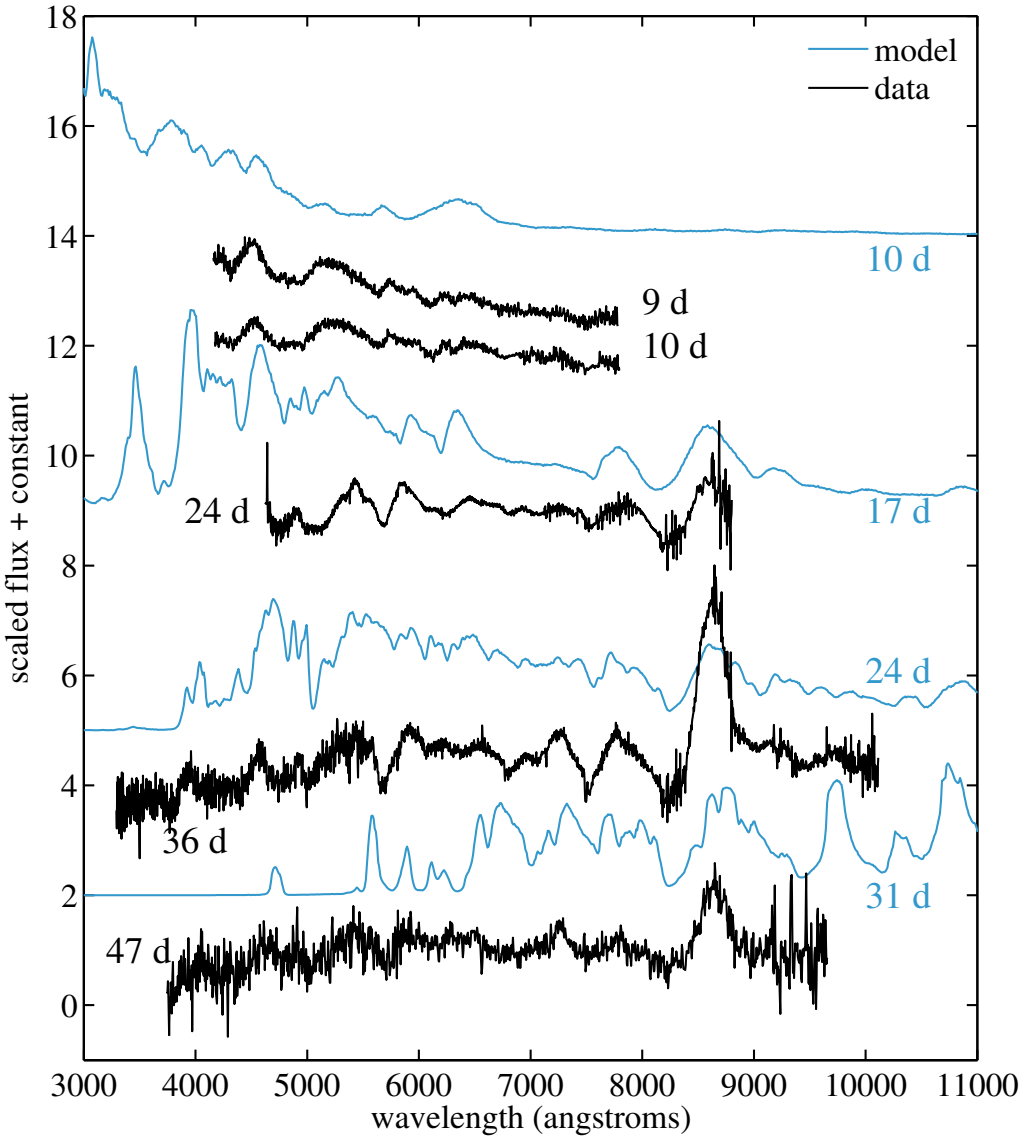

Figure 4.7: Time series of selected synthetic spectra of our fiducial ejecta model of Figure 4.4 compared the observed data of SN 2010X showing the evolution of the oxygen line and other prominent features. The order of the observed and synthetic spectra is chosen to highlight spectral similarities, some of which are more easily seen by comparison of spectra at slightly different phases.

be expected in stripped core-collapse SNe. Similar rapdily declining plateau light curves could happen in carbon/oxygen rich or helium rich ejecta.

Other RFSNe may have a similar origin. The light curve of SN 2002bj had a very similar decline rate to that of SN 2010X, but the peak luminosity was about two magnitudes brighter. The model scalings suggest that the brightness and duration could be reproduced in a Type Ib/c plateau SN with larger progenitor radius and/or higher explosion energy. The spectral features of SN 2002bj were distinct from SN 2010X , perhaps because the ejecta temperatures were higher, but possibly because the composition of the ejecta was different (e.g., helium-rich instead of oxygen-rich). Further modeling is needed to constrain the ejecta properties in detail.

Recently, Drout et al. (2013) presented a detailed analysis of SN 2005ek, which was spectroscopically and photometrically similar to SN 2010X. The late-time R and I band observations of SN 2005ek (at 40 and 70 days after peak) do perhaps indicate the presence of a radioactively powered light curve tail. The uncertain bolometric corrections, however, make it difficult to determine the actual gamma-ray trapping rate and hence radioactive mass. The late-time light curve decline is consistent with nearly complete gamma-ray trapping, as might be expected in a massive ($M \sim 3\mathrm{M}_{\odot}$) event. In this case, the inferred ^{56}Ni mass, while not zero, is very small, $M_{\mathrm{ni}} \approx 1 - 4 \times 10^{-3}$ $\mathrm{M}_{\odot}$. The luminosity at the light curve peak would then be attributed to an oxygen-plateau of the sort we have described.

In contrast, Drout et al. (2013) argue that if the ejecta mass and kinetic energy of SN 2005ek were relatively low ($M \approx 0.35 - 0.7$ $\mathrm{M}_{\odot}$, $E \approx 0.25 - 0.52$ B) then most of the gamma-rays escape at late times and the inferred ^{56}Ni mass is much larger, $M_{\mathrm{ni}} \approx 0.03$ $\mathrm{M}_{\odot}$, sufficient to power the light curve peak. It is not clear, however, that such a model can explain the rapid light curve decline after peak. Iwamoto et al. (1994) considered a similar model for SN 1994I with $M \approx 0.53$ $\mathrm{M}_{\odot}$, $E \approx 1$ B, $M_{\mathrm{ni}} \approx 0.08$ $\mathrm{M}_{\odot}$ and found light curves which declined less rapidly and showed a clear radioactive tail. More recently, models were explored in a different context by Fink et al. (2013), who calculated radiative transport models for similar scenarios (e.g., model ND3 with $M \approx 0.2$ $\mathrm{M}_{\odot}$, $E \approx 0.43$ B, $M_{\mathrm{ni}} \approx 0.07$ $\mathrm{M}_{\odot}$) and found light curves that decline fairly gradually, dropping by only ~ 1 mag in R-band in the 15 days after peak. This is much more gradual than either SN 2005ek or SN 2010X (which dropped ~ 3 R-band mags in 15 days). These results suggest that the radioactively powered model may struggle to explain the rapid decline that characterizes the class of RFSNe.

The light curve of SN 2002bj poses an even greater challenge for radioactively powered models. This event was significantly brighter than either SN 2005ek and SN 2010X, such that the inferred ^{56}Ni mass would be $M_{\rm ni} \approx 0.15 - 0.25$ M$_\odot$ (Poznanski et al. 2010). To be consistent with the rapid rise and steep decline of the light curve, one would need to assume a small ejecta mass, $M \sim 0.3$ M$_\odot$, such that the ejecta consisted of very little else but ^{56}Ni. This, however, contradicts the observed spectrum, which did not show strong features from iron group elements.

A potentially revealing empirical discriminant of the RFSNe is the ratio of the luminosity measured at peak to that on the radioactive tail. Some events, like SN 2002cx, SN 2005E and SN 2008ha, show a moderate peak-to-tail ratio, similar to SNe Ia and consistent with a light curve powered entirely by radioactivity. In contrast, the events considered here (SN 2005ek, SN 2010X, and SN 2002bj) show a larger peak-to-tail luminosity ratio (or no tail at all) more reminiscent of Type IIP supernova. It is possible that this distinction separates those events powered solely by radioactivity from those with an initial thermally powered oxygen (or helium) plateau.

The RFSNe also are distinguished by their host galaxies. All of SN 2010X, SN 2002bj, and SN 2005ek were found in star-forming galaxies and so are consistent with young stellar populations and massive star progenitors. Other types of RFSNe, however, such as SN 2005E and similar low-luminosity calcium-rich transients have often been found in the remote outskirts of elliptical galaxies, which almost exclusively harbor old stars. For these events, a different model, perhaps based on white dwarf progenitors, may be appropriate.

If correct, the identification of SN 2010X-like events as oxygen plateau SNe has two important implications for core-collapse SNe. The first is that some stripped-envelope SNe may eject a very small amount ($\lesssim 10^{-3}$ M$_\odot$) of radioactive isotopes. This may be because abundant radioactivity was not synthesized in the explosion or because the inner ejecta layers remained bound and fell back unto the compact remnant. The fallback process is not well understood; it has mostly been studied in parameterized 1-D models with an artificial inner boundary condition (e.g., Zhang et al. (2008), but see Ugliano et al. (2012)). Fallback is expected to be most significant in low-energy explosions, but it can also be substantial in more energetic SNe if a strong reverse shock propagates inward and decelerates the inner layers of ejecta (Chevalier 1989; Zhang et al. 2008; Dexter & Kasen 2013). If the progenitor experienced a heavy mass loss episode just prior to explosion (as we discuss below)

the interaction of the SN with the CSM could produce a reverse shock which may promote fallback of the inner ejecta.

The second implication of our analysis is that the progenitors of some stripped-envelope SNe may have surprisingly large initial radii, perhaps $R \sim 20\ R_\odot$ for SN 2010X and perhaps $R \gtrsim 100\ R_\odot$ for SN 2002bj. This is considerably larger the expected radii of most Wolf-Rayet (WR) stars, $R_0 \sim$ few $R_\odot$. Recent stellar evolution models suggest that some stars with helium envelopes can have radii on the order of $10\ R_\odot$ (Yoon et al. 2010). However, for SN 2010X we favor a composition dominated by oxygen, not helium. In the absence of some refinement of our understanding of stellar evolution, the large inferred radius presumably requires some mechanism to puff up an oxygen star prior to explosion.

One compelling explanation for the large radius is mass loss shortly before explosion. There are both observational and theoretical indications that instabilities can drive significant outflows from massive stars during the late stages of evolution (Woosley et al. 2007; Smith et al. 2011; Quataert & Shiode 2012; Smith & Arnett 2013). Most studies have focused on mass loss episodes occurring ~years prior to core collapse, which could explain the most luminous SNe observed (Smith et al. 2007; Gal-Yam 2012; Quimby 2012). If the expelled mass expands at roughly the escape velocity of a compact star (~ 1000 km s^{-1}), it will form a circumstellar shell at rather large radii, $R \sim 10^{15}$ cm. This shell, if it is optically thick, sets the effective "radius" of the progenitor, which can produce a very bright SN light curve ($L \sim 10^{44}$ ergs, see Equation 4.5).

The much fainter SN 2010X could be explained in a similar way if a circumstellar shell was located at a smaller radius, $R \sim 20\ R_\odot$. This would imply a much shorter time delay (~ 1 day) between mass loss and explosion. In fact, this dichotomy of timescales could be tied to the basic nuclear physics of massive stars; the timescale of the oxygen burning phase is ~ 1 year, while that of the silicon burning phase is ~ 1 day. If mass is lost during silicon burning at ~ 1000 km s^{-1}, the resulting circumstellar material would have reached a radius of $10^{12} - 10^{13}$ cm at the onset of core collapse a day or so later, setting the stage for a SN 2010X-like event. Because the shell is relatively close to the explosion site, any observational indications of interaction (e.g., narrow emission lines) would only be visible for a short time (~ 1 hour) after explosion.

Quataert & Shiode (2012) and Shiode & Quataert (2013) (see also Smith & Arnett 2013) have presented an explicit mechanism for mass loss related to core fusion.

They show that waves excited by vigorous convection during oxygen burning can (under certain circumstances) propagate through the star and deposit of order 10^{47} – 10^{48} ergs near the surface, sufficient to unbind ~ 10 $M_\odot$ in a red supergiant. They also show that for stripped-envelope stars, the sound-crossing time is short enough ($\lesssim 1$ day) for this mechanism to operate during silicon burning as well.

To explain the light curve of SN 2010X, the mass in the circumstellar shell (or inflated envelope) must be substantial enough to provide a sufficiently long light curve, which may require $M_{\rm csm} \gtrsim 0.5$ $M_\odot$ (using Equation 4.4 with a timescale of ~ 20 days, $E \sim 1$ B, and $R \sim 20$ $R_\odot$). The energy needed to drive this amount of material from a compact star is $\gtrsim 5\times10^{48}$ ergs. While this is only $\sim 1\%$ of the total energy released during silicon burning, most of the fusion energy is lost to neutrinos. In the specific models of Shiode & Quataert (2013), wave-driven mass loss in stripped-envelope stars only ejects $\lesssim 0.01$ $M_\odot$ of material in the silicon burning phase. However, more efficient mechanisms for mass loss may be possible (Smith & Arnett 2013), perhaps due to explosive burning episodes occurring when parcels of fuel are mixed downward into the hot core. Pulsational pair instabilities can in some circumstances also eject successive shells of material on the appropriate day timescale, in particular for the lower range of helium core masses (Woosley et al. 2007). Pulsational pair instabilities may not only act as a precursor for SN 2010X -like events by expanding the radius, but could also produce oxygen-rich and nickel-free transients themselves if they were to occur in stars stripped of their hydrogen and most of their helium (A. Heger, private communication). In this case, the star would remain after the event and could subsequently undergo more mass ejections or explode as a supernova.

There may be other ways to expand the effective radius of a stripped-envelope progenitor, perhaps related to stellar mergers or a common envelope phase in a binary system (e.g., Chevalier 2012). Alternatively, a large effective radius could be due to reheating of the SN remnant after it has expanded for a brief time. Dexter & Kasen (2013), for example, explore the possibility that the input of accretion power of a central black hole, fed by fallback material, can produce a diversity of SN light curves.

Though they have previously been seen as weak explosions, our analysis suggests that faint, fast SNe like SN 2010X may have more in common with the most luminous SNe in the Universe, namely the superluminous SNe powered by interaction with circumstellar material. In both cases, the progenitors may be massive stars that have experienced heavy mass loss just prior to explosion. The main distinction

in the observed light curve may simply be in the timing of the main pre-SN mass loss episode. Further detailed modeling is needed to investigate the dynamics of the interaction and the variety of outcomes and to determine whether realistic progenitors can produce core-collapse SNe of this type.

References

Abdikamalov, E. B., Ott, C. D., Rezzolla, L., et al., 2010, PhRvD, 81.4, 044012, 044012

Arnett, W. D., 1979, ApJL, 230, L37

Bildsten, L., Shen, K. J., Weinberg, N. N., & Nelemans, G., 2007, ApJL, 662, L95

Chevalier, R. A., 1989, ApJ, 346, 847

—, 1992, ApJ, 394, 599

—, 2012, ApJL, 752, L2, L2

Contardo, G., Leibundgut, B., & Vacca, W. D., 2000, A&A, 359, 876

Darbha, S., Metzger, B. D., Quataert, E., et al., 2010, MNRAS, 409, 846

Dessart, L., Burrows, A., Ott, C. D., et al., 2006, ApJ, 644, 1063

Dessart, L., & Hillier, D. J., 2008, MNRAS, 383, 57

Dessart, L., Hillier, D. J., Livne, E., et al., 2011, MNRAS, 414, 2985

Dessart, L., Hillier, D. J., Li, C., & Woosley, S., 2012, MNRAS, 424, 2139

Dexter, J., & Kasen, D., 2013, ApJ, 772, 30, 30

Drout, M. R., Soderberg, A. M., Mazzali, P. A., et al., 2013, ApJ, 774, 58, 58

Ensman, L. M., & Woosley, S. E., 1988, ApJ, 333, 754

Fink, M., Kromer, M., Seitenzahl, I. R., et al., 2013, ArXiv e-prints

Foley, R. J., Challis, P. J., Chornock, R., et al., 2013, ApJ, 767, 57, 57

Fryer, C. L., Brown, P. J., Bufano, F., et al., 2009, ApJ, 707, 193

Gal-Yam, A., 2012, Science, 337, 927

Grassberg, E. K., Imshennik, V. S., & Nadyozhin, D. K., 1971, Ap&SS, 10, 28

Iwamoto, K., Nomoto, K., Hoflich, P., et al., 1994, ApJL, 437, L115

Kasen, D., Thomas, R. C., & Nugent, P., 2006, ApJ, 651, 366

Kasen, D., & Woosley, S. E., 2009, ApJ, 703, 2205

species	inner abundance[a]	outer abundance[b]
H	1.3441e-14	—
He	7.2524e-13	9.8671e-01
Li	—	1.0043e-08
Be	—	1.7418e-10
B	—	4.9905e-09
C	1.3561e-02	2.2179e-03
N	2.3119e-09	7.1266e-04
O	6.5954e-01	5.9003e-03
F	—	3.9087e-07
Ne	1.5747e-01	1.1163e-03
Na	3.4553e-05	3.4553e-05
Mg	2.7580e-02	6.4116e-04
Al	—	5.8630e-05
Si	9.5727e-02	7.3099e-04
P	—	6.7316e-06
S	3.9061e-02	3.7317e-04
Cl	—	4.7954e-06
Ar	4.4617e-03	9.6441e-05
K	—	3.7829e-06
Ca	1.2866e-03	6.5889e-05
Sc	—	3.9365e-08
Ti	2.8182e-06	2.8182e-06
V	—	3.6517e-07
Cr	2.9462e-06	1.6984e-05
Mn	—	1.4106e-05
Fe	1.3033e-03	1.2132e-03
Co	3.4272e-06	3.4272e-06
Ni	7.0975e-05	7.0975e-05

Table 4.1: Mass fractions used for the composition in the radiative transport models. The boundary between inner and outer zones is at 10^9 cm. For some isotopes in the inner layer, the abundance was increased to solar.

[a] Woosley et al. (2002) oxygen/neon-rich composition. [b] Solar composition from Lodders (2003) with all hydrogen converted to helium.

Kasliwal, M. M., Kulkarni, S. R., Gal-Yam, A., et al., 2010, ApJL, 723, L98

Kasliwal, M. M., Kulkarni, S. R., Gal-Yam, A., et al., 2012, ApJ, 755, 161, 161

Kawabata, K. S., Maeda, K., Nomoto, K., et al., 2010, Nature, 465, 326

Kromer, M., Fink, M., Stanishev, V., et al., 2013, MNRAS, 429, 2287

Lodders, K., 2003, ApJ, 591, 1220

Lucy, L. B., 1991, ApJ, 383, 308

Metzger, B. D., Piro, A. L., & Quataert, E., 2009, MNRAS, 396, 1659

Moriya, T., Tominaga, N., Tanaka, M., et al., 2010, ApJ, 719, 1445

Perets, H. B., Gal-Yam, A., Mazzali, P. A., et al., 2010, Nature, 465, 322

Pinto, P. A., & Eastman, R. G., 2000, ApJ, 530, 757

Popov, D. V., 1993, ApJ, 414, 712

Poznanski, D., Chornock, R., Nugent, P. E., et al., 2010, Science, 327, 58

Quataert, E., & Shiode, J., 2012, MNRAS, 423, L92

Quimby, R. M., 2012, in IAU Symposium, Death of Massive Stars: Supernovae and Gamma-Ray Bursts, Vol. 279, 22

Sauer, D. N., Mazzali, P. A., Deng, J., et al., 2006, MNRAS, 369, 1939

Shen, K. J., Kasen, D., Weinberg, N. N., Bildsten, L., & Scannapieco, E., 2010, ApJ, 715, 767

Shiode, J. H., & Quataert, E., 2013, ArXiv e-prints

Smith, N., Li, W., Foley, R. J., et al., 2007, ApJ, 666, 1116

Smith, N., Li, W., Filippenko, A. V., & Chornock, R., 2011, MNRAS, 412, 1522

Smith, N., & Arnett, D., 2013, ArXiv e-prints

Ugliano, M., Janka, H.-T., Marek, A., & Arcones, A., 2012, ApJ, 757, 69, 69

Woosley, S. E., 1988, ApJ, 330, 218

Woosley, S. E., Heger, A., & Weaver, T. A., 2002, Reviews of Modern Physics, 74, 1015

Woosley, S. E., Blinnikov, S., & Heger, A., 2007, Nature, 450, 390

Yoon, S.-C., Woosley, S. E., & Langer, N., 2010, ApJ, 725, 940

Young, T. R., Baron, E., & Branch, D., 1995, ApJL, 449, L51

Zhang, W., Woosley, S. E., & Heger, A., 2008, ApJ, 679, 639

Chapter 5

MODELS OF BRIGHT NICKEL-FREE SUPERNOVAE FROM STRIPPED MASSIVE STARS WITH CIRCUMSTELLAR SHELLS

ABSTRACT

The nature of an emerging class of rapidly fading supernovae (RFSNe)—characterized by their short-lived light curve duration, but varying widely in peak brightness—remains puzzling. Whether the RFSNe arise from low-mass thermonuclear eruptions on white dwarfs or from the core collapse of massive stars is still a matter of dispute. We explore the possibility that the explosion of hydrogen-free massive stars could produce bright but rapidly fading transients if the effective pre-supernova radii are large and if little or no radioactive nickel is ejected. The source of radiation is then purely due to shock cooling. We study this model of RFSNe using spherically symmetric hydrodynamics and radiation transport calculations of the explosion of stripped stars embedded in helium-dominated winds or shells of various masses and extent. We present a parameter study showing how the properties of the circumstellar envelopes affect the dynamics of the explosion and can lead to a diversity of light curves. We also explore the dynamics of the fallback of the innermost stellar layers, which might be able to remove radioactive nickel from the ejecta, making the rapid decline in the late time light curve possible. We provide scaling relations that describe how the duration and luminosity of these events depend on the supernova kinetic energy and the mass and radius of the circumstellar material.

5.1 Introduction

The population of observed supernovae (SNe) is growing swiftly as high-cadence surveys fill regions of observational phase space that were previously much less accessible. Among the peculiar objects found are a class of rapidly fading supernovae (RFSNe) with peak luminosities ranging widely from sub-luminous to brighter than “normal" SNe. Well known single objects include SN 2002bj (Poznanski et al. 2010), SN 2010X (Kasliwal et al. 2010), and SN 2015U (Shivvers et al. 2016), but studies of the larger population have also emerged (e.g., Drout et al. 2014; Arcavi et al. 2016). The progenitor systems and explosion mechanisms of RFSNe these events remain in dispute.

RFSNe exist in what is currently the shortest-timescale region of optical observational parameter space, with rise and decline times lasting days to weeks. If these transients are interpreted as powered by centrally concentrated radioactive ^{56}Ni, the total ejected mass must be small (~ 0.1 M$_\odot$, assuming a constant opacity) so as to produce a short effective diffusion time. Several theoretical models may produce such ejecta, for example the thermonuclear detonation of a helium shell atop a white dwarf (a “point Ia supernova", Bildsten et al. 2007; Shen et al. 2010), the explosion of a highly stripped massive star (Tauris et al. 2015), or a core collapse supernova experiencing heavy fallback (Moriya et al. 2010).

However, low-mass ^{56}Ni powered models likely cannot explain many of the RFSNe. The light curves of many observed events show no noticeable late-time “tail" indicating a continuing input of decay energy (although incomplete trapping of the radioactive γ-rays could perhaps explain this behavior). Moreover, some objects, such as SN 2002bj and SN 2015U , are so bright that simple analytic estimates lead to the unphysical inference that the mass of ^{56}Ni must be larger than the total ejecta mass. For such reasons, Drout et al. (2014) conclude that many of the RFSNe are likely powered by shock energy rather than radioactivity.

Previous modeling in Chapter 4 (Kleiser & Kasen 2014) has shown that some RFSNe like SN 2010X could be explained by the explosion of a hydrogen-poor star with a relatively large radius ($\sim 20\ R_\odot$). The ejected mass of radioactive isotopes was assumed to be small, such that the luminosity was powered by diffusion of the shock deposited energy. The model light curves declined rapidly due to recombination in the cooling ejecta (composed of helium or carbon/oxygen) which reduced the opacity and led to a rapid depletion of the thermal energy, similar to the end of the plateau in Type IIP SN. Dim transients of this sort had been studied in the SNIb

models of Dessart et al. (2011).

To produce a bright RFSN from shock cooling requires a progenitor star with a radius much greater than the few $R_\odot$ found in stellar evolution models of hydrogen-stripped stars (Crowther 2007). Kleiser & Kasen 2014 (Chapter 4) suggested that the effective presupernova star radius may be increased due to envelope inflation of mass loss just prior to explosion. Strong mass-loss episodes could arise due to binary interaction (Chevalier 2012) or dynamics driven by nuclear burning (Quataert & Shiode 2012; Smith 2016). Indeed, the spectra of Type Ibn SN (e.g. Pastorello et al. 2015; Pastorello et al. 2016, and citations therein) and of SN 2015U provide direct evidence for a hydrogen-poor circumstellar medium (CSM) around some massive star explosions.

In this chapter, we pursue the shock cooling model for RFSN by carrying out a parameter study of the dynamics and shock cooling light curves of supernova exploding into an extended, hydrogen poor CSM. In §5.2, we provide simple analytic scalings for how the interaction dynamics and resulting light curve should depend on physical parameters such as the mass and radius of the CSM shell. In §5.3, we describe a pipeline to model the 1D hydrodynamics of the interaction and the subsequent light curves. In §5.4, we show how different shell parameters affect the dynamics and the possibility of fallback. We present light curves for nickel-free and nickel-rich ejecta profiles, and we explore how Ralyeigh-Taylor mixing effects may effect the results. Finally, §5.5 contains discussion of our results and their implications for our understanding of RFSNe and the possible outcomes of stellar evolution that could produce such peculiar objects.

5.2 Analytics

We first present simple analytic scalings that can be used to estimate the properties of interacting SNe. As an idealized model, we consider the case of homologously expanding SN ejecta running into a stationary CSM shell or wind. Although the interaction with the CSM will generally occur before the stellar ejecta has had time to establish homology, our hydrodynamical models (see §5.4) indicate that the post-shock velocity structure of the exploded star is approximately linear in radius. We therefore assume the ejecta velocity at radius r and time t is $v = r/t$ and describe the ejecta structure with a broken power law profile (Chevalier 1989a) in which the density in the outer layers (above a transition velocity v_t) is

$$\rho_{\rm ej} \propto \frac{M_{\rm ej}}{v_t^3 t^3}\left(\frac{r}{v_t t}\right)^{-n}, \tag{5.1}$$

where $v_t \propto (E_{\rm exp}/M_{\rm ej})^{1/2}$, and $M_{\rm ej}$ is the ejecta mass and $E_{\rm exp}$ the energy of the explosion.

Interaction with the (nearly) stationary CSM will decelerate the ejecta and convert its kinetic energy into thermal energy. By conservation of momentum, the mass of ejecta that can be significantly decelerated in the interaction is of order the total mass of the CSM. For the power-law density profile, the ejecta mass above some velocity coordinate $v_0 > v_t$ is

$$M(v_0) = \int_{v_0}^{\infty} 4\pi r^2 \rho_{\rm ej}(r) dr \propto \frac{4\pi}{n-3} M_{\rm ej} \left(\frac{v_0}{v_t}\right)^{3-n} \tag{5.2}$$

which assumes $n > 3$. Setting $M(v_0) \sim M_{\rm CSM}$ (where $M_{\rm CSM}$ is the total CSM mass) implies that the velocity coordinate above which the ejecta is slowed by the interaction is

$$v_0 \propto v_t \left(\frac{M_{\rm ej}}{M_{\rm CSM}}\right)^{\frac{1}{n-3}} .$$

The ejecta kinetic energy contained in the layers above v_0 is

$$\mathrm{KE}(v_0) \;=\; \int_{v_0}^{\infty} \frac{1}{2} \rho_{\rm ej} v^2 4\pi r^2 dr \propto M_{\rm ej} v_t^2 \left(\frac{v_0}{v_t}\right)^{5-n} \tag{5.3}$$

which suggests that the energy thermalized in the interaction should scale as

$$E_{\rm th,0} \propto \mathrm{KE}(v_0) \propto M_{\rm ej} v_t^2 \left(\frac{M_{\rm CSM}}{M_{\rm ej}}\right)^{\frac{n-5}{n-3}} . \tag{5.4}$$

For $n = 8$, for example, the energy thermalized scales as $(M_{\rm CSM}/M_{\rm ej})^{3/5}$.

The thermalization of the ejecta kinetic energy will occur over the timescale for the ejecta to accelerate the CSM. To estimate the interaction timescale we follow the self-similar arguments of (Chevalier 1992) and assume that the CSM has a power-law density structure of the form

$$\rho_{\rm CSM}(r) \propto \frac{M_{\rm CSM}}{R_{\rm CSM}^3} \left(\frac{r}{R_{\rm CSM}}\right)^{-s} , \tag{5.5}$$

where $R_{\rm CSM}$ is the outer radius of the CSM and $s < 3$. In a self-similar interaction, the ejecta and CSM densities maintain a constant ratio at the contact discontinuity, $\rho_{\rm ej}(r_c)/\rho_{\rm CSM}(r_c) = C$, with C a constant. This implies that r_c, the radius of the contact discontinuity between the ejecta and CSM, evolves as (Chevalier 1992)

$$r_c(t) = t^{\frac{n-3}{n-s}} \left[\frac{M_{\rm ej}}{M_{\rm CSM}} \frac{R_{\rm CSM}^{3-s}}{C v_t^{3-n}}\right]^{\frac{1}{n-s}} . \tag{5.6}$$

Setting $r_c(t) \approx R_{\rm CSM}$ gives an estimate of the time $t_{\rm bo}$ when the forward shock from interaction will break out of the CSM (Harris et al. 2016):

$$t_{\rm bo} \approx \frac{R_{\rm CSM}}{v_t}\left(\frac{CM_{\rm CSM}}{M_{\rm ej}}\right)^{\frac{1}{n-3}} . \tag{5.7}$$

The total amount of ejecta kinetic energy thermalized will rise until $t \approx t_{\rm bo}$, then decline as the interaction abates and the system adiabatically expands. Because the pressure is radiation-dominated (adiabatic index $\gamma = 4/3$), the thermal energy after expansion to a radius $R(t)$ is

$$E_{\rm th}(t) = E_{\rm th,0}\frac{R_{\rm CSM}}{R(t)} \propto E_{\rm th,0}\left(\frac{t_{\rm bo}}{t}\right) , \tag{5.8}$$

where $R(t)$ is the radius of the expanding, post-interaction ejecta, and the last equation assumes homologous expansion, $R(t) \sim t$, following the breakout. The thermal energy at time t is then

$$E_{\rm th}(t) \propto R_{\rm CSM}M_{\rm ej}^{1/2}E_{\rm exp}^{1/2}\left(\frac{M_{\rm CSM}}{M_{\rm ej}}\right)^{\frac{n-4}{n-3}} t^{-1}. \tag{5.9}$$

For the case of $n = 8$, for example, which will approximate the post-shock density structure of our hydrodynamical models, we have

$$E_{\rm th}(t) \propto R_{\rm CSM}E_{\rm exp}^{1/2}M_{\rm CSM}^{4/5}M_{\rm ej}^{-4/5}t^{-1}. \tag{5.10}$$

We will show using hydrodynamical models in §5.4 that Equation 5.10 accurately predicts how the thermal energy content depends on the CSM and ejecta properties. The derivation assumes $M_{\rm CSM} \lesssim M_{\rm ej}$.

The light curves arising from the interaction are the result of the diffusion of thermal radiation from the shocked region. The opacity κ is usually dominated by electron scattering and is constant in ionized regions, but will drop sharply to near zero once the temperature drops below the recombination temperature T_I. Scaling relations for the duration and peak luminosity of thermal supernovae, including the effects of recombination, have been determined by Popov (1993) and verified numerically by Kasen & Woosley (2009):

$$t_{\rm sn} \propto E_{\rm th,0}^{-1/6}M_{\rm diff}^{1/2}R_0^{1/6}\kappa^{1/6}T_I^{-2/3}, \tag{5.11}$$

$$L_{\rm sn} \propto E_{\rm th,0}^{5/6}M_{\rm diff}^{-1/2}R_0^{2/3}\kappa^{-1/3}T_I^{4/3} , \tag{5.12}$$

where $M_{\rm diff}$ is the effective amount of mass the photons must diffuse through. We take this to be some combination of $M_{\rm ej}$ and $M_{\rm CSM}$, depending on the distribution

of thermal energy among the relative masses. Taking $R_0 = R_{\rm CSM}$ and using our Equation 5.4 for $E_{\rm th,0}$ gives

$$t_{\rm sn} \propto E_{\rm exp}^{-1/6} \left(\frac{M_{\rm CSM}}{M_{\rm ej}} \right)^{\frac{-(n-5)}{6(n-3)}} M_{\rm diff}^{1/2} R_{\rm CSM}^{1/6} \kappa^{1/6} T_I^{-2/3} \ , \tag{5.13}$$

$$L_{\rm sn} \propto E_{\rm exp}^{5/6} \left(\frac{M_{\rm CSM}}{M_{\rm ej}} \right)^{\frac{5(n-5)}{6(n-3)}} M_{\rm diff}^{-1/2} R_{\rm CSM}^{2/3} \kappa^{-1/3} T_I^{4/3} \ . \tag{5.14}$$

For the purposes of easy comparison to numerical data, we would like to devise simple power laws to describe the dependency of $L_{\rm sn}$ and $t_{\rm sn}$ on the parameters. This is complicated by the $M_{\rm diff}$ factor, but there are limits we can consider. First it is necessary to recognize that the masses change the light curve in two opposing ways: increasing $\frac{M_{\rm CSM}}{M_{\rm ej}}$ increases the amount of available thermal energy to power the light curve, which would increase the peak luminosity and decrease the timescale, according to Equations 5.11 and 5.12. Meanwhile, the diffusion mass $M_{\rm diff}$ also slows the diffusion of photons out of the ejecta more as it increases, lowering the peak luminosity and increasing the timescale.

In the cases presented here, we hold $M_{\rm ej}$ fixed. One limit is to imagine that the circumstellar mass is small compared to the ejecta mass, so the dependence on $M_{\rm diff}$ goes away. Then the equations become

$$t_{\rm sn} \propto E_{\rm exp}^{-1/6} M_{\rm CSM}^{\frac{-(n-5)}{6(n-3)}} R_{\rm CSM}^{1/6} \kappa^{1/6} T_I^{-2/3} \ , \tag{5.15}$$

$$L_{\rm sn} \propto E_{\rm exp}^{5/6} M_{\rm CSM}^{\frac{5(n-5)}{6(n-3)}} R_{\rm CSM}^{2/3} \kappa^{-1/3} T_I^{4/3} \ . \tag{5.16}$$

In the case of $n = 8$, we then have $t_{\rm sn} \propto M_{\rm CSM}^{-1/10}$ and $L_{\rm sn} \propto M_{\rm CSM}^{1/2}$. If $n = 6$, $t_{\rm sn} \propto M_{\rm CSM}^{-1/18}$ and $L_{\rm sn} \propto M_{\rm CSM}^{5/18}$.

This limit essentially assumes the increase in circumstellar mass does not contribute significantly to inhibiting the travel of photons out of the ejecta. Alternatively, we can imagine that the CSM makes up the bulk of the mass available, or that the total mass scales roughly as the CSM mass. In this case, $M_{\rm diff} \propto M_{\rm CSM}$, so

$$t_{\rm sn} \propto E_{\rm exp}^{-1/6} M_{\rm CSM}^{\frac{-(n-5)}{6(n-3)}+\frac{1}{2}} R_{\rm CSM}^{1/6} \kappa^{1/6} T_I^{-2/3} \ , \tag{5.17}$$

$$L_{\rm sn} \propto E_{\rm exp}^{5/6} M_{\rm CSM}^{\frac{5(n-5)}{6(n-3)}-\frac{1}{2}} R_{\rm CSM}^{2/3} \kappa^{-1/3} T_I^{4/3} \ . \tag{5.18}$$

For $n = 8$, $t_{\rm sn} \propto M_{\rm CSM}^{2/5}$ and $L_{\rm sn} \propto M_{\rm CSM}^{0}$. For $n = 6$, $t_{\rm sn} \propto M_{\rm CSM}^{4/9}$ and $L_{\rm sn} \propto M_{\rm CSM}^{-2/9}$. We will find in §5.4 that this last case with $n = 6$ appears to fit our numerical results for the light curves most closely.

5.3 Methods

We adopt a spherically symmetric framework to model the light curves of hydrogen-poor stars exploding into an extended CSM. We use the MESA stellar evolution code to model massive stars that have lost their hydrogen envelopes due to heavy mass loss. At the point of core collapse, we add to the MESA models a parameterized external shell or wind of mass $M_{\rm CSM}$. We map this progenitor structure into a 1D hydrodynamics code and explode it by depositing a central bomb of thermal energy. Once the ejecta have neared homologous expansion, the structure is fed into the SEDONA radiation transport code to calculate time-dependent light curves and spectra.

Progenitor Star Models

We use MESA version 7184 to produce a hydrogen-stripped stellar model using a simple artificial mass loss prescription. The prescription is meant to approximate Case B mass transfer to a binary companion, which should be common among the massive progenitors of Type Ibc SNe (see Sana et al. 2012; Smith et al. 2011). We use a zero-age main sequence (ZAMS) mass of 20 $M_\odot$ and evolve the star through hydrogen burning until the surface temperature reaches $T_{\rm eff}$ = 5000 K, indicating that the radius has expanded significantly. We then initiate a constant mass loss at $\dot{M} = 10^{-3}$ $M_\odot$ yr^{-1} until a desired final mass is reached, in the present case 5 $M_\odot$. This mass loss history qualitatively resembles the more detailed Roche lobe overflow calculations in Yoon et al. (2010). Therefore, even though the mass loss prescription is simple, it is similar to the natural loss of a large amount of mass (in this case the entire hydrogen envelope) expected in some systems by Roche lobe overflow. Other or more complex mass loss histories may yield different final stellar structures.

The MESA model is evolved to the point of iron core collapse. Before exploding the model, we first cut out the remnant based on the point at which ^{56}Fe drops below 10% going outward—in our case, the remnant mass is 1.395 $M_\odot$. We then insert an ad-hoc distribution of extended CSM, which is meant to mock up a heavy mass loss episode in the final days before explosion. We assume that the CSM mass was lost at a constant velocity, $v_{\rm CSM} \ll v_{\rm ej}$ with a rate $\dot{M}$ that was Gaussian in time. This leads to a CSM density profile

$$\rho_{\rm CSM}(r) = \frac{M_{\rm CSM}}{4\pi r^2 \Delta r \sqrt{2\pi}} \exp\left[\frac{-(r - r_{\rm mid})^2}{2\Delta r}\right], \tag{5.19}$$

where $r_{\rm mid}$ and Δr are free parameters specifying, respectively, the peak and the width

of the Gaussian. For a constant mass rate and wind velocity, $\Delta r = v_{\rm CSM}\tau$ where τ is the standard deviation of the Gaussian and can be used as a measure of the duration of the mass loss episode. For large values of τ, the CSM resembles that of a constant $\dot{M}$ wind with a $1/r^2$ density profile. We chose here $v_{\rm CSM} = 100$ km s^{-1}. While the value of $v_{\rm CSM}$ would be interesting in the context of understanding the nature and mechanism of the mass loss, here the actual quantity is of little consequence for the light curves and spectra since the velocity of the ejecta is so much greater.

Figure 5.1 shows the density profile of the progenitor star model with a few different distributions of CSM. Figure 5.2 shows the composition of a progenitor model. We assume that the CSM composition is homogenous and equal to that at the surface of the stellar model, which is helium-dominated.

Our parameterized progenitor configuration is artificial in that the progenitor star structure is not self-consistently altered to compensate for the presumed final episodes of mass loss. In addition, in some models we rescale the mass of the progenitor star by simply dividing the density profile everywhere by a constant. The assumption is that the density profile of our MESA progenitor star provides a reasonable representation of presupernova stars of other masses. In the present context, a simplified approach is not unreasonable in that we will explode the star with a 1D thermal bomb, and the detailed internal structure of the star will be largely washed out by the blastwave. What is most important to the light curve is the structure of the CSM, which in the present case is parameterized in a simplified way that allows us to easily control the physical characteristics. Future studies using more realistic CSM structures and progenitors are clearly warranted.

Hydrodynamical Explosion Simulations

For modeling the explosion of the star, we use a 1D staggered moving-mesh hydrodynamical code and a gamma-law equation of state with $\gamma = 4/3$, as the SN shock is radiation-pressure dominated. We do not compute the complex mechanism of the explosion itself but instead deposit a chosen amount of thermal energy $E_{\rm exp}$ at the center of the stellar model to create a thermal bomb. We evolve the explosion until the ejecta profile is roughly homologous, i.e. $r \sim vt$ for all zones. This method has the advantage of speed but is limited to cases in which the CSM radius is small enough that radiative diffusion is not important before homology is reached.

In the hydrodynamical calculation, some inner zones may remain bound and fall back toward the remnant. In order to capture this, we use the following criteria

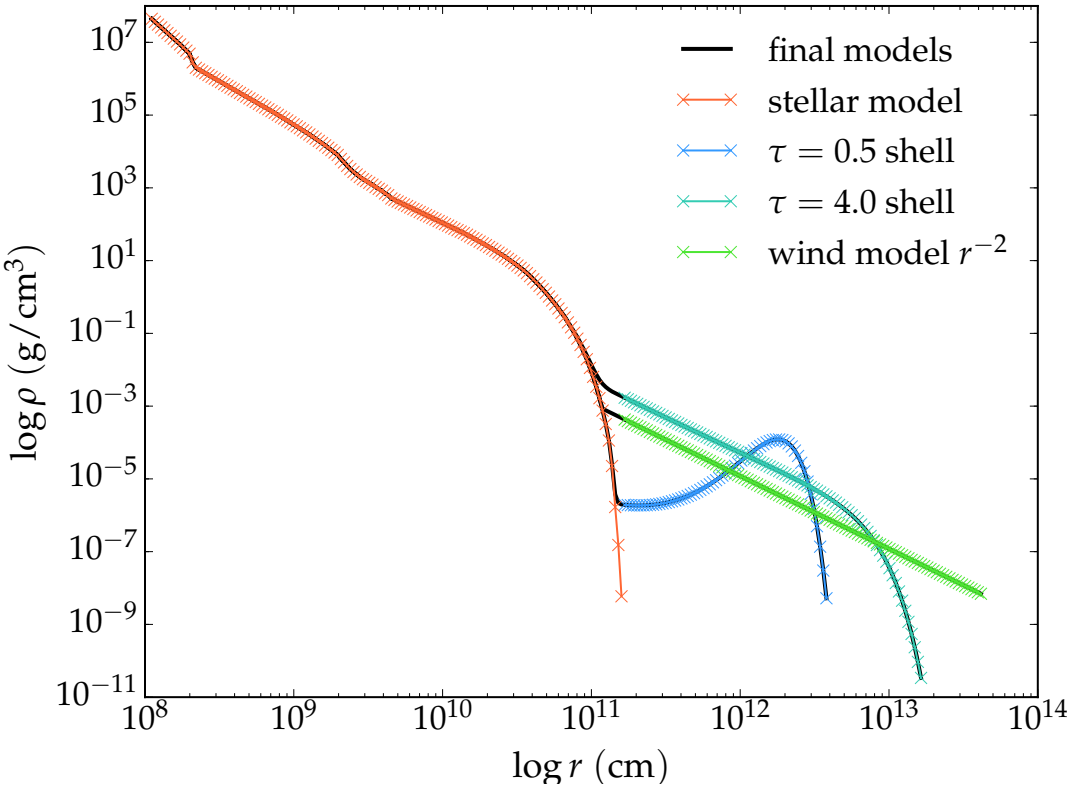

Figure 5.1: Density profile for an example star + shell model. The same stripped MESA star model is used throughout this chapter, and different toy shells are constructed around it. The original stellar profile is shown in orange. Blue-green colors show various shell profiles. Two of the shells shown here are Gaussian profiles modified by r^{-2} based on the fact that we assumed a Gaussian $\dot{M}$ whose velocity was constant (see Equation 5.19) with different values of τ. The third is simply a density profile $\propto r^{-2}$, corresponding to a constant wind prior to explosion. This is essentially the case of infinite τ. Final models are shown in black, with a smooth transition between stellar and shell densities. All shells in this plot have the same amount of total mass.

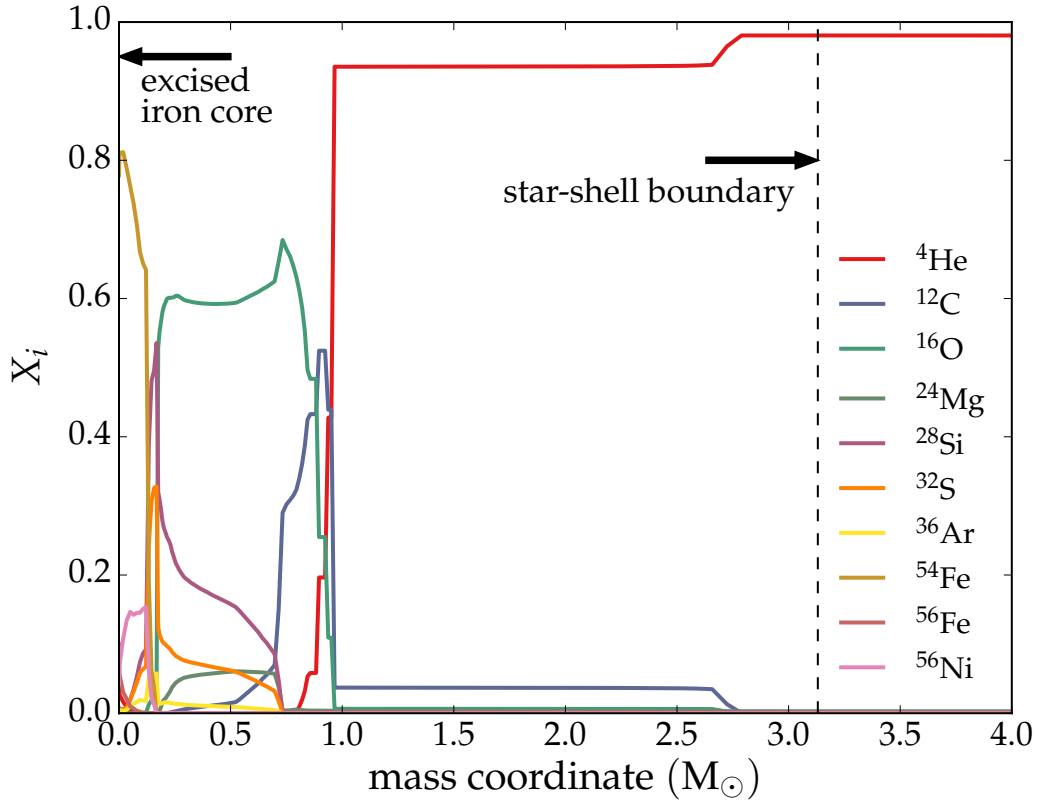

Figure 5.2: Composition plot for an example star + shell model. The iron core has been removed already by cutting out the mass interior to the point where ^{56}Fe drops below 10% of the composition. The star used for all runs is the same, and the shell is assumed to have the same abundances as the outermost layer of the star. In this case, all shells are very dominated by ^{4}He. The dotted black line indicates where the star ends and the shell begins.

to determine if the innermost zone should be “accreted" and removed from the calculation: 1) the zone has negative velocity; and 2) the gravitational potential energy of the zone exceeds the kinetic and thermal energy of the zone combined by a factor of $1 + \epsilon$, where we typically take ϵ to be ~ 0.2. Sometimes an innermost zone will also be removed if its density is some factor η larger than the density of the next zone, where η is typically ~ 100. The density criterion is used because sometimes a zone that is considered unbound by the prior criteria will nevertheless remain spatially small, which imposes a very small time step on the calculation without significantly affecting the results.

Radiative Transfer Calculations

Once our exploded profiles are close to homology, we map the final ejecta structure into SEDONA, a time-dependent Monte Carlo radiation transport code that takes into account the composition, density, and temperature-dependent opacities (Kasen et al. 2006). We run the code with the assumption of local thermodynamic equilibrium (LTE), which should be reasonable for approximating the phases of the light curve after which interaction with the CSM has taken place, but before the ejecta have become optically thin.

For the models in which we include ^{56}Ni in the ejecta, we assume the nickel mass fraction $X_{\rm ni}$ profile follows

$$X_{\rm ni} = \frac{1}{2}\left(\tanh\left[\frac{-(r - r_{\rm ni})}{s\,dr}\right] + 1\right), \tag{5.20}$$

where dr is the width of each zone. This equation essentially produces a smoothed step function where s controls the amount of smoothing and the quantity $r_{\rm ni}$ is the shift required, given s to make the total mass of nickel present match a user-specified $M_{\rm ni}$. In this chapter, every SEDONA run has the same number of equally spaced radial zones ($N = 200$), so $s\,dr$ represents the spatial extent of the smearing and is a fraction of the radial extent of the ejecta controlled by s.

5.4 Results

Dynamics of Interaction

We present here a study of hydrodynamical simulations of the explosion of the described progenitor star plus CSM configuration. Figure 5.3 compares the velocity evolution of a model with no CSM to one with a 3 $M_\odot$ CSM shell. In both models, a strong shock initially propagates outward through the star, reaching the surface (at mass coordinate 3.4 $M_\odot$) at a time $t \approx 10^2$ s. In the model with no CSM, the shock breaks out and accelerates the surface layers of the star to high velocity. In the model with a CSM shell, the interaction produces a reverse shock and a forward shock, the latter of which breaks out of the CSM shell some time later ($t \approx 10^4$ s). The reverse shock weakens after the forward shock breakout due to the pressure release and stalls before reaching the ejecta center.

Figure 5.4 shows the temporal exchange of kinetic and thermal energy in a model with a total kinetic energy at infinity of 1 B. The thermal energy declines over the intial $\sim$ 300 seconds as the shock travels through the star, overcoming the gravitational binding energy and imparting kinetic energy to the stellar material. In

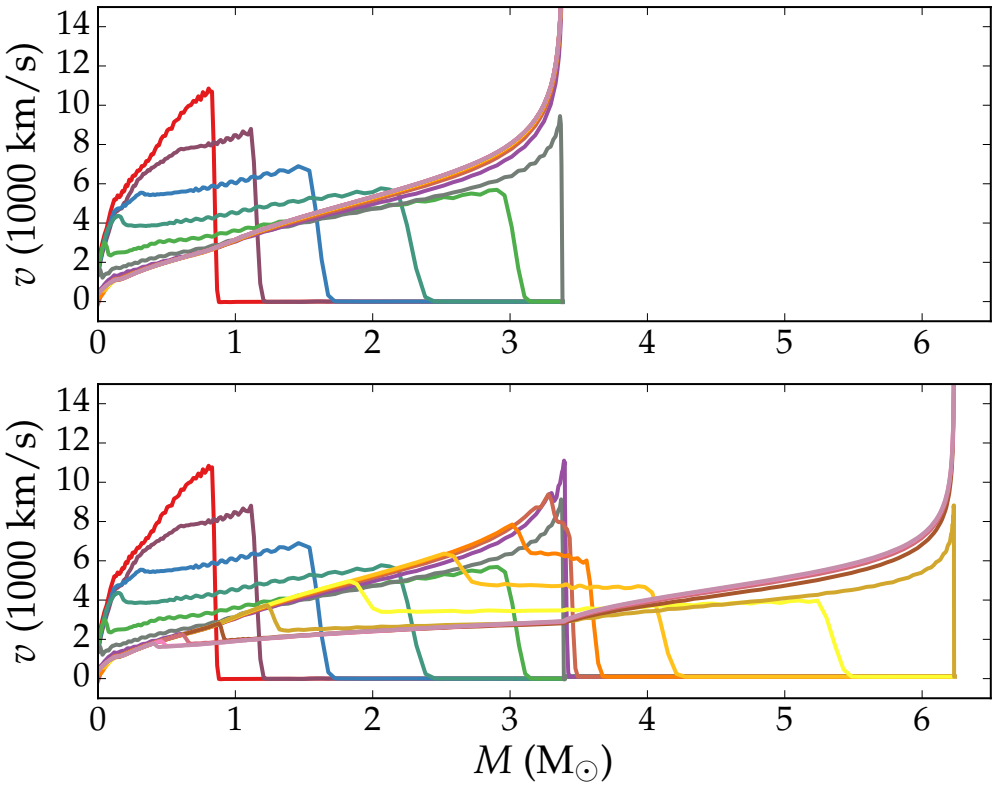

Figure 5.3: Velocity profiles at various times for two hydrodynamical calculations. Each profile corresponds to roughly a doubling in time, i.e. $\sim$ 2 s, $\sim$ 4 s, $\sim$ 8 s, and so forth. Top panel: explosion of a 5 $M_\odot$ progenitor star ($\sim$ 3.4 $M_\odot$ once the iron core is removed) with no CSM added. Bottom panel: explosion of the same star with a 3 $M_\odot$ CSM. The addition of the CSM slows down the forward shock, producing a reverse shock moving toward the center.

the absence of a CSM shell, Figure 5.4 shows that the thermal energy continues to decline to late times due to expansion loss. In the presence of a CSM shell, however, the outer layers of stellar ejecta impact the shell at $\sim$ 300 s and shocks begin to convert kinetic energy back into thermal energy again. The thermal energy content peaks around 5×10^3 seconds, which occurs shortly before the breakout of the forward shock from the CSM. Thereafter, the thermal energy declines again as $1/t$, as expected from $p\,dV$ loses.

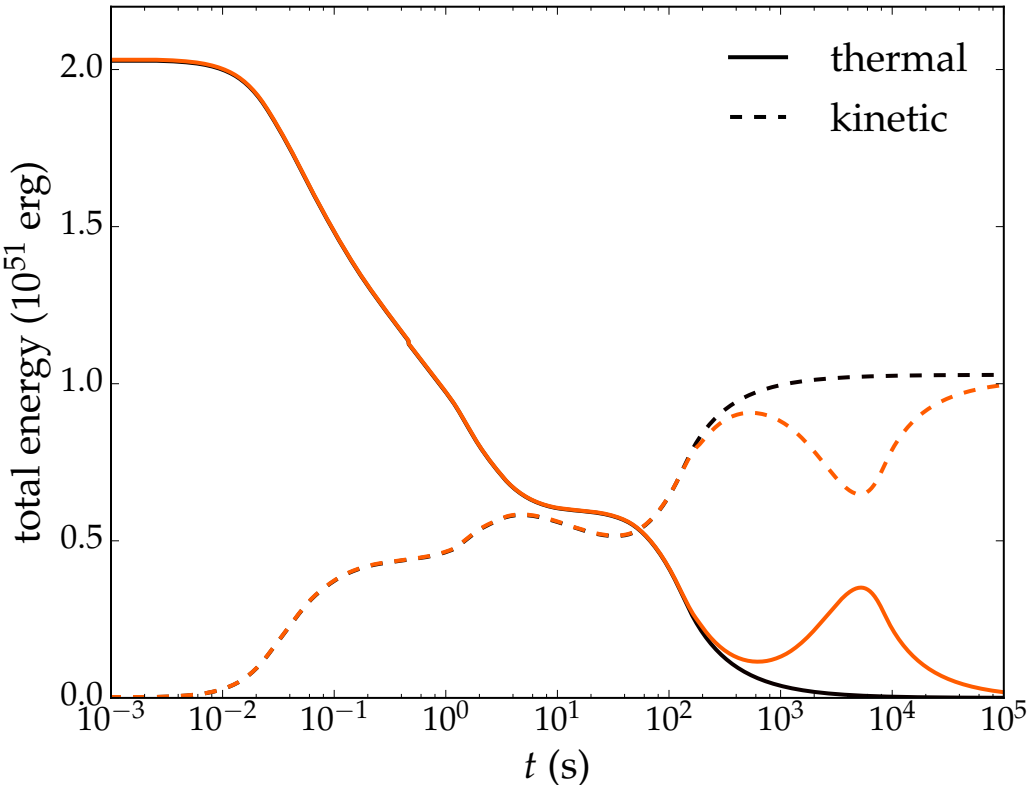

Figure 5.4: Evolution of the total kinetic and thermal energy in the explosion of a 5 $M_\odot$ star with 3 $M_\odot$ of CSM (red lines). For comparison, a model with no CSM is also shown (black lines) A central thermal bomb is input to give an initial thermal energy just above 2 B, resulting in a final kinetic energy of 1 B once the gravitational potential has been overcome. At the earliest times ($t \lesssim 10^2$ s), thermal energy is converted to kinetic energy as the star explodes. The interaction with the CSM begins at times $t \gtrsim 10^2$ s and converts kinetic energy back into thermal energy. At a time near 10^4 s, the forward shock breaks out of the CSM. Thereafter the thermal energy declines, closely following the t^{-1} scaling of adiabatic homologous expansion.

Parameter Study

Figure 5.5 shows how the thermal energy evolution depends on the ejecta and CSM parameters. The end result is quantified further in Figure 5.6, which shows the thermal energy content $E_{\rm th}(t_{\rm end})$ found at a final reference time $t_{\rm end} = 10^5$ s. The general trends noted are: 1) $E_{\rm th}(t_{\rm end})$ increases with explosion energy, due to the larger available energy budget; 2) $E_{\rm th}(t_{\rm end})$ increases with shell mass, due to a larger deceleration and hence thermalization of the ejecta kinetic energy; 3) $E_{\rm th}(t_{\rm end})$ increases with shell radius, as a later onset of interaction leads to less expansion losses by $t_{\rm end}$. Figure 5.6 demonstrates that the scaling with these three parameters closely follow the analytic scalings of § 5.2. The analytics did not take into account the shell width, and Figure 5.5 shows that it is has a relatively small impact on the final thermal energy content.

The radial density and energy density distributions of our exploded models at $t_{\rm end}$ are shown in Figures 5.7 and 5.8. The density profiles show two sharp features, one at the location where the inward propagating reverse shock stalled, and one at the location of the contact discontinuity between the star and CSM. The energy density has a smoother radial distribution. Figure 5.8 shows that, even though the shell width does not impact the total thermal energy content, it does affect the radial distribution, with more extended shells leading to more central concentration of mass and energy. This will have some effect of the shape of the resulting light curve.

Fallback

For models with strong interaction, the reverse shock may reach the center of the ejecta and induce fallback onto the remnant (e.g., Chevalier 1989b). Alternatively, low explosion energies could also allow larger amounts of mass to remain bound to the remnant. It is interesting to speculate whether this fallback could provide a mechanism to explain the apparently low ^{56}Ni masses inferred for some RFSNe, as ^{56}Ni is synthesized in the innermost layers of the star. Following previous work on SN fallback (see e.g. MacFadyen et al. 2001; Zhang et al. 2008), we explore here the amount of material which may remain bound to the central remnant following the explosion.

Figure 5.9 shows the amount of fallback for models with 3 $M_\odot$ of CSM and various explosion energies. For models with $E = 1$ B the fallback mass is small ($\lesssim 0.01\,M_\odot$). This is because the reverse shock stalls before reaching the ejecta center. A CSM

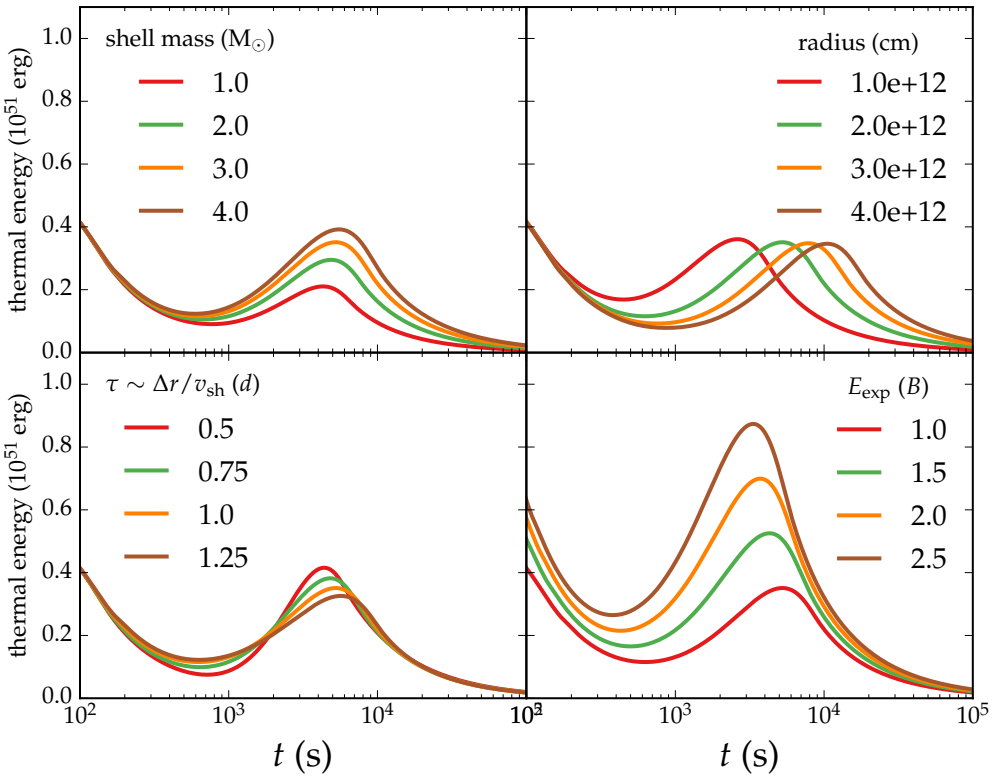

Figure 5.5: Thermal energy evolution for models with different physical parameters. The panels show the effect of varying the CSM mass (top left), CSM radius (top right), CSM thickness (bottom left, note both $r_{\rm mid}$ and τ are varied proportionally to one another to produce self-similar solutions), and the explosion energy (bottom right).

mass of $M_{\rm CSM} \gtrsim M_{\rm ej}$ is needed for the reverse shock to approach the center in a $E = 1$ B explosion (see Figure 5.7).

For low explosion energies ($E \lesssim 0.3-0.5$ B) and $M_{\rm CSM} \approx M_{\rm ej}$ the fallback mass may be significant, $\gtrsim 0.05\ M_\odot$. This is comparable to the typical mass of ^{56}Ni inferred to be ejected in core collapse SNe. Since ^{56}Ni is synthesized in the densest, innermost regions, such strong fallback could significantly reduce or eliminate entirely the radioactivity available to contribute to the light curve.

The results in Figure 5.9 are only suggestive, as the actual amount of fallback will depend on the details of the progenitor structure and explosion mechanism. Whether fallback is relevant for RFSNe is unclear. Given the scalings of Figure 5.6, a low

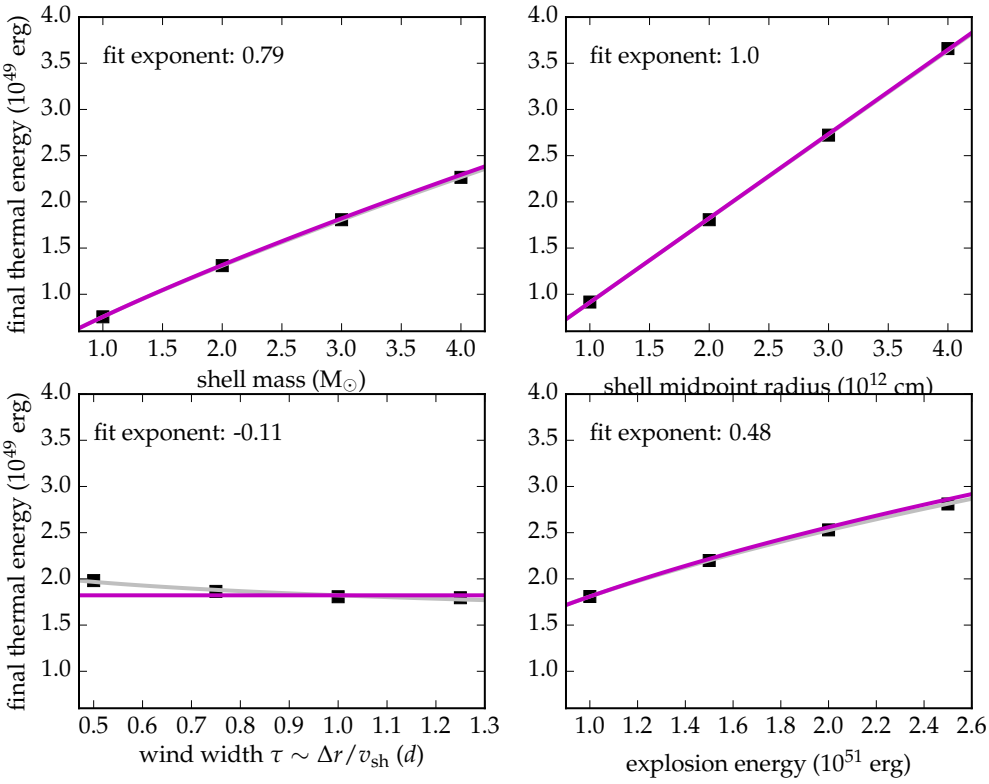

Figure 5.6: Final thermal energy at $t_{end} = 10^5$ s for each simulation presented in Figure 5.5. The power-law fits to our numerical data are listed in the figure, and solid gray lines show the fits to the data. Solid magenta lines show our analytical power laws for comparison. The fitted exponents correspond well to our analytical scalings in Equation 5.10 of §5.2.

explosion energy will lead to a dim light curve unless the progenitor star radius is very large. Alternatively, if the explosion energy is typical ($E \approx 1$ B), the CSM mass likely needs to exceed that of the ejecta. Even in cases where the fallback mass is significant, multi-dimensional effects could mix synthesized ^{56}Ni out to larger radii, allowing some radioactive material to be ejected. More detailed simulations are needed to evaluate the importance of fallback in RFSNe.

Light Curves

Nickel-Free Light Curves

Having run hydrodynamical simulations of the ejecta/CSM interaction, we post-process the results with radiation transport calculations in SEDONA. Table 5.1

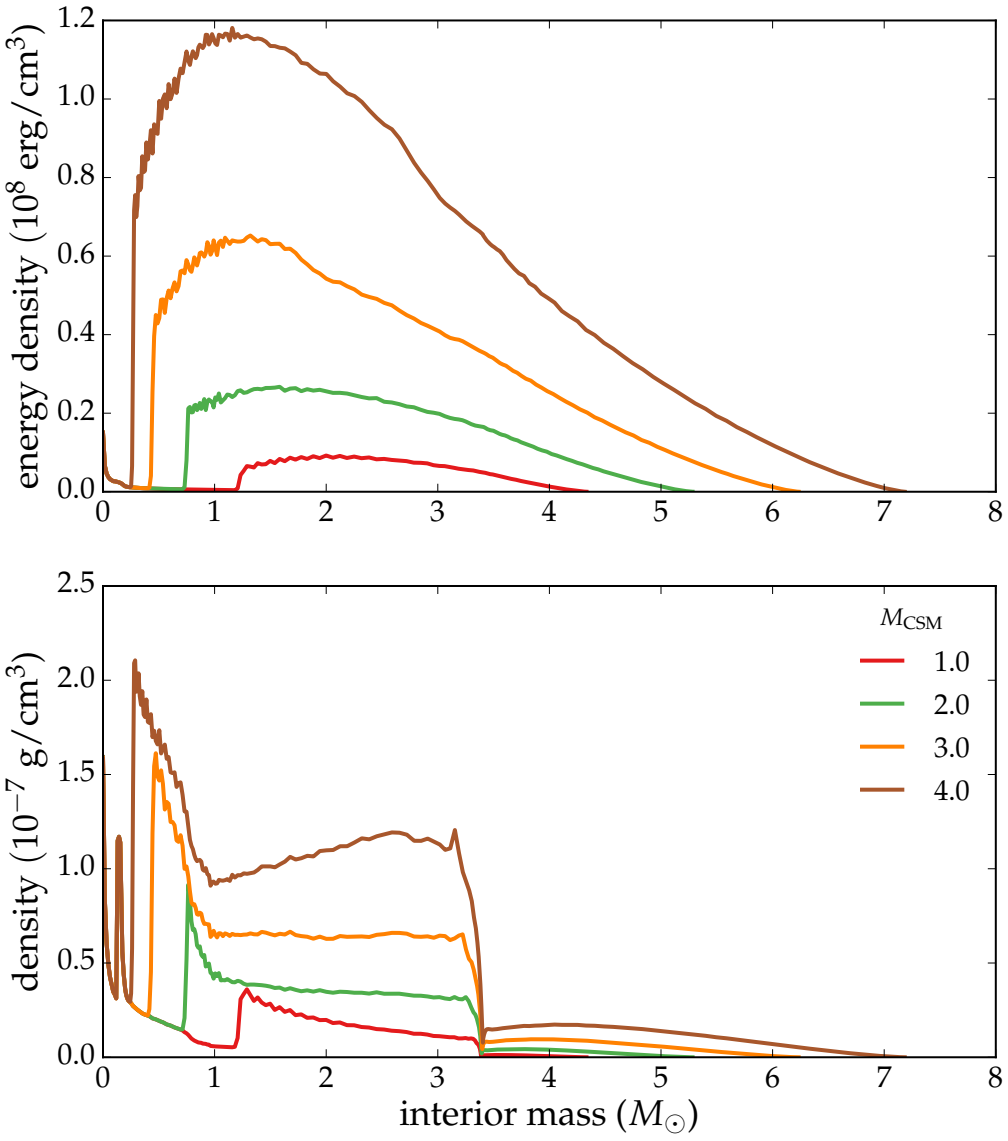

Figure 5.7: Final density and energy density profiles for the explosion of a 5 $M_\odot$ star with different CSM masses. Most of the thermal energy is contained between the reverse shock and the star/CSM contact discontinuity. The thermal energy is greater for models with larger CSM masses, and both the density and energy density are concentrated farther inward in mass coordinate.

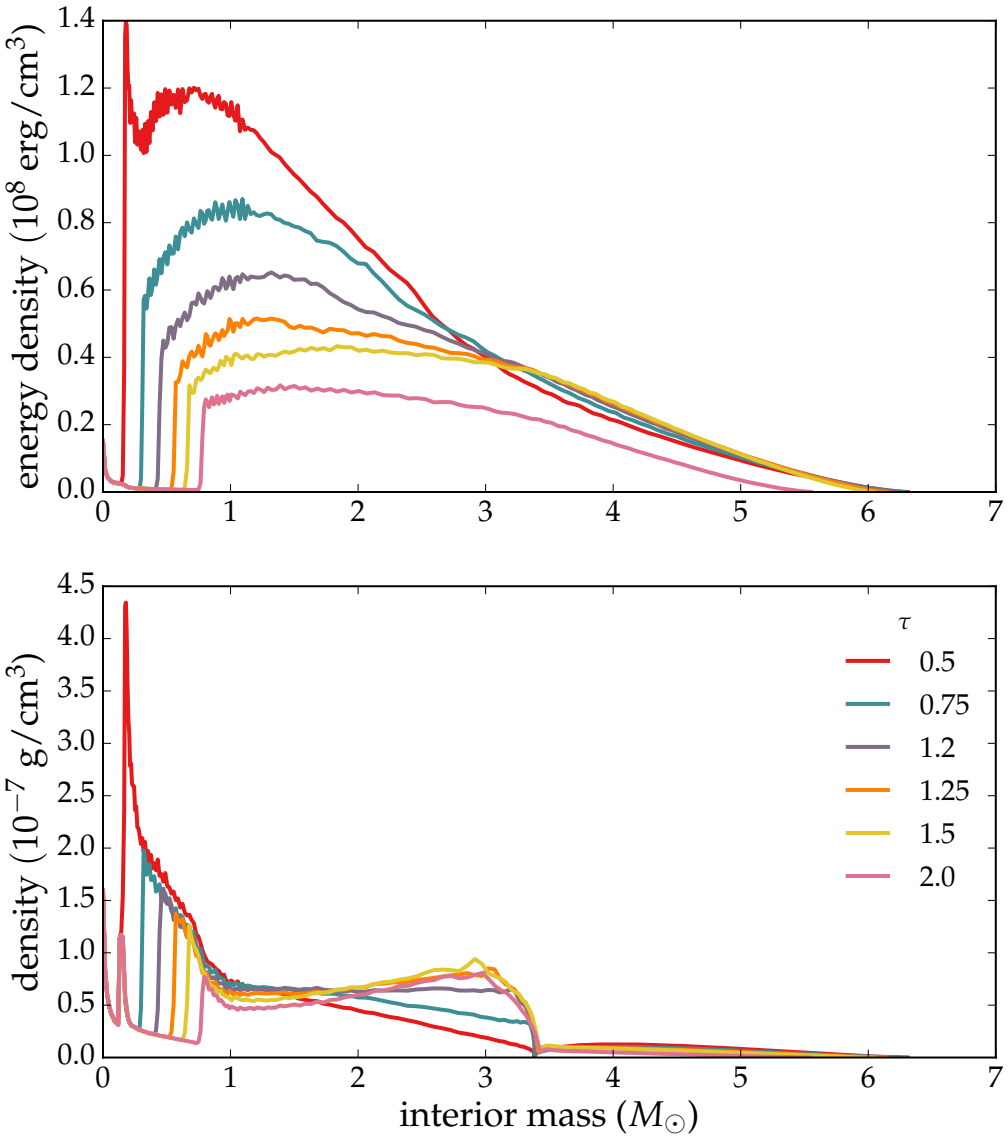

Figure 5.8: Same as Figure 5.7 but for models varying the τ parameter that sets the CSM thickness. While the CSM thickness does not greatly affect the total thermal energy, it does affect the final distribution of the thermal energy and the location of the reverse shock.

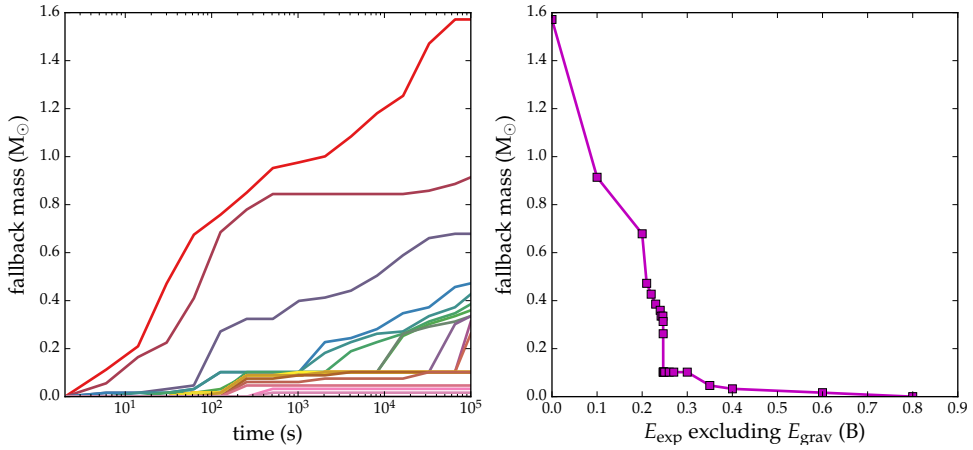

Figure 5.9: Amount of fallback in the explosion of a 5 $M_\odot$ star with 3 $M_\odot$ of CSM. Left: Cumulative fallback mass over time for models with various explosion energies. Right: Final amount of fallback as a function of explosion energy. Here explosion energy refers to the final kinetic energy of the ejecta at infinity. For lower energies ($E < 0.5$ B) the fallback mass can be significant ($\gtrsim 0.05$ $M_\odot$) and may influence the mass of radioactive ^{56}Ni ejected.

gives the parameters of the models considered, along with our calculated rise time, decline time, and peak brightness. Figure 5.10 shows a specific example light curve compared to data from SN 2010X . While the parameters ($M_{\rm shell} = 3.0$ $M_\odot$, $R_{\rm mid} = 2\times10^{12}$ cm, $\tau = 1$ day, $E_{\rm exp} = 3$ B) were not finely tuned to fit this particular object, the model reproduces the bulk properties of this supernova rather well.

We show in Figure 5.11 the variety of r-band light curves and bulk properties (peak brightness, rise time, and decline time) for our parameter survey of different CSM structures and explosion energies. Similar to the observed diversity in RFSNe shown by Drout et al. (2014), the model light curves display generally short durations but span a wide range in brightness. For the parameter range chosen, most of our models occupy the lower-luminosity ($M_r > -17$) region. However, models with higher explosion energies ($E > 1$ B) or larger radii $R_{\rm csm} \gtrsim 10^{14}$ cm, and lower ejected masses ($M \lesssim 2M_\odot$) begin to approach the luminosity and rapid timescales of the brightest RFSNe.

To explore the effect of ejecta mass in a parameterized way, we have also included in our sample a model for which the stellar density profile has been reduced by a factor of 3 and exploded into a 1 $M_\odot$ shell with 3 B. The resulting light curve is very similar to that of the original mass star exploded into a 1 $M_\odot$ shell with 6 B,

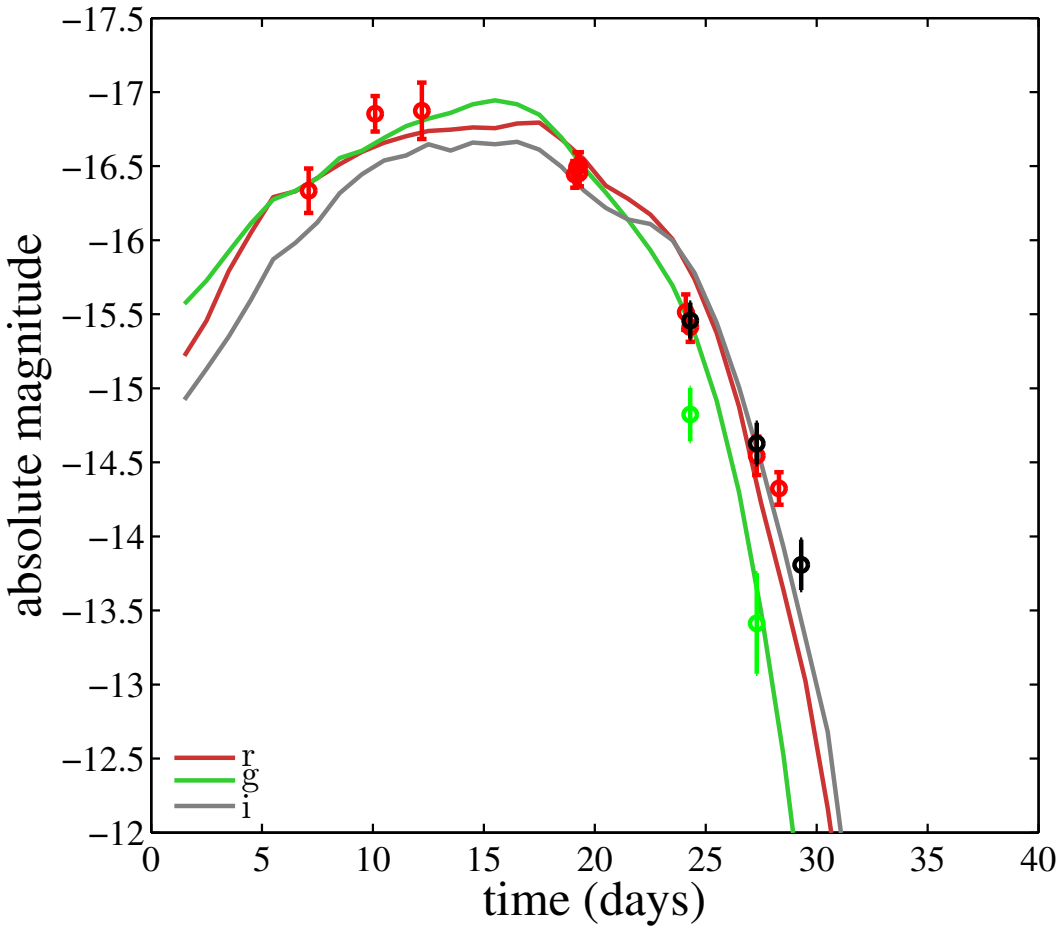

Figure 5.10: Light curve from one run plotted against the light curves for SN 2010X . The parameters used here are $E_{\rm exp} = 3\ B$, $M_{\rm shell} = 3\ {\rm M}_\odot$, $r_{\rm mid} = 2 \times 10^{12}$ cm, and $\tau = 1$ day. Because the parameters were not specifically tuned, we do not expect a perfect fit, but this comparison is to demonstrate the viability of the shock cooling model to explain main RFSNe even without extensive model tweaking. We correct the data for Galactic extinction along the line of sight to the host galaxy, NGC 1573A: $A_g = 0.483$; $A_r = 0.334$; $A_i = 0.248$. We do not assume host galaxy extinction.

suggesting that the structure of the star itself is not particularly important to the shape of the light curve but rather that the E/M ratio and CSM structure primarily determine the gross properties of the observed supernova.

While the properties of the models in our parameter survey resemble those of many observed RFSNe, the models do not well fit the light curves of some higher-luminosity events. As shown in Figure 5.11, while we can attain the necessary peak luminosities and timescales for SN 2002bj and SN 2015U , the shapes of the light curves are different; in particular, it is difficult to obtain a short enough rise time to match the observations. This indicates that the fastest rising events may not be explained by post-shock cooling. A fast (~days) rise of the light curve may be possible as a result of shock breakout in dense CSM (Chevalier & Irwin 2011). It is also possible that in some events, significant CSM interaction is ongoing throughout the light curve. The narrow He lines seen in SN 2015U (Shivvers et al. 2016) certainly suggest that there is ongoing conversion of kinetic energy to thermal energy, well past the supernova peak. Capturing these properties would require the use of radiation-hydrodynamics calculations (rather than treating the hydrodynamics and radiation transport separately in sequence).

Figures 5.12 and 5.13 show numerical versus analytical results for the same series as presented in Figure 5.6. While our analytical estimates for the total available energy were quite accurate, the light curves are somewhat more complex. Because $t_{\rm sn}$ and $L_{\rm sn}$ depend on both the sum and ratio of $M_{\rm CSM}$ and $M_{\rm ej}$ in Equations 5.13 and 5.14, they do not lend themselves to simple power laws because of the $M_{\rm diff}$ factor. As we showed subsequently in §5.2, there are some assumptions that can be used to simplify these expressions. In these figures, we have plotted the examples using $t_{\rm sn} \propto M_{\rm CSM}^{\frac{-(n-5)}{6(n-3)}+\frac{1}{2}}$ and $L_{\rm sn} \propto M_{\rm CSM}^{\frac{5(n-5)}{6(n-3)}-\frac{1}{2}}$ with $n = 6$ and $n = 8$ as examples.

We also see that, while our analytics did not consider the effects of varying the shell width τ, $L_{\rm sn}$ shows a nearly linear dependence on this parameter. This may be because a more diffuse shell produces a weaker reverse shock and more evenly distributes thermal energy in the ejecta (see Figure 5.8), allowing for a higher and earlier peak. We also see a much larger dependence on radius than expected, possibly in part due to the fact that when increasing the radius we also increased τ proportionally such that the profile of the ejecta would simply scale.

We also derive scalings from our numerical results, including for τ, which was not included in our analytical predictions. Equations for peak luminosity and timescale

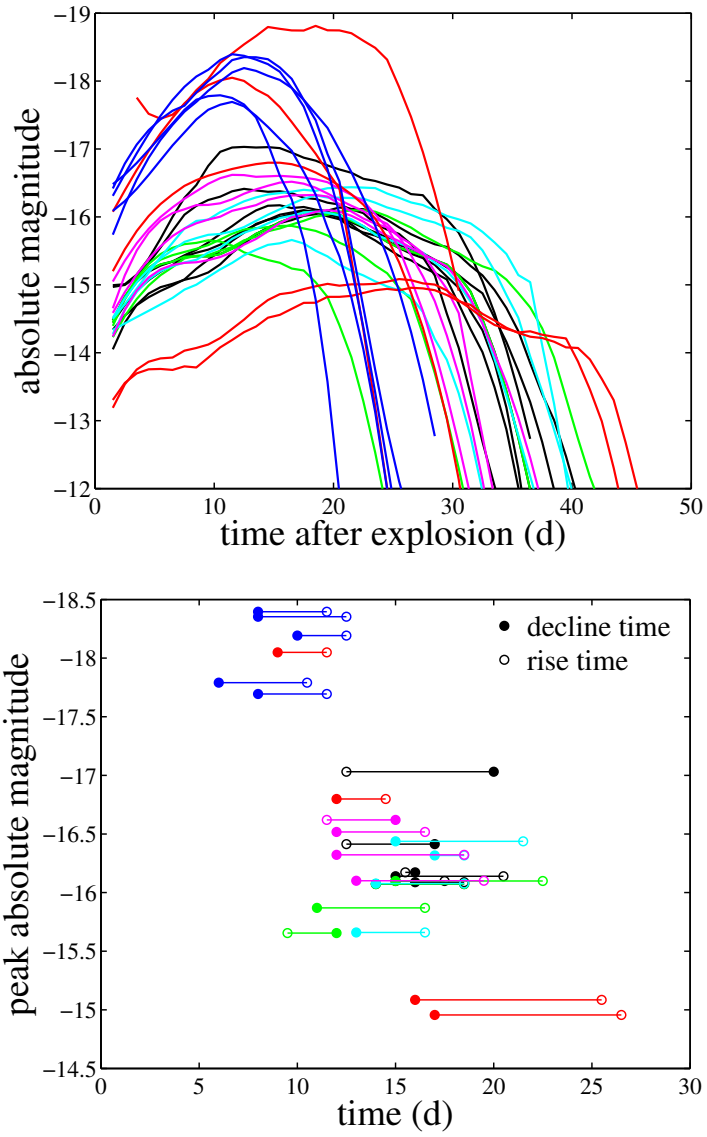

Figure 5.11: Calculated r-band optical data for many of the hydrodynamical models from Section 5.4. Top: Light curves including parameter variation in radius, explosion energy, shell mass, and τ. This plot also includes more extreme runs with large energy $E_{\rm exp} = 6\ B$ and fallback models with $E_{\rm exp} = 0.22,\ 0.25\ B$. Light curves have been run with low photon counts for speed and then smoothed using Savitzsky-Golay filtering. Bottom: Peak magnitude and timescale plots for these light curves. To the left of the plot is the rise time ($t_{\rm peak} - t_0$). To the right are decline times determined by how long it takes for the r-band light curve to decline from peak by two magnitudes. The parameters and bulk properties of the runs plotted here are shown in Table 5.1.

Table 5.1: Properties of star + shell models and their corresponding supernovae.

$M_{\rm shell}$[a]	τ[b]	$R_{\rm mid}$[c]	$E_{\rm exp}$[d]	$M_{\rm peak}$[e]	$t_{\rm decl}$[f]	$t_{\rm rise}$[g]	color[h]
3.0	0.5	2×10^{12}	1.0	-16.1391	15	20.5	black
3.0	0.75	2×10^{12}	1.0	-16.0881	16	18.5	black
3.0	1.0	2×10^{12}	1.0	-16.0729	14	18.5	black
3.0	1.25	2×10^{12}	1.0	-16.0990	15	17.5	black
3.0	1.4	2×10^{12}	1.0	-16.1721	16	15.5	black
3.0	4.0	2×10^{12}	1.0	-16.4137	17	12.5	black
3.0	10.0	2×10^{12}	1.0	-17.0311	20	12.5	black
1.0	1.0	2×10^{12}	1.0	-15.6547	12	9.5	green
2.0	1.0	2×10^{12}	1.0	-15.8692	11	16.5	green
3.0	1.0	2×10^{12}	1.0	-16.0729	14	18.5	green
4.0	1.0	2×10^{12}	1.0	-16.0987	15	22.5	green
3.0	0.5	1×10^{12}	1.0	-15.6602	13	16.5	cyan
3.0	1.0	2×10^{12}	1.0	-16.0774	14	18.5	cyan
3.0	1.5	3×10^{12}	1.0	-16.3172	17	18.5	cyan
3.0	2.0	4×10^{12}	1.0	-16.4376	15	21.5	cyan
3.0	1.0	2×10^{12}	1.0	-16.1009	13	19.5	magenta
3.0	1.0	2×10^{12}	1.5	-16.3225	12	18.5	magenta
3.0	1.0	2×10^{12}	2.0	-16.5175	12	16.5	magenta
3.0	1.0	2×10^{12}	2.5	-16.6194	15	11.5	magenta
3.0	10.0	2×10^{12}	6.0	-18.0486	9	11.5	red
3.0	1.0	2×10^{12}	0.22	-14.9561	17	26.5	red
3.0	1.0	2×10^{12}	0.25	-15.0852	16	25.5	red
3.0	1.0	2×10^{12}	3.0	-16.7979	12	14.5	red
1.0*	(wind)[i]	2×10^{14}	3.0	-18.8123	9	18.5	red
1.0	10.0	1×10^{12}	3.0	-17.6945	8	11.5	blue
1.0	10.0	1×10^{12}	6.0	-17.7910	6	10.5	blue
1.0	10.0	2×10^{12}	3.0	-18.1923	10	12.5	blue
1.0	10.0	2×10^{12}	6.0	-18.3955	8	11.5	blue
1.0[j]	10.0	2×10^{13}	3.0	-18.3533	8	12.5	blue

[a] Shell mass in $M_\odot$. [b] Effective temporal width of mass loss episode in days. [c] Effective midpoint radius of shell in cm.
[d] Explosion energy in B. [e] Peak r-band magnitude. [f] Decline time (by a factor of 1/2 in luminosity from peak) in days. [g] Rise time in days.
[h] As plotted in Figure 5.11 [i] The label (wind) signifies that in this case the CSM density profile goes as r^{-2} and is not modified by the Gaussian.
[j] Stellar model with density profile reduced by a factor of three in order to explore lower ejecta mass.

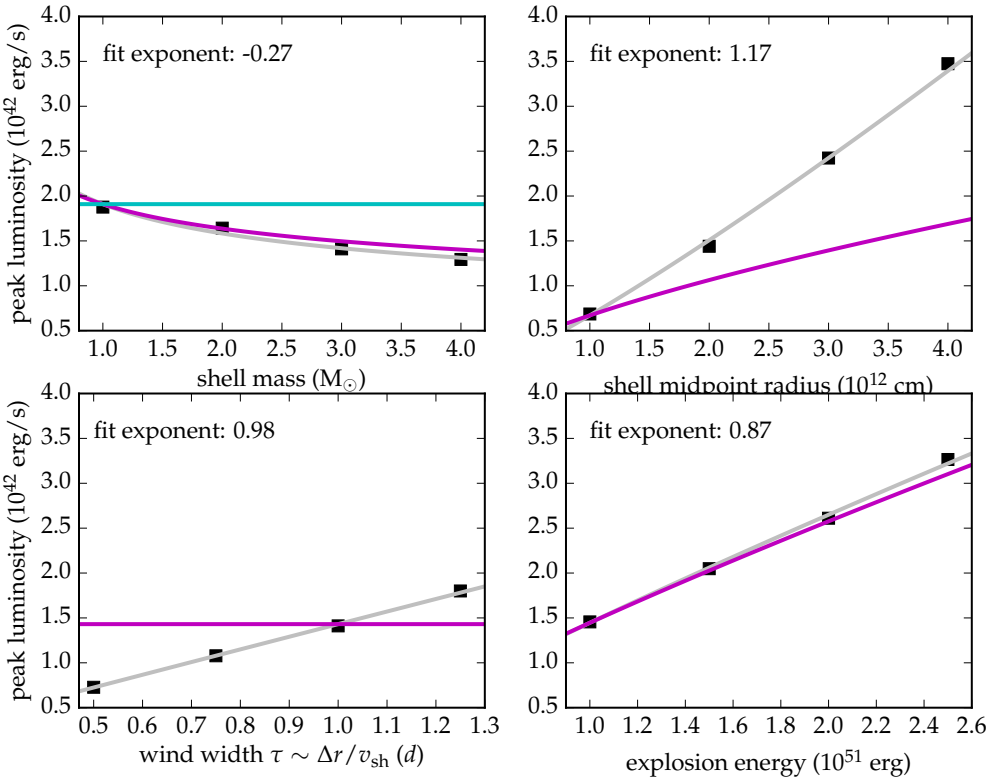

Figure 5.12: Peak luminosities for the parameter study shown in Figure 5.6. The power-law fits to our numerical data are listed in the figure, and solid gray lines show the fits to the data. Solid magenta lines show our analytical power laws from Equation 5.18 of §5.2 using $n = 6$. The cyan line in the first panel represents the same but using $n = 8$ for the mass variation. Note that there is a stronger dependence of L_{sn} on both τ and R_{CSM}, which we tentatively attribute to the different distribution of energy for different CSM structures, as shown in Figure 5.8.

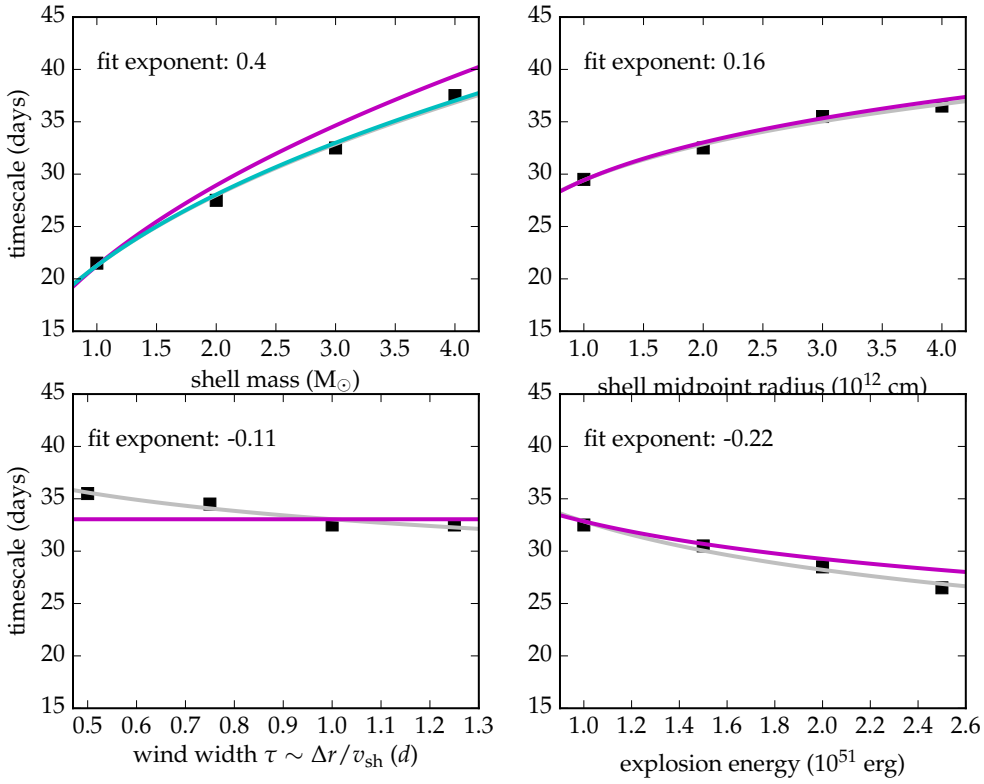

Figure 5.13: Same as Figure 5.12 but for timescales $t_{\rm sn} = t_{\rm rise} + t_{\rm decline}$. Again, gray lines show our power-law fits to the data, while magenta lines show analytic results from Equation 5.17 of §5.2. As in Figure Figure 5.12, the magenta line in the first panel uses $n = 6$, and the cyan line uses $n = 8$.

based on the fits to our numerical results are:

$$L_{\rm sn} \approx (1.3 \times 10^{42}\ {\rm erg/s})\, M_{\rm CSM}^{-0.27} R_0^{1.17} \tau^{0.98} E_{\rm exp}^{0.87}\ , \tag{5.21}$$

$$t_{\rm sn} \approx (29\ {\rm days})\, M_{\rm CSM}^{0.4} R_0^{0.16} \tau^{-0.11} E_{\rm exp}^{-0.22}\ . \tag{5.22}$$

The normalizations are obtained by taking the average value from the fits to each parameter variation and then reducing to one significant figure due to the uncertainty.

Spectra for SN 2010X

While a comprehensive study of the spectroscopic properties of our models is beyond the scope of this work, we show in Figure 5.14 example spectra of the single SN 2010X model whose light curve is shown in Figure 5.10. Figure 5.14 shows

comparisons of our calculated spectra to those obtained by Kasliwal et al. (2010) at similar days. The observed spectra have been corrected for the redshift of the host galaxy (NGC 1573A at $z = 0.015014$) and de-reddened using Galactic extinction value along the line of sight $A_V = 0.401$ but assuming no host extinction. As can be expected, the results from our model resemble those of a typical SN Ibc, although at early times they are quite blue. They compare fairly well with SN 2010X spectra, showing many of the same features but not always recovering their relative strengths. The calculated spectra are also slightly bluer across the board, which could be due to unaccounted-for host extinction that we have chosen to exclude from our corrections to the data.

Double-Peaked Light Curves

The contribution of significant emission from shock cooling does not necessarily preclude the presence of radioactive nickel in the ejecta. Models that include some radioactive ^{56}Ni can produce more complex light curves with double-peaked morphologies. Figure 5.15 shows our light curves using the parameters in Figure 5.10 ($E_{\rm exp} = 3\ B$, $M_{\rm shell} = 3\ {\rm M}_\odot$, $r_{\rm mid} = 2 \times 10^{12}$ cm, and $\tau = 1$ day) as well as 0.01, 0.05, or 0.1 $\rm M_\odot$ of ^{56}Ni concentrated in the center of the ejecta. The ^{56}Ni is distributed throughout the ejecta using the parameterized radial profile Equation 5.20 with smearing parameters $s = 10$ and 50. These light curves qualitatively resemble those of double-peaked SNe discussed in Drout et al. (2016), such as SNe 2005bf, 2008D, and 2013ge.

As expected, the additional nickel increases the peak luminosity and adds the characteristic radioactive tail. The ^{56}Ni can also produce a second peak in light curve, but the radioactive peak can blend with the shock-cooling peak for models with smeared nickel distributions. Interestingly, the model with only 0.01 $\rm M_\odot$ of nickel but smearing factor $s = 50$ produces a bright, short-lived peak that drops precipitously to a very low magnitude, which might often be below the limits of detectors, depending on the object's distance. Therefore an object with a small amount of very smeared nickel in addition to the shock cooling contribution might increase the luminosity without producing a detectable tail.

Effects of Rayleigh-Taylor Mixing

While our hydrodynamical models have been carried out in 1D, it is well known that the SN interaction is subject to the Rayleigh-Taylor instability (RTI). The sharp

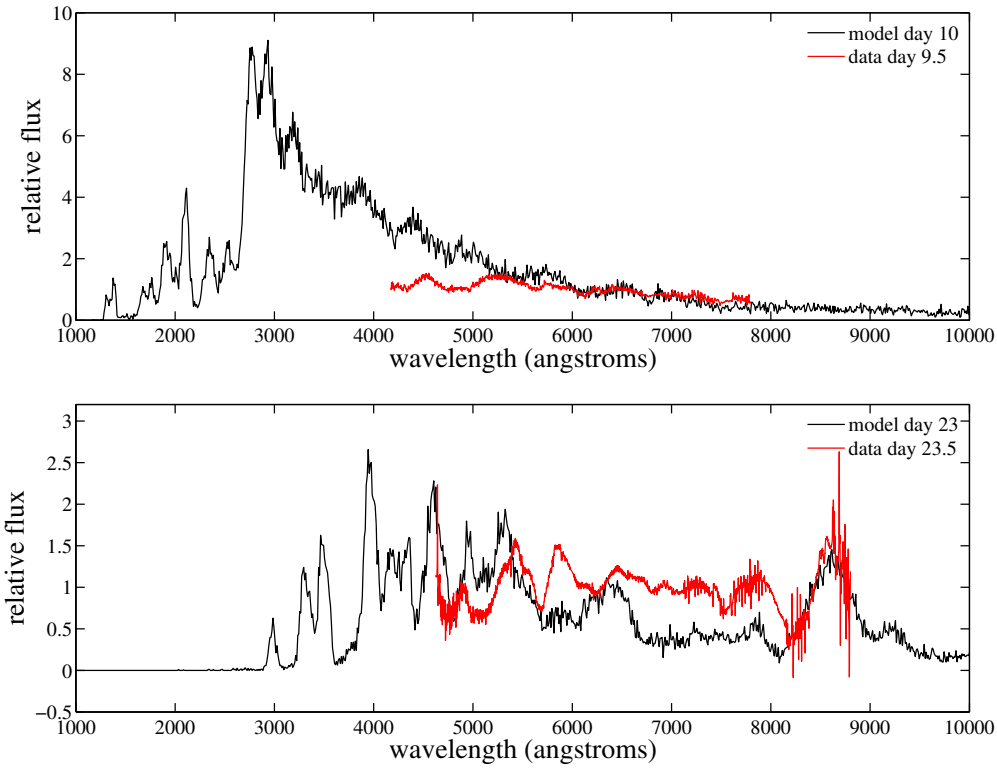

Figure 5.14: Spectra of the same model shown in Figure 5.10 at days 12 and 23 after explosion (black). We have plotted data from SN 2010X at days 9.5 and 23.5, respectively, for comparison (red), after correcting for redshift and Galactic extinction. The presumed day after explosion for the data is determined by the shift we use in matching the light curve data to our model light curves. Note that many of the same features are reproduced, but the relative strengths can differ for a variety of possible reasons, including variations in composition, temperature, and ejecta structure. Because we have not finely tuned our model to fit this object, we expect it to recover only the bulk properties of the spectra, which is typical of SNe Ibc. Our calculated spectra are also slightly bluer, which could be corrected by assuming some amount of extinction for the host galaxy.

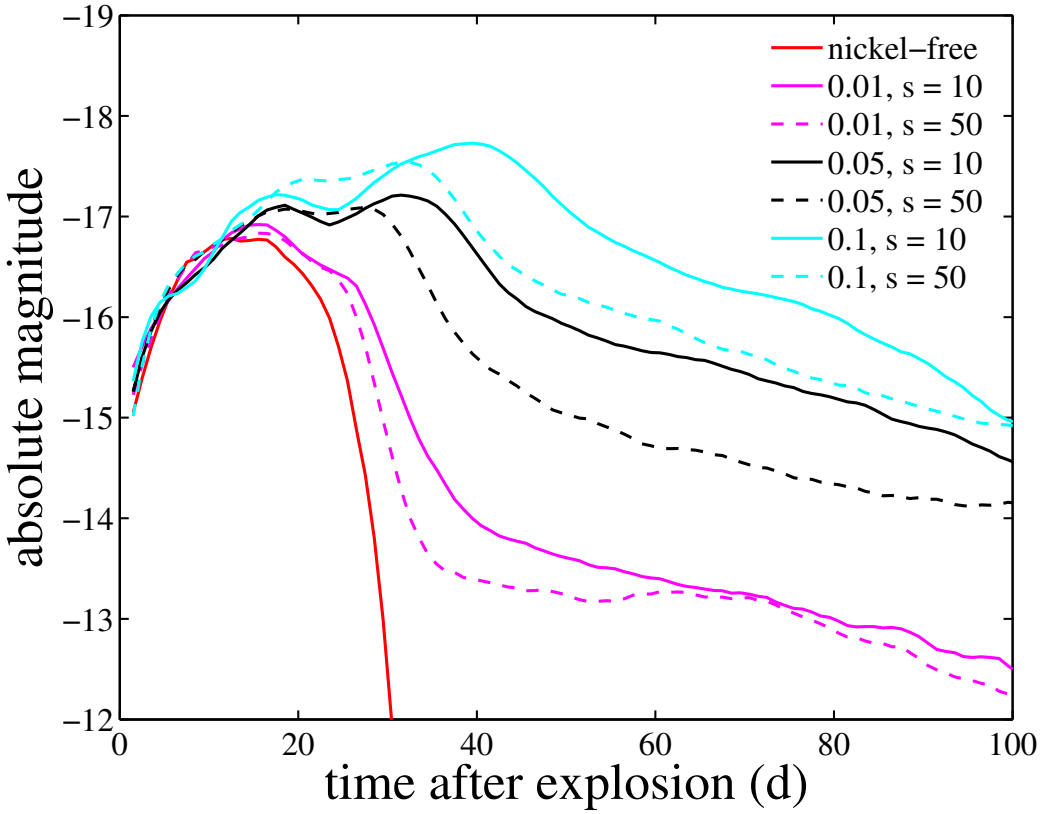

Figure 5.15: Model light curves obtained by adding ^{56}Ni to the ejecta structures for the SN 2010X fit in Figure 5.10. The Figure shows models with nickel masses of 0.01, 0.05, and 0.1 $M_\odot$; and for two levels of smearing, s =10 and 50. Less smearing (with nickel concentrated toward the center) is more likely to result in two distinct peaks.

features and spikes in the density profiles of Figures 5.7 and 5.8 can be expected to smoothed out by RT instabilities, which will also mix the ejecta and CSM. These multi-dimensional affects could in principle affect the rate at which light diffuses out of the ejecta and could affect the shape of the light curve.

To estimate the effects of the RTI on the models, we ran one of our star + CSM models using the hydrodynamics code from Duffell (2016), which includes a 1D RTI mixing prescription that has been calibrated to 3D models. In this case, we used a CSM mass of 3 $M_\odot$ and a CSM radius of 2×10^{13} cm, chosen in order approach the higher luminosities of SN 2015U and SN 2002bj . The hydrodynamics results are shown in Figure 5.16. RTI mixing almost entirely eliminates the large density spike that occurs in 1D models at the CSM/ejecta contact discontinuity. The energy

density in the RTI calculation is also somewhat higher than a model without RTI, since kinetic energy in the form of turbulence eventually cascades into lower spatial scales until it is thermalized. Rather than all the kinetic energy go into expansion and acceleration of the ejecta, some instead becomes turbulent kinetic energy and eventually thermal energy.

Figure 5.17 shows the resulting light curves from the runs with RT prescription turned both on and off. It seems, in this case, that even though the final hydrodynamics profile is dramatically different, the mixing does not affect the overall peak luminosity or timescale, although it does affect the very early behavior of the light curve. This may be due to the fact that in the RT-off case, the shock passes through, heats, and accelerates the outer layers to large radii and large velocities, so the diffusion time for the small amount of radiation in these outer layers is short; in the RT-on case, much of the shock energy is dissipated into heat before it can reach these outer layers, and outer layers are not as accelerated and therefore do not reach the low densities needed for a very short diffusion time. In both runs, the peak luminosity is similar to that of SN 2002bj , but the rise time is still too long to fit these fast-rising objects.

5.5 Discussion and Future Directions

We have shown that models of the core-collapse SN with large pre-supernova radii and lacking ^{56}Ni are a viable explanation for some H-free short-duration transients of a range of luminosities. We suggested that the large initial radius may be due to heavy mass loss just prior to the explosion, and we explored the dynamics and observable signatures of stars exploding into shells and winds. The model light curves presented here resemble those of many of the observed RFSNe, but they struggle to capture the light curve shapes for some objects with high luminosities and rapid rise times. It is likely that for brighter objects the stellar radius would be large enough that the shock has not propagated all the way through the shell by the time radiation losses become significant. Scenarios involving shock breakout in a wind may be more appropriate for these events, and this will be an area of exploration using radiation-hydrodynamical simulations in later work. We expect that the use of radiation-hydrodynamics will change calculations for larger-radius progenitor systems. In such models, radiation will begin escaping at early times when the ejecta have not yet reached homologous expansion. These radiation losses can affect the dynamics; in particular, if radiation can escape directly from the region of the shock, the shock could lose significant energy and result is less acceleration

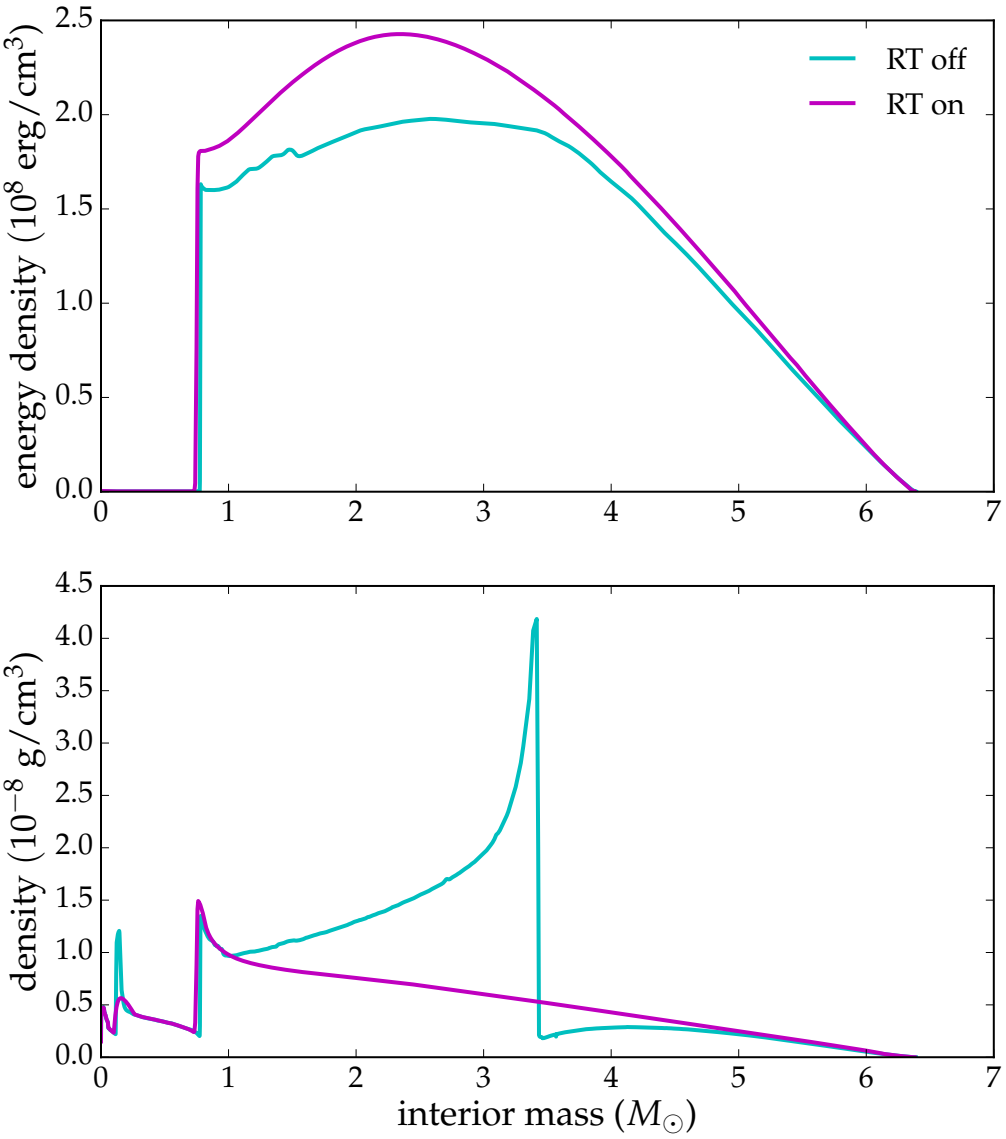

Figure 5.16: Energy density and mass density profiles from the 1D hydrodynamics code from Duffell (2016), which includes a 3D-calibrated prescription for Rayleigh-Taylor mixing. Here the forward shock is stronger than shown in previous figures because we used a large radius (2×10^{13} cm) in the hopes of capturing fast-rising, bright RFSNe. The density structure is dramatically affected by RT instabilities. Note that the run with Rayleigh-Taylor mixing on has a higher energy density; however the envelope is also not as extended as it is without mixing, since more of the outward kinetic energy is converted into turbulence.

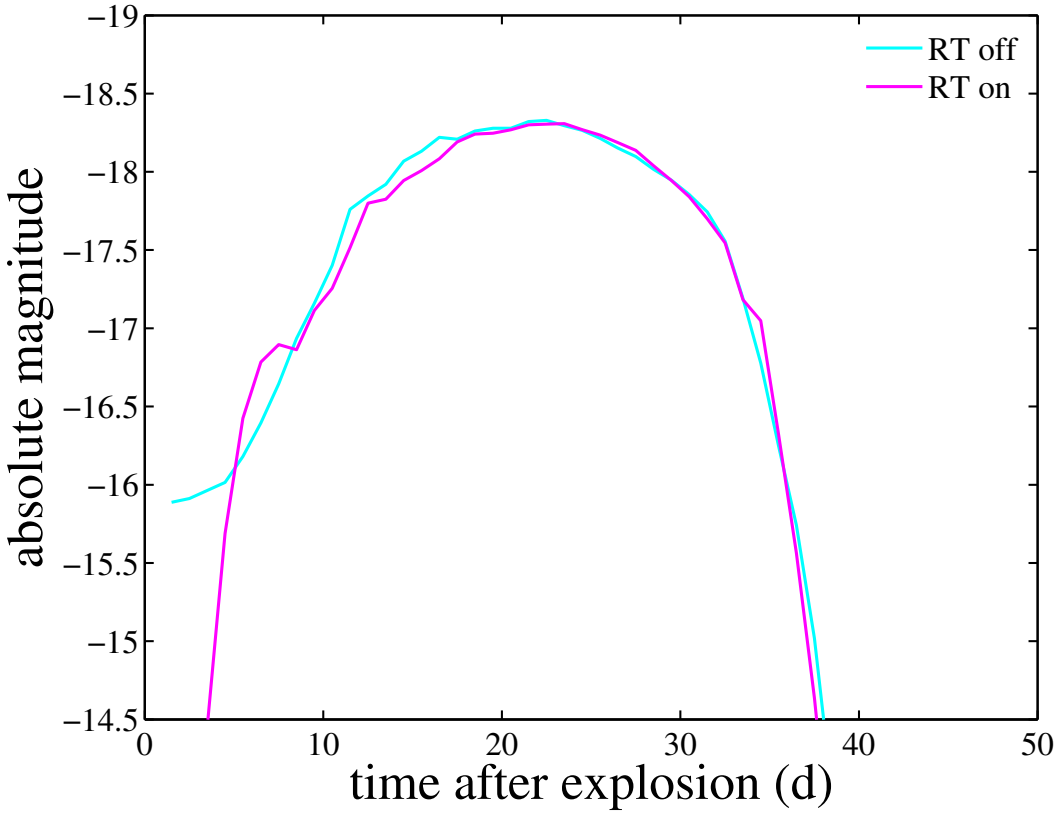

Figure 5.17: Light curves using the hydro output from our code and the code from Duffell (2016) with the Rayleigh-Taylor mixing prescription on and off. Evidently even though mixing can significantly affect the structure of the ejecta, it may not have a large effect on the bulk light curve properties.

of the outer layers. This could quantitatively change the peak and timescale of the light curve as well as the velocities of spectroscopic lines.

Two outstanding questions remain for the presented model for RFSNe. One is the reason for the apparent low ejection of ^{56}Ni. Observations and parameterized 1D models of massive star explosions suggest that $\sim$ 0.05 $M_\odot$ of ^{56}Ni should be synthesized in typical core collapse events. In §5.4, we studied whether RFSNe may enhanced fallback, which could rob the ejecta of radioactivity. In stars surrounded by a dense CSM, the interaction of the ejecta with the CSM will produce a reverse shock which can decelerate and push material back onto the central remnant. While this suggests an intriguing connection between nickel-free explosions and progenitors with extended envelopes or shells, achieving significant fallback through the reverse shock would require that the mass of the CSM more than exceed that of the ejecta.

Alternatively, independent of the presence of the CSM, fallback can occur if the explosion energy is somewhat less than the canonical 1 B. We showed that for certain stellar structures, the explosion energy can be tuned to allow ~ 0.1 $M_\odot$ of of fallback while still unbinding the rest of the star and accelerating outer layers to high velocities. Light curves calculated for these examples are relatively dim and long-lived, so obtaining RFSNe with fallback may require lower-mass, higher-radius pre-SN configurations. Our 1D studies, however, are merely a proof of concept for the viability of removing ^{56}Ni by fallback. More detailed calculations would consider how the interior stellar structure may have been modified by the pre-supernova mass-loss, as well as the influence on fallback mass of both multi-dimensional dynamics and the particular explosion mechanism.

The second outstanding question is how H-stripped stars might be able to obtain extended envelopes or mass shell ejections that produce an adequately bright shock cooling light curve. While several theoretical studies have the laid the groundwork for understanding that late burning phases could unbind or extend much of the stellar envelope, more detailed stellar evolution calculations are needed to understand if these instabilities can occur in the final few days of a stripped envelope stars life.

Conclusions

In this chapter, we have explored the viability of hydrogen-stripped core-collapse supernova models using no radioactive nickel and extended helium envelopes to explain the enigmatic rapidly fading supernovae discovered in the last few years. Using 1D stellar evolution, hydrodynamics, and radiation transport codes in sequence, we have shown that such models reproduce the bulk properties of these events. We also compare our numerical results to analytical scalings predicted for the light curve properties. Further investigation using radiation-hydrodynamics codes would help understand the cases with more extended envelopes, as it is expected that sometimes the ejecta will still be dynamically interacting with the CSM even while radiation losses occur. Additional insight into possible mechanisms for both attaining such extended envelopes and failing to produce nickel in the ejecta are also necessary to validate this explanation.

References

Arcavi, I., Wolf, W. M., Howell, D. A., et al., 2016, ApJ, 819, 35, 35

Bildsten, L., Shen, K. J., Weinberg, N. N., & Nelemans, G., 2007, ApJL, 662, L95

Chevalier, R. A., 1989a, ApJ, 346, 847

—, 1989b, ApJ, 346, 847

—, 1992, ApJ, 394, 599

—, 2012, ApJL, 752, L2, L2

Chevalier, R. A., & Irwin, C. M., 2011, ApJL, 729, L6, L6

Crowther, P. A., 2007, ARA&A, 45, 177

Dessart, L., Hillier, D. J., Livne, E., et al., 2011, MNRAS, 414, 2985

Drout, M. R., Chornock, R., Soderberg, A. M., et al., 2014, ApJ, 794, 23, 23

Drout, M. R., Milisavljevic, D., Parrent, J., et al., 2016, ApJ, 821, 57, 57

Duffell, P. C., 2016, ApJ, 821, 76, 76

Harris, C. E., Nugent, P. E., & Kasen, D. N., 2016, ApJ, 823, 100, 100

Kasen, D., Thomas, R. C., & Nugent, P., 2006, ApJ, 651, 366

Kasen, D., & Woosley, S. E., 2009, ApJ, 703, 2205

Kasliwal, M. M., Kulkarni, S. R., Gal-Yam, A., et al., 2010, ApJL, 723, L98

Kleiser, I. K. W., & Kasen, D., 2014, MNRAS, 438, 318

MacFadyen, A. I., Woosley, S. E., & Heger, A., 2001, ApJ, 550, 410

Moriya, T., Tominaga, N., Tanaka, M., et al., 2010, ApJ, 719, 1445

Pastorello, A., Tartaglia, L., Elias-Rosa, N., et al., 2015, MNRAS, 454, 4293

Pastorello, A., Wang, X.-F., Ciabattari, F., et al., 2016, MNRAS, 456, 853

Popov, D. V., 1993, ApJ, 414, 712

Poznanski, D., Chornock, R., Nugent, P. E., et al., 2010, Science, 327, 58

Quataert, E., & Shiode, J., 2012, MNRAS, 423, L92

Sana, H., de Mink, S. E., de Koter, A., et al., 2012, Science, 337, 444

Shen, K. J., Kasen, D., Weinberg, N. N., Bildsten, L., & Scannapieco, E., 2010, ApJ, 715, 767

Shivvers, I., Zheng, W. K., Mauerhan, J., et al., 2016, MNRAS, 461, 3057

Smith, N., 2016, ArXiv e-prints

Smith, N., Li, W., Filippenko, A. V., & Chornock, R., 2011, MNRAS, 412, 1522

Tauris, T. M., Langer, N., & Podsiadlowski, P., 2015, MNRAS, 451, 2123

Yoon, S.-C., Woosley, S. E., & Langer, N., 2010, ApJ, 725, 940

Zhang, W., Woosley, S. E., & Heger, A., 2008, ApJ, 679, 639-654, 639

Chapter 6

HELIUM GIANT STARS AS PROGENITORS OF RAPIDLY FADING TYPE IBC SUPERNOVAE

ABSTRACT

Type I rapidly fading supernovae (RFSNe) appear to originate from hydrogen-free stars with large radii that produce predominantly shock-cooling light curves, in contrast with more typical ^{56}Ni-rich SNe Ibc. However, it remains to be determined what types of stars would produce bright shock-cooling light curves without significant contribution from radioactive nickel. Bare helium stars in the mass range $\sim 2 - 4$ $M_\odot$ are known to hydrostatically develop radii as large as 100 $R_\odot$ or more due to strong He and C shell burning outside of a core with a sharp density gradient. We produce several such stellar models and demonstrate that, when exploded, these helium giants can naturally produce RFSN light curves. Since many prototypical SNe Ibc should come from large-radius stars in this mass range as well, we predict that these RFSNe may be distinct from SNe Ibc solely due to the absence of substantial ^{56}Ni.

6.1 Introduction

There has been some difficulty in characterizing the stars that give rise to hydrogen-poor rapidly fading supernovae (RFSNe) discovered in recent years. Initially their short light curve rise and fall led to the conclusion that they must be very low-mass, perhaps non-terminal, ejections (Kasliwal et al. 2010). However, radiation transport calculations in Chapter 4 (Kleiser & Kasen 2014) suggest that some of these objects require relatively large ($\gtrsim 0.3$ $M_\odot$) ejecta masses, implying that ^{56}Ni is not the dominant power source, since large ejecta masses with significant nickel content will produce a long-lasting light curve. Observational evidence from more recent RFSNe presented by Drout et al. (2014) and Shivvers et al. (2016) also point toward scenarios in which these stars explode inside extended envelopes or winds, suggesting that shock-deposited energy, rather than radioactive nickel, is the primary source of power for the light curve.

The question of why RFSNe would fail to eject nickel is still unanswered. Perhaps a large CSM-to-ejecta mass ratio could more effectively push the innermost material to fall back onto the remnant through the reverse shock that forms once the ejecta and CSM collide (Chevalier 1989). Alternatively, as shown previously (MacFadyen et al. 2001), low explosion energies ($\sim$ 0.1 B) could allow material to fall back, stifling the radioactive material and allowing only shock energy to power the light curve. Another possibility is that low shock temperatures may result in very little nickel production in the first place.

There are several possible mechanisms for developing an extended envelope around a hydrogen-free star toward the end of its life. A large effective radius (tens to hundreds of $R_\odot$) could ensue from dynamical ejection of material in the last few days of the star's life or from heating and expansion of the envelope. One promising avenue for bringing significant mass out to large radii prior to explosion is the mechanism described by Quataert & Shiode (2012) in which instabilities in core oxygen burning produce g-modes that propagate as p-modes through the envelope. Large, thick envelopes could also be the result of common envelope evolution, as discussed by Chevalier (2012) in the case of SNe IIn. This possibility was invoked speculatively for RFSNe in Chapters 4 and 5 (Kleiser & Kasen 2014; Kleiser et al. 2018).

Here we entertain another possibility, which is more naturally produced in simple stellar evolution calculations. Extended helium red giant stars have been shown to arise from certain binary evolution scenarios and can explode as SNe Ibc (Paczyński

1971; Savonije & Takens 1976; Nomoto 1984; Habets 1986a; Yoon et al. 2010; Woosley et al. 1995; Dessart et al. 2018; Yoon et al. 2012; Podsiadlowski et al. 1992; Yoon 2015; Eldridge et al. 2015; Yoon et al. 2017; Divine 1965). Upsilon sagittari (Dudley & Jeffery 1990; Koubský et al. 2006) may be an example of such a moderately inflated He star in the midst of case BB mass transfer. If these stars explode, even with a small amount of energy, their light curves could be very bright because of the very extended radius and moderate envelope mass while producing very little ^{56}Ni.

These helium stars, typically in the range of 2-4 $M_\odot$ after stripping, are therefore appealing candidates for RFSNe; they naturally develop very extended radii ($\gtrsim$ 100 $R_\odot$), and some of them are expected to result in electron-capture SNe (ECSNe) and low-mass iron core-collapse SNe (CCSNe), which should produce very small amounts of ^{56}Ni without the need for fallback of material onto the remnant (Radice et al. 2017; Müller et al. 2017; Mayle & Wilson 1988; Sukhbold et al. 2016). In this paper, we explore this possibility by running numerical simulations of the evolution of these stars, their explosions, and resulting light curves and spectra.

6.2 Methods

Using MESA version 10000, we model helium stars in the 2-4 $M_\odot$ mass range using a constant mass loss rate of 10^{-3} $M_\odot$/yr after the star has left the Main Sequence and expanded such that its surface temperature has dropped below $\sim$ 5000 K. This threshold is meant to indicate when the star's radius has likely increased enough for Roche lobe overflow. Once the H envelope has been removed, the artificial mass loss is shut off. The bare He core is then allowed to evolve until the simulation is stopped. We use the default settings for massive stars in MESA, including a "Dutch" hot wind scheme with scaling factor of 0.8 (Glebbeek et al. 2009). We use Type 2 opacities and assume solar abundances at the beginning of the simulation.

We use the final progenitor star model as the input for our 1D hydrodynamics code and run a shock through it after removing the innermost 1.4 $M_\odot$, assuming this forms the remnant. The explosion energy is chosen by hand and deposited as a thermal bomb by artificially increasing the thermal energy of the innermost few zones. The hydrodynamics code is not coupled to radiation but uses a $\gamma = 4/3$ equation of state.

We feed the output profile into a separate radiation transport code, SEDONA (Kasen et al. 2006), once the ejecta are roughly free-streaming, as described in Chapter 5 (Kleiser et al. 2018). The implicit assumption is that the ejecta will expand

adiabatically and radiation will be trapped until it is homologous. This may not be the case for all objects, e.g. those in which radiation begins escaping before the shock has traversed the entire stellar envelope and interaction is still occurring while the supernova can be observed optically. However, this assumption should be appropriate for many objects, particularly those from intermediate-radius stars. Even in cases where radiation hydrodynamics would be ideal, our results should provide informative rough peak luminosities and decline timescales; the behavior of the rise will not be adequately captured. Therefore, with this simplification, we use SEDONA to calculate time-dependent light curves and spectra for our ejecta profiles beginning about a day after explosion. In some of our light curve calculations, we add ^{56}Ni that has essentially a smoothed step-function profile, as described in Chapter 5 (Kleiser et al. 2018).

6.3 Results

We have produced stellar models with varying zero-age Main Sequence mass $M_{\rm ZAMS}$ between 12 and 18 $M_\odot$ such that their bare helium cores lie in the 2-4 $M_\odot$ range once the hydrogen envelope is removed. For the lower-mass models, the calculation slows dramatically after oxygen core formation due to the overlap of convective regions with thin burning shells. Since the envelope of the star is already quite extended by this time, we stop all models once the radius has settled into a relatively stable state. In models we allowed to run longer, the radius tended to remain constant after this point or increase steadily, but here we show only the evolution up until just after the radius settles following oxygen core formation. The more massive stars are able to evolve further, and we stop them at the point of off-center neon ignition. These stars expand in radius somewhat, although not as much as their lower-mass counterparts.

We show Kippenhahn diagrams of one low-mass and one high-mass star in Figure 6.1. Helium shell burning is responsible for the initial expansion of the radius during core carbon burning. As the carbon in the core is exhausted, an oxygen core begins to form and carbon shell burning starts. In the case of a low-mass star, a convective layer develops at the surface and extends inward, which helps inflate the star dramatically. Once the convective envelope penetrates down to the He and C shell burning regions, which are now very narrow and nearly on top of one another, the envelope enters a tumultuous phase and the radius is highly variable before settling into a slower and more steady growth. The differences in behavior between the two types of models is consistent with previous findings (e.g. Habets 1986b; Habets 1986a; Yoon et al. 2010).

The higher-mass stars, by contrast, do not develop a surface convective zone, and the He and C shell burning layers remain separate. Instead, helium shell burning creates a convective shell, but it does not lead to the dramatic expansion seen in the low-mass stars. We can also see that core burning continues in the higher-mass star, whereas the lower-mass star develops a degenerate core.

Figure 6.2 shows the photospheric radius as a function of carbon core mass near the end of the star's evolution. The lower-mass stars expand dramatically and have some rapid variability before they settle into their final radii. Meanwhile, their higher-mass counterparts expand steadily up to the point of off-center neon ignition, but they only grow to a few solar radii.

We show the final stellar density profiles of all models in Figure 6.3. The models with very extended radii show, as discussed in Habets (1986a), a very steep density gradient outside the core and low-density envelope. Larger-mass models do not feature this density gradient and have a more even distribution of mass.

When the stellar models are exploded, shock heating of the envelope converts some of the kinetic energy back into thermal energy. This behavior was explored for toy helium shells added to smaller-radius stars in Kleiser et al. (2018) but is also well known for giant stars with extended envelopes (see e.g. Popov 1993; Woosley et al. 1995; Kasen & Woosley 2009). Even for lower-energy (0.1 B) explosions, if the radius is large, then the final thermal energy at $t = 10^5$ s can still be significant. In Figure 6.4, we show light curves from all of our exploded models, some of which are qualitatively similar to RFSNe. While rise times are long compared to known objects, peak luminosities and timescales are similar. Low-mass models with large radii produce bright supernovae with relatively short rise times and very rapid decay times. More massive stars with smaller radii produce dim, very short light curves that would be difficult to detect without nickel. The low-mass models we exploded with 0.1 B are moderately bright and more plateau-like than typical RFSNe. Dessart et al. (2018) also show a shock cooling light curve from a moderately extended helium giant, but it is relatively dim and very short-lived, and they propose this as an early component of SN Ibc light curves rather than as an explanation for RFSN light curves.

Using a similar ^{56}Ni abundance profile to the ones explored in Kleiser et al. (2018), we add various amounts of mixed nickel to our 15 $M_\odot$ model exploded with 1 B, shown in Figure 6.4. If the nickel is more radially mixed (i.e. not centrally concentrated), the peak blends with the shock cooling peak. A radioactive tail is

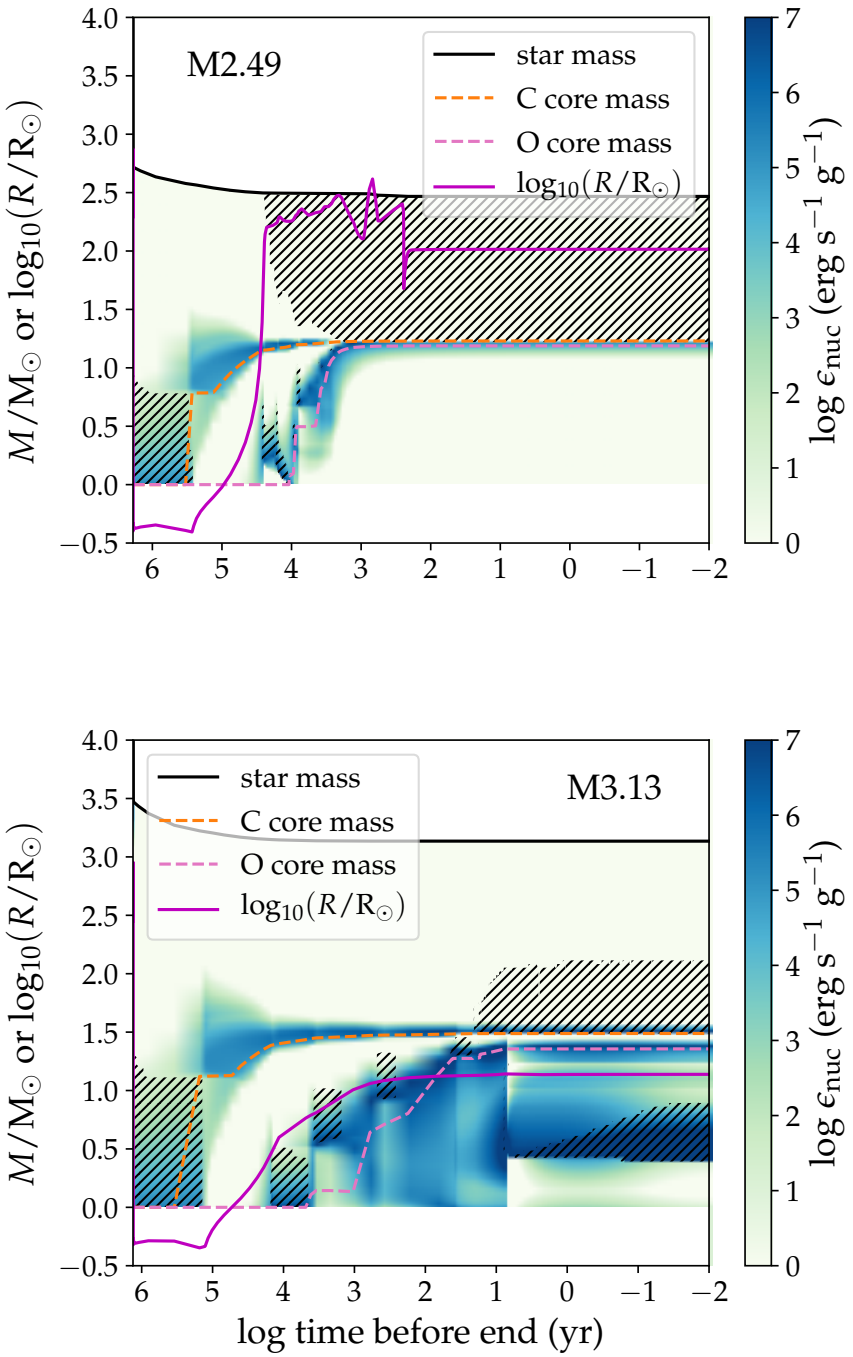

Figure 6.1: Kippenhahn diagrams for a low-mass model (2.49 $M_\odot$ at the end of artificial mass loss, $M_{\rm ZAMS}$ = 14 $M_\odot$) and high-mass model (3.13 $M_\odot$, $M_{\rm ZAMS}$ = 16 $M_\odot$). The radius over time is overlain as well, and hatches indicate convective regions. For both stars, the radius expands when the carbon core forms and helium shell burning begins. The radius of the lower-mass star grows dramatically as a convective layer forms at the surface and deepens throughout the envelope, eventually reaching the He and C shell burning regions, which have grown very close to one another. This dramatic expansion does not occur for the higher-mass star, although the evolution and final structure also will depend on the size of the Roche lobe at this point.

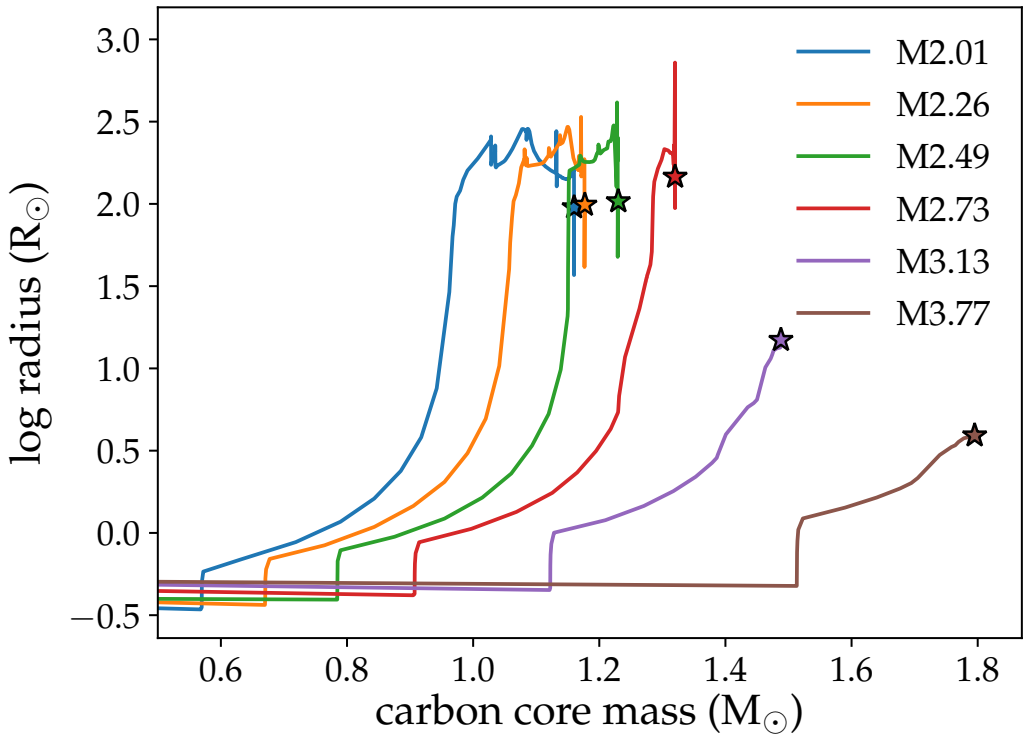

Figure 6.2: Radii as a function of carbon core mass for all stellar models. The radius, which dropped significantly at the onset of mass loss (not shown in this plot), increases dramatically as shell burning heats the envelope.

also present, but most of the peak luminosity comes from shock cooling. In a scenario like this, in which an extended helium star explodes with a small amount of highly mixed nickel, it may be difficult to distinguish the light curves from those of a regular SN Ibc that is dominantly nickel-powered.

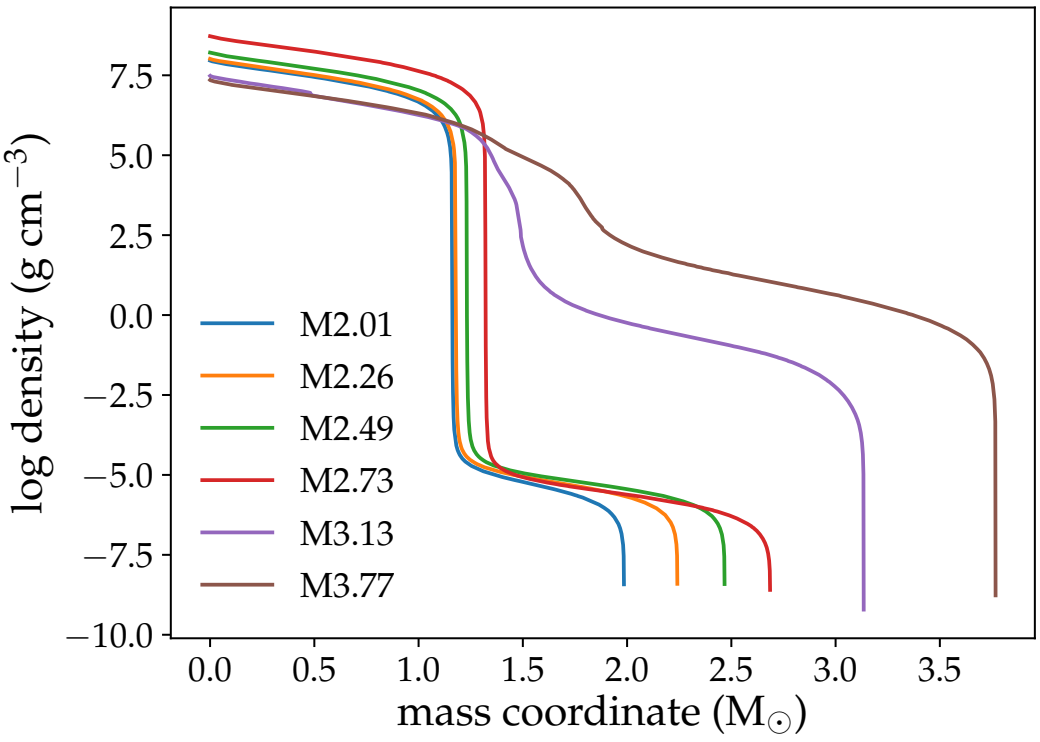

Figure 6.3: Stellar density profiles for final stellar models. The lower-mass stars have steeper density gradients outside their degenerate cores, causing their envelopes to expand to large radii due to helium shell burning. Meanwhile, higher-mass stars have much more even density distributions and much less steep gradients outside the core.

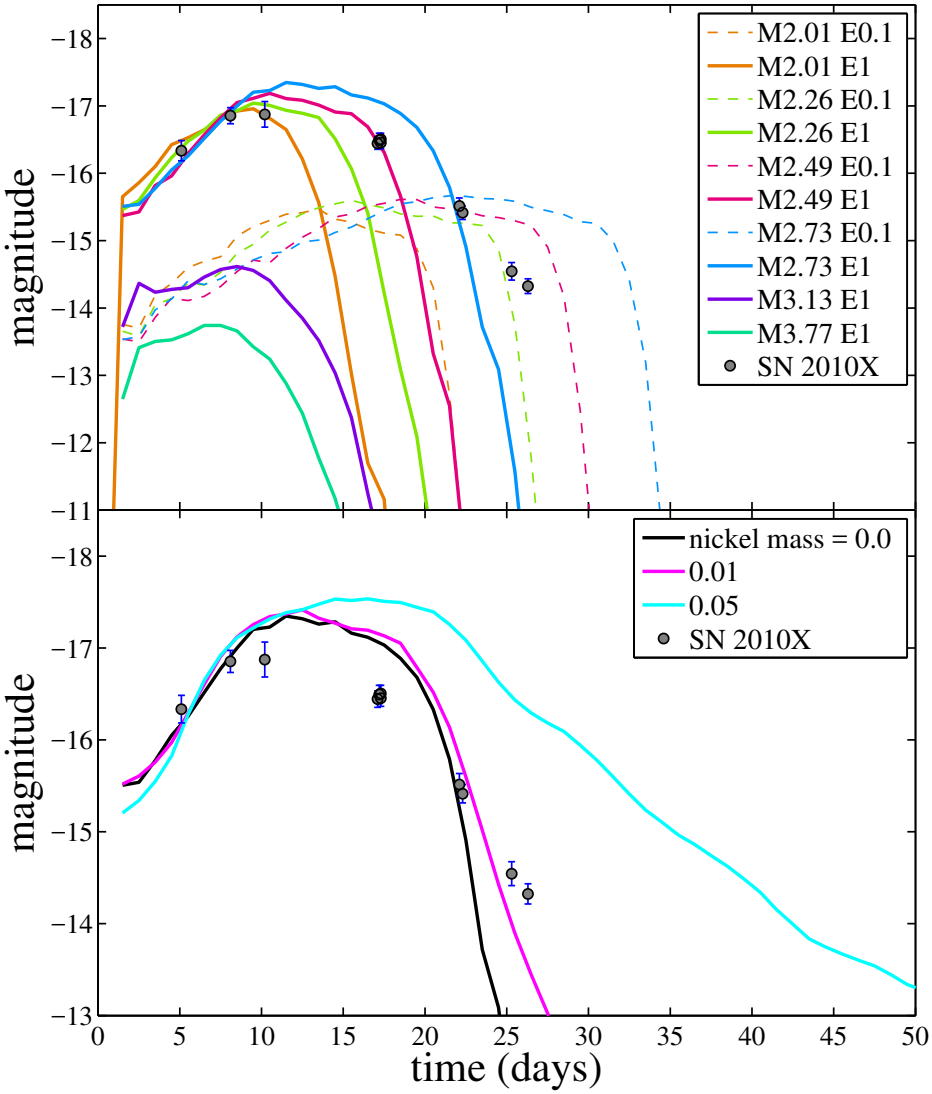

Figure 6.4: Top: Light curves (SDSS r-band) for all models. Light curves in the g and i bands track the r band closely in all cases. The peak luminosities and timescales are similar to many known RFSNe, although it is difficult to capture the rapid rise times while maintaining a slow enough decline time, as seen by comparison to SN 2010X . Lower-energy explosions rise more slowly, are slightly more plateau-like, and drop off rapidly. The explosions of low-radius, high-mass helium stars are faint without nickel. Bottom: SDSS r-band light curves calculated using the M2.73 E1 explosion model with various amounts of mixed ^{56}Ni using the formula in Chapter 5 (Kleiser et al. 2018) with the transition from nickel-rich to nickel-poor ejecta spanning $\sim$ 50 out of 200 zones. A small amount of ^{56}Ni can produce a tail while most of the peak luminosity still comes from shock cooling.

Table 6.1: Stellar and supernova properties.

$M_{\rm ZAMS}$ [a]	$M_{\rm ML}$ [b]	$M_{\rm final}$ [c]	$M_{\rm ccore}$ [d]	$R_{\rm ZAMS}$ [e]	$R_{\rm ML}$ [f]	$R_{\rm final}$ [g]	$E_{\rm th}$ [h]	$m_{r,\rm SN}$ [i]	$t_{\rm SN}$ [j]
12.0	2.18	2.01	1.08	9.59	0.352	95.2	2.54e+49	-16.96	13
13.0	2.46	2.26	1.15	10.0	0.383	98.7	3.11e+49	-17.04	16
14.0	2.72	2.49	1.22	10.4	0.402	104	3.60e+49	-17.19	18
15.0	2.99	2.73	1.31	11.2	0.408	146	5.13e+49	-17.35	21
16.0	3.47	3.13	1.48	12.0	0.473	14.9	1.17e+48	-14.62	14
18.0	4.24	3.77	1.79	12.2	0.548	3.91	4.11e+47	-13.74	13

[a] Initial or zero-age Main Sequence (ZAMS) mass in $M_\odot$. [b] Mass of bare helium core at end of artificial mass loss. [c] Mass of bare helium core at end of calculation. [d] Carbon core mass at end of calculation. [e] Radius (photospheric) on the Main Sequence in $R_\odot$. [f] Radius at end of artificial mass loss. [g] Final radius at end of calculation. [h] Thermal energy after the star is exploded with 1 B (erg). [i] Supernova *r*-band peak absolute magnitude). [j] Timescale of the supernova (days), from explosion until the r-band luminosity declines by a factor of 2 from peak.

6.4 Discussion and Conclusions

We have presented models of bare helium cores from the lower-mass end of massive stars that expand to very large radii toward the end of their lives. This expansion is due to intense shell burning when the core contracts, similar to the mechanism for envelope expansion in hydrogen-rich red giant stars (Habets 1986b; Habets 1986a; Yoon et al. 2010). The greatest expansion occurs for stars with cores that become very compact with a sharp density gradient above the core during carbon shell burning. The helium stars in these mass ranges would probably end their lives as either iron core-collapse or electron-capture SNe.

Even without production of radioactive nickel, explosions of stars with such extended radii can produce bright transients, and they qualitatively reproduce the features of some RFSNe discovered in recent years. We have found that lower explosion energies, which may be more relevant for electron-capture SNe, can still yield transients bright enough to detect. He cores from 16 $M_{\odot}$ stars and above do not develop large radii and would be very difficult to observe without the presence of nickel.

There are several possible explanations for the dearth of nickel available in the ejecta. In previous work (Kleiser et al. 2018), we considered the fallback of some of the innermost material onto the remnant (MacFadyen et al. 2001; Moriya et al. 2018). This scenario is unlikely for the helium giants presented here because they have steep density gradients outside their cores and low compactness (O'Connor & Ott 2011; Sukhbold et al. 2016), which more readily allow for neutrino-driven explosions with very little bound material (Müller et al. 2017). If the star explodes as an electron-capture SN, it is expected to produce very little nickel (Nomoto 1987; Miyaji & Nomoto 1987; Mayle & Wilson 1988; Wanajo et al. 2009; Müller et al. 2017; Poelarends et al. 2017). Additionally, core-collapse explosions from iron cores on the lower-mass end should also produce much less nickel than their more massive counterparts (Radice et al. 2017). Sukhbold et al. (2016) show iron yields, which can be taken as a proxy for nickel yields, for single stars models; stars with cores comparable to those of helium giants from binaries produce less nickel by a factor of about 10.

An important consideration for the light curves is that the final radii and envelope configurations of these models may evolve beyond what are presented here. If they become even more extended, they could result in even brighter supernovae. Based on preliminary calculations, we speculate that the radii of many of these stars

could reach hundreds of $R_\odot$. However, the radii may be constrained by companion interaction; if the orbit has not widened enough, the expanding helium star will overflow its Roche lobe and be stripped via case BB mass transfer (see e.g. Delgado & Thomas 1981; Dewi et al. 2002; Tauris et al. 2017). Explosions from stars that have undergone such extreme stripping have been explored by Tauris et al. (2013) and Tauris et al. (2015).

We have used a simple mass loss prescription that mimics Case B mass transfer, then allow the star to evolve as though it is a single star, such as in. Realistically, a scenario is needed in which the entire hydrogen envelope can be lost to Roche lobe overflow; but at the end of the star's life, the He envelope is allowed to grow without becoming unstable. There are several ways to accomplish this. One is that the secondary star is more massive than the He star after case B mass transfer. Any subsequent mass loss from the He star due to Roche lobe overflow will cause the orbit to widen, and for some binary configurations the He star may have quite an extended radius at core-collapse. It will require a more detailed exploration of binary parameters to show what final donor star structures are possible (see e.g. Yoon et al. 2010). Even if the star overfills the new Roche lobe, the Roche lobe only needs to be $100 - 200$ $R_\odot$ for the star to produce bright shock-cooling transients. It is also possible that material overflowing the Roche lobe produces a common envelope ejection, which the exploding star might run into as a dynamically ejected shell or wind rather than as an extended hydrostatic envelope.

Alternatively, as described by Dessart et al. (2018), the accretor may be originally a lower-mass star that then becomes higher mass once it removes the donor's hydrogen envelope. This star then might evolve faster than its companion and explode as a supernova first, potentially unbinding the binary system and allowing the donor to continue evolving as a single helium star. In this scenario, the helium envelope could then expand unimpeded and possibly reach several hundred $R_\odot$. Another way to produce a single helium star would be a common envelope interaction during case B mass transfer, in which a low-mass companion star merges with the core of the donor. The small amount of remaining hydrogen could then be lost via winds during the core helium-burning phase, producing a bare helium core that could expand unimpeded.

A broader consideration is that many regular SNe Ibc, which are assumed to be mostly radioactively powered, could have a strong shock cooling component (Arnett 1982; Bersten et al. 2014). As seen in Kleiser et al. (2018), adding some nickel to

the ejecta can result in double-peaked light curves, but if a small amount is mixed into the ejecta, the peaks may be blended. In fact, the presence of an extended envelope should cause a reverse shock that will cause Rayleigh-Taylor instabilities and mix nickel outward (Paxton et al. 2018). Therefore the luminosity from any nickel produced in the explosions of these helium red giants would likely blend with the shock cooling component rather than causing a double-peaked light curve. The Rayleigh-Taylor mixing would also change the overall abundance structure, which we do not address here. If blending between a significant shock cooling component and nickel component occurs, then it would be difficult to tease out the contribution of each power source based on the peak luminosity.

References

Arnett, W. D., 1982, ApJ, 253, 785

Bersten, M. C., Benvenuto, O. G., Folatelli, G., et al., 2014, AJ, 148, 68, 68

Chevalier, R. A., 1989, ApJ, 346, 847

—, 2012, ApJL, 752, L2, L2

Delgado, A. J., & Thomas, H.-C., 1981, A&A, 96, 142

Dessart, L., Yoon, S.-C., Livne, E., & Waldman, R., 2018, A&A, 612, A61, A61

Dewi, J. D. M., Pols, O. R., Savonije, G. J., & van den Heuvel, E. P. J., 2002, MNRAS, 331, 1027

Divine, N., 1965, ApJ, 142, 824

Drout, M. R., Chornock, R., Soderberg, A. M., et al., 2014, ApJ, 794, 23, 23

Dudley, R. E., & Jeffery, C. S., 1990, MNRAS, 247, 400

Eldridge, J. J., Fraser, M., Maund, J. R., & Smartt, S. J., 2015, MNRAS, 446, 2689

Glebbeek, E., Gaburov, E., de Mink, S. E., Pols, O. R., & Portegies Zwart, S. F., 2009, A&A, 497, 255

Habets, G. M. H. J., 1986a, A&A, 167, 61

—, 1986b, A&A, 165, 95

Kasen, D., Thomas, R. C., & Nugent, P., 2006, ApJ, 651, 366

Kasen, D., & Woosley, S. E., 2009, ApJ, 703, 2205

Kasliwal, M. M., Kulkarni, S. R., Gal-Yam, A., et al., 2010, ApJL, 723, L98

Kleiser, I. K. W., & Kasen, D., 2014, MNRAS, 438, 318

Kleiser, I. K. W., Kasen, D., & Duffell, P. C., 2018, MNRAS, 475, 3152

Koubský, P., Harmanec, P., Yang, S., et al., 2006, A&A, 459, 849

MacFadyen, A. I., Woosley, S. E., & Heger, A., 2001, ApJ, 550, 410

Mayle, R., & Wilson, J. R., 1988, ApJ, 334, 909

Miyaji, S., & Nomoto, K., 1987, ApJ, 318, 307

Moriya, T. J., Terreran, G., & Blinnikov, S. I., 2018, MNRAS, 475, L11

Müller, B., Wanajo, S., Janka, H.-T., et al., 2017, Mem. Soc. Astron. Italiana, 88, 288

Nomoto, K., 1984, ApJ, 277, 791

—, 1987, ApJ, 322, 206

O'Connor, E., & Ott, C. D., 2011, ApJ, 730, 70, 70

Paczyński, B., 1971, Acta Astronomica, 21, 1

Paxton, B., Schwab, J., Bauer, E. B., et al., 2018, ApJS, 234, 34, 34

Podsiadlowski, P., Joss, P. C., & Hsu, J. J. L., 1992, ApJ, 391, 246

Poelarends, A. J. T., Wurtz, S., Tarka, J., Cole Adams, L., & Hills, S. T., 2017, ApJ, 850, 197, 197

Popov, D. V., 1993, ApJ, 414, 712

Quataert, E., & Shiode, J., 2012, MNRAS, 423, L92

Radice, D., Burrows, A., Vartanyan, D., Skinner, M. A., & Dolence, J. C., 2017, ApJ, 850, 43, 43

Savonije, G. J., & Takens, R. J., 1976, A&A, 47, 231

Shivvers, I., Zheng, W. K., Mauerhan, J., et al., 2016, MNRAS, 461, 3057

Sukhbold, T., Ertl, T., Woosley, S. E., Brown, J. M., & Janka, H.-T., 2016, ApJ, 821, 38, 38

Tauris, T. M., Langer, N., Moriya, T. J., et al., 2013, ApJL, 778, L23, L23

Tauris, T. M., Langer, N., & Podsiadlowski, P., 2015, MNRAS, 451, 2123

Tauris, T. M., Kramer, M., Freire, P. C. C., et al., 2017, ApJ, 846, 170, 170

Wanajo, S., Nomoto, K., Janka, H.-T., Kitaura, F. S., & Müller, B., 2009, ApJ, 695, 208

Woosley, S. E., Langer, N., & Weaver, T. A., 1995, ApJ, 448, 315

Yoon, S.-C., 2015, PASA, 32, e015, e015

Yoon, S.-C., Woosley, S. E., & Langer, N., 2010, ApJ, 725, 940

Yoon, S.-C., Gräfener, G., Vink, J. S., Kozyreva, A., & Izzard, R. G., 2012, A&A, 544, L11, L11

Yoon, S.-C., Dessart, L., & Clocchiatti, A., 2017, ApJ, 840, 10, 10

Chapter 7

DISCUSSION

7.1 More on Binary Systems and Rapidly Rotating Stars

The importance of binary evolution is hard to overemphasize when it comes to understanding the progenitors of core-collapse SNe. While it is often tempting to focus on single-star models due to their relative simplicity compared with the many parameters of binary systems, they are extremely lacking in characterizing a large fraction of progenitor stars. There is a large body of work studying potential binary evolution channels (e.g. Podsiadlowski et al. 1992; Zapartas et al. 2017; Yoon et al. 2010; Yoon 2015; Yoon et al. 2017; Poelarends et al. 2017; Eldridge et al. 2013) and ascribing binary systems to individual SNe when single star models will not suffice (e.g. Bersten et al. 2014; Podsiadlowski & Joss 1989; Nomoto et al. 1994; De et al. 2018), but comprehensive binary population synthesis models will be needed to thoroughly explore the parameter space available for SN progenitors, including both RFSNe and more typical CCSNe alike. There are several compelling reasons to believe that binary considerations are critical for a significant fraction, if not majority, of CCSNe.

One reason is that the number of SNe Ibc and the number of very massive stars simply do not add up. If all stars can be treated as single stars, their mass loss rates are assumed to be primarily due to radiation pressure, and mass loss rates will be proportional to the luminosity. On the Main Sequence, this radiation pressure goes as a strong function of mass ($L \propto M^3$ or more). In the single star scenario, only the most massive stars—those above ~ 34 $M_\odot$—should produce SNe Ibc (Heger et al. 2003). Assuming a typical initial mass function (IMF) of Salpeter (1955)

$$\xi(m)dm = \xi_0 \left(\frac{m}{M_\odot}\right)^{-2.35} \frac{dm}{M_\odot} , \tag{7.1}$$

the fraction of stars at this very high mass end is not large enough to account for the fraction of SNe Ibc among all CCSNe, which would require total H-stripping above an initial mass of only ~ 22 $M_\odot$ (Smith et al. 2011). This disparity becomes even more difficult to reconcile when considering the possibility that more massive stars should tend to be more compact in their cores and more likely than lower-mass stars to collapse directly into black holes rather than exploding. In addition, the wind

mass loss rates due to radiation pressure may be lower than previously expected, which further casts doubt on the ability of radiation pressure alone to result in high numbers of very stripped stars (Bouret et al. 2005).

Another line of evidence comes from direct observations of massive star populations themselves. Sana et al. (2012) conducted the VLT-FLAMES survey studying clusters of massive stars in the Tarantula Nebula. They were able to determine that in these clusters, roughly 70% of stars were close enough to a binary companion to interact significantly throughout their lives. There are several possible outcomes of this interaction based on the stars' masses and orbital separation. The most common possibility (33%) is that the star with greater initial mass will expand after the Main Sequence and undergo Roche lobe overflow, donating mass to its companion. This stripping may be great enough to remove most or all of the hydrogen envelope of the donor star. Another possibility is that the binary is close enough that, after the more massive star expands, there is a common envelope phase. Some of these systems (24% of systems) will merge, while others will exit the common envelope phase as a binary but only after having exchanged mass and angular momentum.

While we have exclusively focused on SNe from stars that undergo mass loss, it is also interesting to consider what becomes of the mass accretors in binary systems. Smith & Tombleson (2014) showed through an observationally based argument that many of these may end up as luminous blue variables (LBVs), which are known for violent episodes of mass loss prior to explosion. Here LBVs were shown to exist on average significantly farther from the centers of massive star clusters than other types of stars within that cluster. A possible explanation for this deviation is that, if the LBV begins as the less massive star in a binary system and accretes mass from its companion, the companion could explode first and impart the star with a kick, sending it to the outskirts of the cluster. It has previously been widely assumed that LBVs represented a transitional phase of mass loss preceding the mass-stripped Wolf-Rayed phase; this explanation would again assume a single star system and would account for the existence of H-stripped massive stars using pulsational mass loss. Their positions relative to the massive star clusters, however, suggest that this scenario is unlikely and that LBVs may in fact be the ejected mass accretors from binary systems. While this conclusion is intriguing and the argument compelling, it remains to be shown why mass accretors would ultimately become LBVs.

Another phenomenon that should affect the pre-SN structure of a star is rotation. This could occur through mass accretion or simply through single star evolution from

a protostellar cloud that happens to have a large angular momentum. Rotation can introduce additional mixing that is not typically incorporated into stellar models; for example, rotationally induced mixing similar to meteorological turbulence on Earth could cause a star to entirely dredge up nuclear burning products from its core to the surface on the Main Sequence, immediately producing a fully H-free star without any significant mass loss (Maeder 1987), which is expected to evolve blueward on the HR diagram. Rotationally mixed stars have been invoked as potential GRB progenitors (Kulkarni et al. 1998; Woosley et al. 1999; Fryer & Heger 2005; Yoon & Langer 2005; Yoon et al. 2006) since they could become H-free without spinning down and losing angular momentum during Roche lobe overflow in a binary system. They have also been proposed as the progenitors of single or binary black hole systems should the core collapse (Mandel & de Mink 2016). Brott et al. (2011) present a grid of models of such stars and show this blueward evolution. Therefore it may be possible through rotation alone to produce progenitors for H-free SNe without strong radiation-driven winds or binary evolution. What these stars will look like prior to core collapse is uncertain, but these rotating stars should be investigated further as potential progenitors for a variety of H-free explosions. One might expect, however, that stars with large amounts of angular momentum would not be attractive candidates for SNe that undergo nickel fallback, which may be required to produce RFSNe. Nevertheless, they should result in some kind of exotic transient.

7.2 Supernova Remnants and Fallback

Some of the most fundamental questions about CCSNe concern the explosion mechanism and dynamics, namely how and whether a given star will explode; these questions are closely linked to the type and properties of the remnants left behind. There are several possibilities for a star undergoing core collapse. One is that the collapse will form a neutron star (NS), which will bounce back at formation and initiate an explosion, unbinding virtually all material outside the newly formed NS. Another possibility is that some fallback of material will occur, which could result in a larger NS or even the delayed formation of a black hole (BH). Finally, under some conditions, the star may collapse directly into a BH, in which case there would be no explosion at all.

The outcome for a particular star may depend on its compactness (O'Connor & Ott 2011; Sukhbold et al. 2017), a parameter that measures the inverse of the radius containing a certain amount of interior mass. Higher-compactness pre-SN stars are expected to collapse into black holes, while lower-compactness stars should form

neutron stars. This function is not monotonic with mass and can be quite jagged, so relating pre-SN stars directly to their core-collapse outcomes may be difficult. The outcomes also likely depend on other factors besides mass, including rotation and explosion energy (given that, as we have shown, lower explosion energies lead to fallback). Additionally, Clausen et al. (2015) found that the ability or failure of a star to explode may be somewhat chaotic, casting some doubt on the possibility of definitively linking certain types of stars with the remnants they might produce.

Even so, it is worth attempting to find ways to relate massive stars to their probable remnants, and there are more ways to approach this problem aside from running computationally intensive simulations of explosion dynamics. While we have not addressed the complex problem of the explosion itself in this work, our findings—and other observationally-driven findings in the same vein—can be coupled with observations of remnant populations to elucidate possible links between types of stars and the compact objects they leave behind. For example, a more extensive grid of CCSNe similar to the one presented in Chapter 3 could shed light on this question by an examination of which stars produce unrealistic-looking SNe. In these cases, it may be that the star collapses promptly into a black hole, so no optical transient is seen. Furthermore, we might expect the remnants of RFSNe, if these are produced by fallback of nickel, to be higher-mass neutron stars or black holes formed from the collapse of the neutron star after fallback occurred.

One outstanding question that could be answered by a more thorough study using models of optical transients such as in this work is the gap between known NS masses and BH masses. Both theoretically and observationally, the maximum mass of a NS should not greatly exceed $\sim 2.0 - 2.5\ M_\odot$ (Kiziltan et al. 2013; Alsing et al. 2017). However, observed BH masses start at $\sim 5\ M_\odot$ at the low-mass end (Corral-Santana et al. 2016). This gap may be due to the small number of observed stellar mass black holes, but it could also have a physical origin. It could be tied to fallback, and it may be consistent with the fact that our calculations in Chapter 5 show a steep rise in fallback at low energies; in order to remove only $\sim 0.1\ M_\odot$ from the ejecta, we have to carefully tune the explosion energy, whereas it is much more likely that either all material outside the core will be unbound or the entire star will collapse into a black hole. Further exploration in both BH population studies and the dynamics of fallback will be needed to solidify the connection between the two.

7.3 Galactic Evolution

The possibility that RFSNe are energetic, massive explosions from the core-collapse mechanism has implications for our understanding of the galaxies they inhabit. The chemical evolution of galaxies is driven almost entirely by supernovae, both core-collapse (Types II and Ibc) and thermonuclear (Type Ia). Because each of these two major classes of SNe stems from a different evolutionary path, and because each involves a distinct explosion mechanism, their respective impacts on the interstellar medium (ISM) chemical evolution are very different and occur at disparate times. Through observations of the rate and type of chemical enrichment, this evolution can be linked back to the rates and types of SNe that occur throughout the galaxy's lifetime.

In the simplest terms, most CCSNe occur within $\sim$ tens or hundreds of Myr after star formation and tend to enrich the ISM with α elements such as C, O, Ne, Mg, Si; meanwhile, SNe Ia are produced by white dwarfs and may occur up to several Gyr later. Because SNe Ia involve thermonuclear reprocessing of much of the ejecta, a large fraction of the material blown off is rich in iron-group elements, and they release much less α element material. Comparing abundance ratios measured in galaxies such as [O/Fe] versus [Fe/H] (a proxy for time as the galaxy becomes enriched in heavy elements) can help determine which types of SNe have enriched the galaxy and can therefore aid in determining its formation history (Gilmore & Wyse 1991). Chemical evolution models combine star formation rates and initial mass functions with this understanding of different nucleosynthetic yields from SNe produced by stars of different masses (see Kirby et al. 2011, and references therein).

Additionally, SNe in general represent not only an injection of chemically enriched material into the ISM; they also deposit angular momentum into the galaxy and even drive galactic winds and outflows (see e.g. Hopkins et al. 2017). Therefore, knowing the rates and types of SNe is essential for understanding the evolutionary history, dynamics, and composition of a galaxy.

If, due to their short timescales, RFSNe represent a previously unaccounted-for population of SNe that have ejected significant mass and momentum into their galaxies, they could explain potential discrepancies between observations of galactic properties and observed rates of CCSNe. Previous attempts have been made to link the expected yields from supernovae with the chemical evolution of galaxies. Timmes et al. (1995) recover solar abundances well by modeling chemical evolution of galaxies using a Saltpeter initial mass function and nucleosynthetic yields from

stellar evolution and supernova simulations (Woosley et al. 1995). Based on the calculations in these two papers, it can be shown that single non-rotating stars above $\sim 20\ M_\odot$ should be the ones to produce more than $\sim 1\ M_\odot$ of oxygen and that these should dominate the oxygen production in supernovae because, even though they are rare, the amount of oxygen produced per star is large.

However, Jerkstrand (2017) show that modeling of nebular spectra for SNe IIP and IIb typically yields less than about one solar mass per explosion. Additionally, modeling of light curves of SNe Ibc (e.g. Ensman & Woosley 1988) shows that most of these explosions also should have small ejecta masses ($\lesssim 1\ M_\odot$), so none of the typical SNe appear to represent explosions of very high-mass ($\gtrsim 20\ M_\odot$) stars that should produce the bulk of the oxygen found in the universe.

Brown & Woosley (2013) introduced an upper ZAMS mass cutoff above which stars might be expected to collapse into black holes rather than explode as SNe. If these more massive stars fail to explode, it could explain the lack of SNe with evidence of large oxygen masses in their nebular spectra, as would be expected from single stars in the 30-40 $M_\odot$ range. However, additional oxygen needs to come from somewhere in order to produce the predicted solar abundances from Timmes et al. (1995). Short-lived nickel-free explosions of massive stars such as the RFSNe discussed in this work could be covertly enriching their galaxies with O and other α elements. Many of the models shown in this thesis have large ejecta masses, including two or more solar masses of oxygen. Depending on their actual rates, then, they could be a viable way to make up for the lack of SNe from massive single stars that would be needed to produce the universe's α elements.

A further intriguing possibility arises from the fact that the extent of stripped star envelopes may be independent of the tendency for nickel to fall back. Therefore fallback of nickel could occur even if the pre-SN star is not extended by pre-SN activity or swelling. With radii of only a few $R_\odot$, these SNe would have almost undetectable shock cooling as is true for regular SNe Ibc; if no nickel is produced, these events would be undetectable in the optical except in very nearby galaxies. In this case, significant mass could still be ejected with significant energy, but these SNe would be unaccounted for in models of chemical and mechanical evolution of galaxies.

7.4 Exotic Power Sources

While it is natural and useful to assume the most typical SN power sources when attempting to explain RFSNe, i.e. nickel decay and shock cooling, it is possible that there are other, more exotic power sources involved. We review some of these potential contributors to the light curve here.

One intriguing consideration is that RFSNe could represent pulsational pair ejections, which could result in the ejection of one or more shells of mass without unbinding the star (Barkat et al. 1967). These ejections would occur prior to oxygen burning and if central temperatures are high enough (several $\times 10^9$ K) in massive enough stars ($\sim 20 - 30$ $M_\odot$ or more). Under these conditions, electron-positron pairs can form and rob the core of pressure support. The core contracts, then the contraction is reversed by oxygen burning; however, O burning starts slowly and the core overshoots in its contraction. The burning then rapidly reverses the contraction and can eject large amounts of material. The ejecta would consist of oxygen and its burning products as well as any lighter elements in the envelope, so the presence of iron-group elements in spectra would rule out this model for any RFSNe. Nickel is not produced in this scenario, so it is possible that pulsational pair instabilities could represent a way to eject a shell such that a later core-collapse explosion would interact with CSM; or the ejection itself could produce a bright nickel-free transient on its own. This mechanism has been proposed many times to explain certain very luminous SNe whose light curves are not consistent with radioactive decay (Woosley et al. 2007). This case is distinct from our proposed model in that it does not involve the actual terminal explosion of the star. Pair instability may be a natural way to produce bright light curves without invoking fallback as a way of removing the nickel.

Another important consideration is that of radiation from infalling material. If we imagine that nickel is not present in the ejecta of RFSNe due to fallback, it is worth considering whether the fallback itself onto the remnant could radiate enough to contribute significantly to the light curve. As discussed in MacFadyen et al. (2001), fallback may cause the delayed formation of a black hole and accretion disk, which could deposit additional energy into the ejecta with a luminosity $L_{\rm acc} = \epsilon \dot{M} c^2$, where ϵ may be roughly a few percent to a tenth of a percent. Even with a small ϵ, an amount of energy $\sim$1 B could easily be deposited and could change the resulting light curve. Dexter & Kasen (2013), show that an accretion disk should follow $\dot{M} \propto t^{-5/3}$, so depending on how significant the amount of fallback is and how large

the efficiency, we might expect the light curves of some RFSNe to have a component that follows this timescale. Dexter & Kasen (2013) attempt to model SN 2010X as entirely powered by fallback accretion, which requires a shutoff of accretion onto the remnant after 7 days in order to fit the rapid decline.

The final exotic power source we discuss is the injection of energy from a rotating neutron star via strong magnetic fields. After a CCSN goes off and produces a neutron star, the ejected material, which is ionized, could be further accelerated by a rotating magnetic field. This is because charged particles are constrained to orbit magnetic field lines unless their momentum is large enough to overcome the strength of the magnetic field. The result is that rapidly rotating magnetic fields can have an "egg-beater" effect on the ejecta, imparting angular momentum to the material until it has too much kinetic energy to be constrained to the field lines. If the field around a rapidly rotating neutron star is very large ($\sim 10^{15}$ G), the phenomenon is known as a magnetar, and it is expected to provide a large amount of additional energy and power and extremely bright transient (Kasen & Bildsten 2010). However, it is also possible that rotating neutron stars with more typical magnetic fields could power short-lived, dimmer events (Hotokezaka et al. 2017). These may be too rapid to explain even the RFSNe discussed in this work, but there could be regions of this parameter space involving neutron stars with various rotational velocities and magnetic field strengths that lend themselves to a variety of peculiar transient objects.

7.5 Observational Considerations

Future observations will be needed to help characterize RFSNe and determine their impact on other aspects of the universe. It is therefore useful to discuss the future prospects of discovering RFSNe and what observations are required to determine their nature.

The intrinsic rate of RFSNe is unknown and is difficult to approximate given the small sample size, short timescales, and the variability in peak luminosity, with some objects being quite faint. Drout et al. (2014) estimate a rate from Pan-STARRS1 of $\sim 4 - 7\%$ the rate of all CCSNe based on their sample, which includes some H-rich and H-free RFSNe of variable luminosity and light curve shape. We assume 7% as an optimistic intrinsic fraction of all CCSNe.

Given this fraction, the upcoming Zwicky Transient Facility (ZTF), which is expected to discover $\sim$ 90 SNe Ibc per year, will likely yield several RFSNe per year

as well. The Large Synoptic Survey Telescope (LSST) will discover hundreds of thousands of CCSNe per year, so it can be expected that thousands of RFSNe will be found each year among them. The difficulty in following up such a large influx of new SNe from LSST is sheer volume as well as determining which objects are interesting based on limited information. It is therefore necessary to determine simple criteria for follow-up. As discussed previously, RFSNe should be characterized by very blue colors early on due to the high shock cooling temperature, whereas nickel-powered H-free SNe should be much redder. Therefore objects flagged for follow-up in the search for explosions through extended He envelopes should look for H-poor SNe with very blue early colors.

There are several other key observational pieces that would aid in distinguishing our explanation of RFSNe from other models. The first would the presence or absence of early-time shock cooling or even shock breakout. It can be difficult to distinguish between shock cooling and nickel power at the peak of the light curve, since both will be observed as optical thermal emission of similar temperatures. However, what shock cooling from an explosion through an extended envelope would not have in common with nickel power is very hot blue early thermal emission as well as UV emission. UV evidence of shock breakout, which is the first optical/UV emission that reaches the surface as the SN shock breaks out of the envelope, would be a smoking gun in favor of our model. Nakar & Sari (2010) calculate these light curves in detail for red supergiant, blue supergiant, and Wolf-Rayet (WR) cases. The timescale for this emission, which depends on the light travel time across the star, would last minutes for a WR star of several solar radii, but it would last hours up to perhaps a day for the extended progenitors we expect for RFSNe, as their radii should be similar to those of red supergiants. Detection of shock breakout emission should therefore be easier for RFSNe than for WR progenitors of ordinary SNe Ibc and also could provide a direct estimate of the pre-SN radius.

Searching for shock breakout emission is one of the goals for ULTRASAT (Sagiv et al. 2014), a proposed small UV satellite with a wide field of view that would point at one area of the sky for an extended period of time. The approximate discovery rate of RFSNe from ULTRASAT can be found in the following way. The estimated volume rate of CCSNe is 0.075×10^{-4} Mpc yr^{-1} (Li et al. 2011). ULTRASAT has a field of view of 210 deg^2 and is expected to be able to detect SNe out to about

200 Mpc. Then the rate of discovery should be

$$R_{\mathrm{RFSNe}} = f_{\mathrm{RFSNe}}(0.075 \times 10^{-4}\ \mathrm{Mpc\ yr^{-1}})\left(\frac{210\ \mathrm{deg}^2}{41253\ \mathrm{deg}^2}\right)\left(\frac{4\pi}{3}(200\ \mathrm{Mpc})^3\right) \approx 0.84\ \mathrm{yr}^{-1}\left(\frac{f_{\mathrm{RFSNe}}}{7\%}\right), \tag{7.2}$$

where f_{RFSNe} is the intrinsic fraction of all CCSNe made up by RFSNe. Therefore it can be expected that ULTRASAT will catch the early UV radiation from roughly one RFSN per year, assuming our core-collapse model is correct and assuming that $f_{\mathrm{RFSNe}} \sim 7\%$, on the higher end of the Drout et al. (2014) estimate.

A second observational feature is narrow lines, which would indicate that the shock is continuing to run through some CSM as the SN is observed. Narrow lines were observed for SN 2015U by Shivvers et al. (2016), indicating that at least some RFSNe do involve interaction with an extended He envelope. No such narrow lines have been discovered for other RFSNe, but their absence does not necessarily determine that these are fundamentally different types of SNe—in fact, the time at which narrow lines disappear (or limits on this quantity) can help characterize the differences between RFSNe with different CSM structures.

We provided the following simple argument for Shivvers et al. (2016). Under the assumption that their light curves are all shock cooling curves without significant contribution from radioactive nickel, the peak luminosities and timescales should be governed roughly by

$$t_{\mathrm{SN}} \propto E^{-1/6} M^{1/2} R^{1/6} \kappa^{1/6} T^{-2/3}\ ,$$

$$L_{\mathrm{SN}} \propto E^{5/6} M^{-1/2} R^{2/3} \kappa^{-1/3} T^{4/3}\ ,$$

from Chapter 4 (Kleiser & Kasen 2014), adapted from Kasen & Woosley (2009) for hydrogen-free SNe, where E is the energy of the SN explosion, M is the mass ejected, and R is the effective radius. In particular, consider the peak luminosity equation. Some insight can be derived if we assume these explosions are similar in nature and in all their properties except for the effective pre-supernova radius R, which would be either the envelope radius or the radius of an outflow determined by the time before explosion and the speed at which the pre-SN material was ejected. Other parameters may vary and there could be some degeneracy among them, but assume they are constant (similar velocities and colors indicate at least that the objects' temperatures and E/M ratios should be similar).

Therefore the pre-SN $R \propto L_{\rm SN}^{3/2}$. If we assume that the ejecta velocities of all three objects are similar, this means that the ejecta from the supernova itself will pass through the surrounding CSM in a time $t_{\rm interact} \propto R$, meaning that the time after explosion in which we expect to see narrow lines from this interaction is proportional to R. Comparing the relative peak luminosities, we find that, since SN 2015U showed narrow lines up to $\sim$ 16.5 days after explosion, SN 2002bj should have shown narrow lines at least until $\sim$ 5.5 days after explosion, and the even dimmer SN 2010X would have shown narrow lines at least until $\sim$ 0.52 days. These times are well before the first spectra were taken for either SN 2002bj or 2010X. Typically, we expect that to discover narrow lines in these rapidly-fading SNe, we will either need to look at the brighter among them or catch them early. Luminosity (and timescale) may also depend on the explosion energies, ejected masses, and other properties of the SN, but these must be disentangled with more sophisticated numerical approaches.

Once the SN leaves the photospheric phase and becomes transparent, an additional observational indicator to obtain is nebular spectra (or lack thereof). Given our expectation that RFSNe are not nickel-powered, or only have a very small amount of nickel, we predict that nebular lines typically excited by the presence of nickel (see Jerkstrand 2017, for an overview) should not be present. If they were discovered, this would favor a different model from the one presented in this work.

Given how many RFSNe have already been discovered and the power of upcoming surveys to find and characterize large numbers of SNe, more examples will be quickly added to this diverse class. If such surveys and follow-up programs are geared toward the right observational criteria, it should be straightforward to distinguish between nickel-free shock cooling light curves and other phenomena which may masquerade as the same type of object. Future observational programs will produce exciting and important lines of evidence for this new type of stellar explosion.

References

Alsing, J., Silva, H. O., & Berti, E., 2017, ArXiv e-prints

Barkat, Z., Rakavy, G., & Sack, N., 1967, Physical Review Letters, 18, 379

Bersten, M. C., Benvenuto, O. G., Folatelli, G., et al., 2014, AJ, 148, 68, 68

Bouret, J.-C., Lanz, T., & Hillier, D. J., 2005, A&A, 438, 301

Brott, I., de Mink, S. E., Cantiello, M., et al., 2011, A&A, 530, A115, A115

Brown, J. M., & Woosley, S. E., 2013, ApJ, 769, 99, 99

Clausen, D., Piro, A. L., & Ott, C. D., 2015, ApJ, 799, 190, 190

Corral-Santana, J. M., Casares, J., Muñoz-Darias, T., et al., 2016, A&A, 587, A61, A61

De, K., Kasliwal, M. M., Cantwell, T., et al., 2018, ArXiv e-prints

Dexter, J., & Kasen, D., 2013, ApJ, 772, 30, 30

Drout, M. R., Chornock, R., Soderberg, A. M., et al., 2014, ApJ, 794, 23, 23

Eldridge, J. J., Fraser, M., Smartt, S. J., Maund, J. R., & Crockett, R. M., 2013, MNRAS, 436, 774

Ensman, L. M., & Woosley, S. E., 1988, ApJ, 333, 754

Fryer, C. L., & Heger, A., 2005, ApJ, 623, 302

Gilmore, G., & Wyse, R. F. G., 1991, ApJL, 367, L55

Heger, A., Fryer, C. L., Woosley, S. E., Langer, N., & Hartmann, D. H., 2003, ApJ, 591, 288

Hopkins, P. F., Wetzel, A., Keres, D., et al., 2017, ArXiv e-prints

Hotokezaka, K., Kashiyama, K., & Murase, K., 2017, ApJ, 850, 18, 18

Jerkstrand, A., 2017, ArXiv e-prints

Kasen, D., & Woosley, S. E., 2009, ApJ, 703, 2205

Kasen, D., & Bildsten, L., 2010, ApJ, 717, 245

Kirby, E. N., Cohen, J. G., Smith, G. H., et al., 2011, ApJ, 727, 79, 79

Kiziltan, B., Kottas, A., De Yoreo, M., & Thorsett, S. E., 2013, ApJ, 778, 66, 66

Kleiser, I. K. W., & Kasen, D., 2014, MNRAS, 438, 318

Kulkarni, S. R., Frail, D. A., Wieringa, M. H., et al., 1998, Nature, 395, 663

Li, W., Chornock, R., Leaman, J., et al., 2011, MNRAS, 412, 1473

MacFadyen, A. I., Woosley, S. E., & Heger, A., 2001, ApJ, 550, 410

Maeder, A., 1987, A&A, 178, 159

Mandel, I., & de Mink, S. E., 2016, MNRAS, 458, 2634

Nakar, E., & Sari, R., 2010, ApJ, 725, 904

Nomoto, K., Shigeyama, T., Suzuki, T., & Saio, H., 1994, in Evolution of the Universe and its Observational Quest, ed. K. Sato, 507

O'Connor, E., & Ott, C. D., 2011, ApJ, 730, 70, 70

Podsiadlowski, P., & Joss, P. C., 1989, Nature, 338, 401

Podsiadlowski, P., Joss, P. C., & Hsu, J. J. L., 1992, ApJ, 391, 246

Poelarends, A. J. T., Wurtz, S., Tarka, J., Cole Adams, L., & Hills, S. T., 2017, ApJ, 850, 197, 197

Sagiv, I., Gal-Yam, A., Ofek, E. O., et al., 2014, AJ, 147, 79, 79

Salpeter, E. E., 1955, ApJ, 121, 161

Sana, H., de Mink, S. E., de Koter, A., et al., 2012, Science, 337, 444

Shivvers, I., Zheng, W. K., Mauerhan, J., et al., 2016, MNRAS, 461, 3057

Smith, N., Li, W., Filippenko, A. V., & Chornock, R., 2011, MNRAS, 412, 1522

Smith, N., & Tombleson, R., 2014, ArXiv e-prints

Sukhbold, T., Woosley, S., & Heger, A., 2017, ArXiv e-prints

Timmes, F. X., Woosley, S. E., & Weaver, T. A., 1995, ApJS, 98, 617

Woosley, S. E., Langer, N., & Weaver, T. A., 1995, ApJ, 448, 315

Woosley, S. E., Eastman, R. G., & Schmidt, B. P., 1999, ApJ, 516, 788

Woosley, S. E., Blinnikov, S., & Heger, A., 2007, Nature, 450, 390

Yoon, S.-C., 2015, PASA, 32, e015, e015

Yoon, S.-C., & Langer, N., 2005, A&A, 443, 643

Yoon, S.-C., Langer, N., & Norman, C., 2006, A&A, 460, 199

Yoon, S.-C., Woosley, S. E., & Langer, N., 2010, ApJ, 725, 940

Yoon, S.-C., Dessart, L., & Clocchiatti, A., 2017, ApJ, 840, 10, 10

Zapartas, E., de Mink, S. E., Van Dyk, S. D., et al., 2017, ApJ, 842, 125, 125

Chapter 8

CONCLUSIONS & FUTURE DIRECTIONS

In this thesis, we have demonstrated an effective pipeline for 1D core-collapse SN simulations and some of its potential uses. In particular, we have focused on explosions from stars stripped of part or all of their H envelopes (SNe Ib and Ic), since they are less well understood than their hydrogen-rich SN II counterparts. We presume that this stripping is due to binary interaction, since this allows us to explore many different models without constraints regarding the amount of stripping that occurs.

While there is some exploratory work studying "normal" SNe Ibc, the bulk of this thesis centers around progressive refinement of models for RFSNe, which are much less well understood. We have shown in Chapters 4, 5, and 6 that our models of large-radius stars or stars inside circumstellar shells can reliably produce RFSN light curves if we assume that no radioactive nickel is produced. However, there are still several branches of further study that are necessary for understanding these unusual events and truly determining the nature of their origins.

One important expansion on this work would be greater detail in the treatment of binary evolution. Here we have used simple mass loss prescriptions to remove certain amounts of mass from the exterior of each star, but more physical models are necessary to determine the possible parameter space of this mass stripping. Notably, once stars undergo extensive mass stripping (due to Roche Lobe overflow), their radii shrink dramatically. Under certain circumstances, much or all the hydrogen envelope may be entirely removed, and in others it may not.

Additionally, particularly in the case of stars from Chapter 6, we may desire a scenario in which the entire hydrogen envelope is removed, but the helium envelope is later allowed to expand significantly without being lost to Roche Lobe overflow. Achieving this scenario will likely require a change in orbital distance between the star and its companion, which can occur; the possible extent to which the orbit can change due to the initial mass transfer must still be determined.

Another possibility is that, instead of a large radius, the star has an unbound hydrogen-poor shell that has been previously ejected from the star, as presumed in Chapter 5, likely in the final days or months before explosion. Further study

on the dynamics that can arise during late-stage burning is necessary to determine whether this is likely, how much mass could be unbound, and how early prior to explosion it would be ejected.

In this work, another primary assumption we have not fully addressed is how radioactive nickel could fail to be present in the ejecta. While there is some discussion of nickel fallback in Chapter 5, a better understanding of the explosion mechanism and dynamics is required to determine the feasibility of this explanation. It is also possible that nickel could fail to form if shock temperatures are low, but this would require low explosion energies against a small interior density gradient. Both of these nickel-eliminating scenarios require low explosion energies, which may be hard to reconcile with the large peak brightnesses of some of these objects.

Finally, a greater effort must be made to systematically fit observed RFSNe to physical parameters and characteristics. This will require at least three things: 1. radiation hydrodynamics for the cases in which the shock may not have passed through all of the envelope/CSM by the time of observation; 2. detailed spectra of models; 3. a comprehensive grid of models in the parameter space in order to determine any degeneracies in the model and how they can be broken. An exciting time lies ahead in that a wealth of new transients will be discovered while computational viability continues to increase. Characterizing the zoo of RFSNe and other usual transients will soon become more feasible than ever, thereby greatly bolstering our ability to shed light on their obscured physical nature.